THE UNIVERSITY OF QUEENSLAND

AUSTRALIA

Encoding and Measuring Information in High-Dimensional Quantum States

Mahdi Qaryan

MSc. Malek-Ashtar University of Technology

Candidate's ORCID

A thesis submitted for the degree of Masters of Philosophy at

The University of Queensland in 2021

School of Mathematics and Physics

Abstract

The advent of quantum information has revolutionized the world of communications and the demand for high-speed, high-capacity, and high-security communication systems is increasing. As the result, researchers are always looking for new methods to meet these needs. High-dimensional quantum systems are of increasingly greater interest as they offer increased information capacity, as well as high levels of resilience against noise, through access to the larger Hilbert spaces. Despite the benefits of communication with d-dimensional quantum states with $d > 2$—known as qudits—the generation, transmission, and detection of them is more challenging. In fact, the exact same exponential scaling that gives a quantum information processing in higher dimensions, its power also makes the process of encoding, measuring and transmitting of such data, more challenging.

In the first part of this thesis, we address a new method known as *self-guided tomography* (SGT) to characterize the unknown quantum states in higher dimensions. We prove that unlike the standard method of quantum state estimation, the autonomy, precision, and robustness of SGT against high levels of noise makes it a great candidate to work with high-dimensional quantum systems. In the second part of this thesis we work on simulating and optimizing a new nano-fabrication design for the edge coupler of lithium niobate photonic integrated circuits. This is as a segment of a larger project to build an efficient quantum router for real-world quantum networks.

Declaration by author

This thesis is composed of my original work, and contains no material previously published or written by another person except where due reference has been made in the text. I have clearly stated the contribution by others to jointly-authored works that I have included in my thesis.

I have clearly stated the contribution of others to my thesis as a whole, including statistical assistance, survey design, data analysis, significant technical procedures, professional editorial advice, financial support and any other original research work used or reported in my thesis. The content of my thesis is the result of work I have carried out since the commencement of my higher degree by research candidature and does not include a substantial part of work that has been submitted to qualify for the award of any other degree or diploma in any university or other tertiary institution. I have clearly stated which parts of my thesis, if any, have been submitted to qualify for another award.

I acknowledge that an electronic copy of my thesis must be lodged with the University Library and, subject to the policy and procedures of The University of Queensland, the thesis be made available for research and study in accordance with the Copyright Act 1968 unless a period of embargo has been approved by the Dean of the Graduate School.

I acknowledge that copyright of all material contained in my thesis resides with the copyright holder(s) of that material. Where appropriate I have obtained copyright permission from the copyright holder to reproduce material in this thesis and have sought permission from co-authors for any jointly authored works included in the thesis.

Publications included in this thesis

[1] **Mahdi Qaryan**, Markus Rambach, Michael Kewming, Christopher Ferrie, Andrew G. White, and Jacquiline Romero, Robust and Efficient High-dimensional Quantum State Tomography, *Physical Review Letters*, 126, 100402 (2021).

Submitted manuscripts included in this thesis

No manuscripts submitted for publication

Other publications during candidature

No other publications

Contributions by others to the thesis

No contributions by others

Statement of parts of the thesis submitted to qualify for the award of another degree

No works submitted towards another degree have been included in this thesis

Research involving human or animal subjects

No animal or human subjects were involved in this research

Acknowledgments

More than anything, I would like to take this opportunity to express my special thanks to my principal supervisor, Andrew White for his great support all through these years. Working with Andrew is a rich path of exceptional guidance and professional advice. To Andrew: you were way more than just a supervisor for me and I learnt a lot from your scientific and social character. I also want to thank Markus Rambach, Jacqui Romero, Till Weinhold and Marcelo Pereira De Almeida for their superb supervision during this research.

I am indebted to Mehdi Davoudi as it was all his help and support through my undergraduate and postgraduate that made me hopeful and interested in walking through the academic research.

I'd like to appreciate all the great students in our team, in particular Leonardo Assis, Michael Kewming, Kaumudi Goswami who were always supportive and super-friendly all over the ups and downs of my research and life as well as Lewis Howard, Ming Su, Raphael Abrahao and Jihun Cha that working alongside them brought me a fantastic and unique experience.

Also I need to thank Angela Bird and Murray Kane specifically since if it was not their brilliant work from very first day of me joining this research group I would not have such a smooth and calm path to the end.

Behind the scenes of every achievement in my life, there has been the unended love and support of my compassionate family and in particular my mother that her memory is always with me every step that I take. I am never able to appreciate enough the peace of mind and encouragement my mother and brother gifted to my life. To Ali, my lovely brother: you have always been incredible source of inspiration and guidance for me.

Last but not least, I want to thank my friends, Mehran, Fatemeh, Shayan, Maziar, Ahmad and Mohsen. Thank you for all the moments you have been standing with me, so I could continue on my path despite all the difficulties.

سپاسگزاری

بیش از هر چیز، مایلم از این فرصت استفاده کرده و از استاد راهنمایم، آندرو وایت، به دلیل حمایت های بی دریغش در طی این سالها تشکر ویژه کنم. همکاری با آندرو مسیری سرشار از راهنمایی و مشاوره تخصصی است. به آندرو: شما برای من فراتر از یک استاد بوده و هستید. من از شخصیت علمی و اجتماعی شما بسیار آموختم و امیدوارم همچنان بتوانم از وجود شما بهره‌مند شوم. همچنین از مارکوس رامباخ، جکی رومرو، تیل وینولد و مارسلو پریرا د آلمیدا برای مشاوره‌های فوق العاده‌شان در طول این تحقیق تشکر می‌کنم.

لازم میبینم در اینجا از استاد مهدی داوودی عزیز هم قدردانی کنم چرا که کمک ها و حمایت‌های پر از لطف ایشان در دوره‌های کارشناسی و کارشناسی ارشد بود که سبب امیدواری و علاقمندی من به انجام تحقیقات دانشگاهی شد.

از همه دانشجویان این گروه، به ویژه لئوناردو آسیس، مایکل کیومینگ، کامودی گسوامی که در همه فراز و نشیب های این دوره، دوستانه همراه و حامی‌ام بودند و همچنین از لوئیس هاوارد، مینگ سو، رافائل ابرهائو و جیهون چاو که کار در کنار آنها یک تجربه فوق العاده و منحصر به فرد را برای من به ارمغان آورد سپاسگزاری می‌کنم.

همچنین لازم است به طور خاص از آخلا برد و موری کین تشکر کنم، زیرا اگر کار و تلاش بی‌وقفه و درخشان آنها از همان نخستین روزهای پیوستن من به این گروه تحقیقاتی نبود، تجربه‌ی چنین مسیر هموار و آرامی در طول این دوره برایم فراهم نمی‌شد.

در پس هر دستاوردی در زندگی، عشق و حمایت بی پایان خانواده‌ی دلسوز و به ویژه مادرم بوده و هست. یاد او همراه همیشگی لحظه لحظه‌های زندگیم خواهد ماند. هرگز نمی‌توانم به اندازه کافی از آرامش روحی و دلگرمی ای که مادر و برادرم به زندگی من هدیه کرده‌اند قدردانی کنم. به علی، برادر دوست داشتنی‌ام: تو همیشه منبعی الهام بخش و راهنمایی خردمند برای من بوده‌ای.

همچنین در پایان می خواهم از دوستان مهربانم مهران، فاطمه، شایان، مازیار، احمد و محسن تشکر فراوان کنم: برای تمامی لحظاتی که در کنار من ایستاده‌اید تا بتوانم با وجود همه مشکلات به راه خود ادامه دهم سپاسگزارم.

Financial support

This research was supported by an Australian Government Research Training Program Scholarship. It has also been supported by Top-Up Scholarship of the ARC Center of Excellence ”EQUS”.

Keywords

quantum information, qubit, high-dimension, quantum state tomography, transverse spatial mode, density matrix

Australian and New Zealand Standard Research Classifications (ANZSRC)

ANZSRC code: 510803, Quantum Information, Computation and Communication, 50%
ANZSRC code: 510804, Quantum Optics and Quantum Optomechanics, 25%
ANZSRC code: 510204, Photonics, Optoelectronics and Optical Communications, 25%

Fields of Research (FoR) Classification

FoR code: 5108, Quantum Physics, 75%
FoR code: 5102, Atomic, Molecular and Optical Physics, 25%

To Mom, Dad
and my brother Ali

Contents

List of Figures

List of Tables

Part I

Quantum State Tomography

Chapter 1

Introduction

In our daily life, the operation of many systems is at the classical level, meaning that in our interactions there is no significant quantum effect observed. Such classical systems are configured by a set of variables which can be determined with certainty in an ideal measurement. As the result—except in cases where we consider the effect of noise—the concept of probability in classical mechanics is not as fundamental as in quantum mechanics. In measuring a quantum phenomenon, even when having maximum knowledge about it, does not lead to a deterministic result. Probability is so basic in this case that one can consider the whole definition of quantum mechanics as an algorithm to calculate the probabilities of different outcomes in the process of the measurement. This provides the best probabilistic estimate of the quantum system which assigns a quantum mechanical description to it. Because of the resemblance with the medical computerized tomographic (CT) imaging this process of quantum state estimation is normally referred as *quantum state tomography* (QST).

Despite the limitations of this basic approach to characterizing more complex quantum systems—i.e. systems with more than two levels, be they either multiple qubits or single higher dimensional systems, qudits—for decades it has been the standard method of quantum state tomography, which here I call *Standard tomography* (ST). Although the subject of quantum state estimation is rather new compared with quantum mechanics, its importance specially in the fields of quantum information and quantum optics has attracted much interest from researchers.

In this research we examine the performance of a new QST technique called *self-guided tomography* (SGT) when used with qudits [1]. This new method has been already tested on qubits, there realizing the promise of: high accuracy and precision with less measurements, high robustness, and no post-processing [2]. All of these have been key issues with standard tomography when utilized for more complex systems such as qudits.

Applying quantum protocols on d-level quantum systems, with $d > 2$ (qudits), enables significant advantages which originate from access to higher dimensions of Hilbert space. The larger the dimension of the state space used to encode the quantum information, the higher the channel capacity and the more secure the quantum communication [3, 4]. Other benefits of utilizing qudits for quantum information are their resilience against higher levels of noise [3, 5, 6] and optimal cloning [7]. In this work we use

the the transverse shapes of light as qudits.

In this thesis we first cover the basic knowledge required to work with the spatial modes of light. In Chapter 2, after a short note about discrete quantum communication elements—qubits and qudits—in Section 2.2, we get familiar with mathematics of the transverse spatial modes. In Sections 2.3 and 2.4, we briefly address the generation of Laguerre-Gaussian modes as the Gaussian mode family that we use in our experiment. Finally we discuss about limiting factors of using spatial modes in communication systems, Section 2.6.

In Chapter 3 after introducing *Bloch sphere* as the general graphical tool to picture a qubit system, and *density matrix* as a comprehensive mathematical tool to describe the state of the real quantum systems— Sections 3.1 and 3.2, we provide an example of two-level spatial modes. In Sections 3.4 and 3.5, we get familiar with the basic concepts as well as the historical evolutionary trends in the field of quantum state tomography. We address the theory of self-guided tomography in Section 3.6 and then finish this chapter with bringing the results achieved using SGT on two-level quantum systems—Section 3.7.

Chapter 4 covers the details of our experiment on applying self-guided tomography on 3, 5, and 20 dimensional quantum systems, Sections 4.1 to 4.3. In continue of this chapter, we present the results under both noiseless and noisy regimes and compare them to the results obtained using standard tomography in the case of qutrits ($d = 3$) and ququints ($d = 5$).

In chapter 5, we address a different topic about nanofabrication of lithium niobate integrated circuits which can be considered as a platform to realize the high dimensional quantum states. Here we cover the results of our trials in simulating the edge coupler design as the critical part of the circuit structure, responsible for the magnitude of the fiber to chip loss.

Chapter 2

Communication with Spatial Modes of Light

2.1 Introduction

Different optical communication systems utilize a variety of optical properties such as polarization, wavelength, intensity, or phase in order to encode and carry information. The spatial mode of light is another degree of freedom, rather new—less used for communication systems compared with the aforementioned ones—with special characteristics which have inspired researchers toward inventing revolutionary methods in quantum communication and quantum computing.

The spatial mode of light is the profile of the electric field in three spatial dimensions. *Transverse spatial modes* are solutions of the wave equation in the paraxial limit, where there is no longitudinal component to the light's transverse electric (E) and magnetic (B) fields. In detail, they are the transverse solutions of the Helmholtz electromagnetic wave equation under the paraxial approximation [8–10]. Higher order solutions of these spatial structures fall into different categories, perhaps best known are the Gauss-Hermite (where the transverse patterns have rectangular symmetry) and Gauss-Laguerre (cylindrical symmetry)—which are special cases of the Gauss-Ince [11], where the symmetry can be smoothly varied between the cylindrical and rectangular limits—and Gauss-Bessel, which is also cylindrically symmetric but continuous in the radial degree of freedom, as opposed to discrete like the Gauss-Laguerre [4, 12].

Since transverse modes can encode an infinite dimensional Hilbert space—a complex vector space with an inner product [13]—they are able to carry far more information than say, polarization, which is limited to a 2-dimensional Hilbert space. It is analogous to having a large set of characters in an alphabet: this allows us to encode the intended message via some physical form like specific sounds or visual characters which have a pre-agreed meaning. A larger set of symbols provides larger encoding capabilities [14–20].

Polarization is the locus of the electric field vector: if it is linear we refer to linear polarization, if it is circular, we refer to circular polarization, and between these two limits we refer to elliptical polarization. It is very uncommon to refer to polarized modes as Spin Angular Momentum (SAM) modes, as the angular momentum is not the feature of interest. Similarly, in transverse spatial modes,

the feature of interest is the locus of the phase discontinuity, not the orbital angular momentum of the field. The loci can appear as dark patterns in the optical field, straight lines, curved lines, or as points, the latter signifying a vortex. Unfortunately it is common in the literature to see transverse spatial modes referred to as orbital angular momentum (OAM) modes. This is somewhat problematic as not all transverse spatial modes have angular momentum (it would be like referring to polarization modes as spin angular momentum (SAM) modes, which we do not do). Hence in this thesis we will refer only to transverse spatial modes.

2.2 Communication with Quantum States

In classical information theory, a *bit* is any physical system which has two states that can encode the data, 0 and 1. Similar to the concept of the classical bit, which is independent of any specific physical system for its realization, quantum bits—*qubits*—can be considered as a mathematical object regardless of the type of the quantum system. However, qubits indeed are different from their classical counterpart. Actually, there is a small distinction between these two which makes huge differences in their capabilities. Both are considered having two different states—0 and 1 for classical bit and $|0\rangle$ and $|1\rangle$ for qubit—named computational basis, but qubits can take any superposition of these two states as well,

$$|\psi\rangle = \alpha\,|0\rangle + \beta\,|1\rangle\,. \tag{2.1}$$

This is the general representation of a quantum bit where α and β are complex coefficients that determine the contribution of each basis element in the linear combination of them with the probabilities

$$p(x=0) = |\alpha|^2, \text{ and } p(x=1) = |\beta|^2. \tag{2.2}$$

In a good correspondence with the regular coordinate systems in which the vector representation of every point in the space can be divided into its building components—the portion of the basis vectors along the x and y axes—the superposition state of a qubit can be represented in a vector space as well with the components α and β along the $|0\rangle$ and $|1\rangle$ bases. But this difference in the spectrum of the possible states of a quantum object is not the end of the story. In reality, what makes quantum computing an entirely different world from the classical one is that in general, outcomes are non-deterministic, meaning that probabilities are ascribed to predictions.

Let us see how and where the probability enters this topic. When measuring the state of a classical bit, knowing that its state is 0 (1), the output of our measurement will always be 0 (1) deterministically. For example, if the bit is in the state 0, measuring that bit will always yield the result “0 state”. The quantum case can be quite different. As mentioned before, in addition to $|0\rangle$ and $|1\rangle$ states, a qubit can take any superposition of them as well, $\alpha\,|0\rangle + \beta\,|1\rangle$, where $|\alpha|^2+|\beta|^2=1$. Typically measurement of the qubit is limited to some basis states, say $|0\rangle$ and $|1\rangle$, and these measurements occur with certain probabilities, $P_0=|\alpha|^2$ and $P_1=|\beta|^2$, i.e. the measurement output is not deterministic.

The measurement process to determine the contribution of each of the basis on the quantum system is known as projection. The quantum object related to that is a Hermitian operator which decomposes

the building elements of the quantum state projected on each eigenstate. The spectral decomposition relation for such a measurement is

$$\hat{M} = \sum_{n}^{N} \lambda_n \hat{P}_n = \sum_{n}^{N} \lambda_n \left|\phi_n\right\rangle \left\langle\phi_n\right|, \tag{2.3}$$

in which $\hat{P}_n$ is the definition of the projection operation and $\hat{M}$ being the projection measurement on an N dimensional state space with the eigenstates ϕ_n and the corresponding eigenvalues λ_n. The outcome of such a measurement on an unknown quantum state ψ in the direction of each eigenstate will be a probability given by

$$p_n = \left\langle \psi \left| \hat{P}_n \right| \psi \right\rangle = \left|\langle \psi \mid \phi_n \rangle\right|^2. \tag{2.4}$$

The projection operators corresponding to the computational basis of the qubit system are

$$\hat{P}_0 = |0\rangle\langle 0| \text{ and } \hat{P}_1 = |1\rangle\langle 1|. \tag{2.5}$$

In general we can choose any projective basis so long as the projectors satisfy the following identity [21].

$$\sum_{m} P_m = \mathbb{I}. \tag{2.6}$$

Qudits

Of course, for a practical information system in the real world, working with just one qubit is not terribly useful. So, the first thing which comes to mind is to expand the Hilbert space by using a system of multiple qubits. Another approach is to use any system which is not restricted to just two different basis states. In a mathematical definition there is no limit for such a basis for a quantum information system. We call it a qudit where the letter "*d*" stands for the word "dimension" representing any number of basis states greater than 2 against "*b*" for "binary" in "qubit". Although in theory it does not look like there is any advantage in utilizing qudits rather than qubits, in practice there are some points to consider. One is that you rarely find a two-level-only quantum system: what experimentalists often do is to suppress the effect of extra levels of a multilevel system to extract a two-level system out of that. It would be more advantageous to apply all the channel capacity of such a system instead of blocking it. Also, if some resource is limited for a quantum computer—e.g. space, memory, or time—a specific number of qudits in that space can do more calculations than the same number of qubits. So, the bandwidth of such a system as well as the complexity of possible calculations grows considerably. The spatial modes of light provide a reliable platform to develop quantum communications based on qudits.

2.3 The Paraxial Wave Equation

The physical realization of the field for a propagating wave can vary widely, from a transverse electromagnetic wave radiated from an optical light source through to compressed airfields in the case

of sound waves. The mathematical description of the most of these fields is similar. A function which satisfies the following partial differential equation (wave equation):

$$\nabla^2 u = \frac{1}{c^2}\frac{\partial^2 u}{\partial t^2}, \tag{2.7}$$

where c is the speed of propagating field—for electromagnetic waves this is the speed of light. ∇^2 is the Laplacian operator defined by

$$\nabla^2 u = \frac{\partial^2 u}{\partial x^2} + \frac{\partial^2 u}{\partial y^2} + \frac{\partial^2 u}{\partial z^2} \tag{2.8}$$

for the Cartesian coordinate system.

For a monochromatic electromagnetic wave, the time variations of the field can be considered sinusoidal. So, the solutions of the wave equation will be of the form $U_0(\mathbf{R})e^{-i\omega t}$ in which $U_0(\mathbf{R})$ represents the complex amplitude and ω is the angular frequency. Solving the wave equation with the solutions of this form results in a time-independent equation, the Helmholtz equation,

$$\left(\nabla^2 + k^2\right) U(\mathbf{r}) = 0, \tag{2.9}$$

where $k = n\omega/c$ is the wave vector. Assuming that the field propagates along the z direction, the complex amplitude will reduce to

$$U(\mathbf{r}) \equiv u(\mathbf{r})e^{ikz}, \tag{2.10}$$

and substituting it into the Helmholtz equation gives

$$\frac{\partial^2 u}{\partial x^2} + \frac{\partial^2 u}{\partial y^2} + \frac{\partial^2 u}{\partial z^2} + 2ik\frac{\partial u}{\partial z} = 0. \tag{2.11}$$

This assumption implies that the variations of the field in the propagation direction will be controlled mainly by the phase factor $\exp(ikz)$ and the amplitude, $u(r)$ is mostly under the effect of diffraction in the xy plane expressed as a function of $r = \sqrt{x^2 + y^2}$ so the changes in the z direction are very slow and can be neglected,

$$\left|\frac{\partial^2 u}{\partial z^2}\right| \ll \left|2k\frac{\partial u}{\partial z}\right|, \left|\frac{\partial^2 u}{\partial x^2}\right|, \left|\frac{\partial^2 u}{\partial y^2}\right|. \tag{2.12}$$

As the result, the wave equation takes the form

$$\nabla_t^2 u(\mathbf{s}, z) + 2ik\frac{\partial u(\mathbf{s}, z)}{\partial z} = 0, \tag{2.13}$$

known as the paraxial approximation, this is applicable for every case in which the angle between the wave vector k and the optical axis z is small ($\theta \lesssim 30^\circ$). In the science of optics wherever the propagation of electromagnetic waves is either of the form of paraboloid or gaussian, this model can be utilized.

2.4 Gaussian Solution Families

In general, the intensity profile of a light beam changes during the propagation through free space or a homogeneous optical medium. However, within the paraxial region where the divergence of the beam is not extreme, the shape of the beam profile does not change—modulo a rescaling factor—and can be described by the Gaussian functions. A comprehensive solution for the paraxial wave equation is the one which can cover the infinite size of the Hilbert space. There are many possible solutions, notably the Gaussian mode families which include: Laguerre-Gaussian in cylindrical coordinates; Hermite-Gaussian in rectangular coordinates; and Ince-Gaussian modes in elliptical coordinates. These solutions are the best options for describing many practical conditions. Although the lowest order of the transverse modes (TEM_{00} mode) is of great importance in a majority of research, especially the ones in which focusing and diverging properties matter, these higher order sets of solutions for the paraxial wave equation are suitable for the situations in which the nonlinear effects of the active laser medium should be minimized or multi-spot patterns are desired.

The base of all the Gaussian sets of solutions is the fundamental Gaussian mode (TEM_{00}). Lasers, if well-aligned, normally operate at this mode which has the smallest beam waist and divergence. All other higher order modes can be built from that. Let us consider that the transmitting aperture of the laser is located at the plane z=0 in which the amplitude distribution is Gaussian. The functional form of such a field can be described by

$$z=0: \quad U_0(r,0)=a_0\exp\left(-\frac{r^2}{W_0^2}-\frac{ikr^2}{2F_0}\right)=a_0\exp\left(-\frac{1}{2}\alpha_0 kr^2\right), \tag{2.14}$$

where W_0 represents the radius of the beam at $1/e$ of the maximum field amplitude, F_0 is the radius of curvature for the parabolic phase front, a_0 is the amplitude of the field at z=0, $r=\sqrt{x^2+y^2}$ radius of the beam and α_0 is a complex term,

$$\alpha_0=\frac{2}{kW_0^2}+i\frac{1}{F_0}. \quad \left[\mathrm{m}^{-1}\right]. \tag{2.15}$$

Comparing the Eq. 2.14 with the mathematical description of a general plane wave at $z=0$,

$$z=0: \quad U_0(r,0)=A_0e^{i\varphi_0}, \tag{2.16}$$

the amplitude and phase of the Gaussian beam are as follows

$$A_0=a_0\exp\left(-\frac{r^2}{W_0^2}\right), \tag{2.17}$$

$$\varphi_0=-\frac{kr^2}{2F_0}, \tag{2.18}$$

which are both dependent on beam radius r.

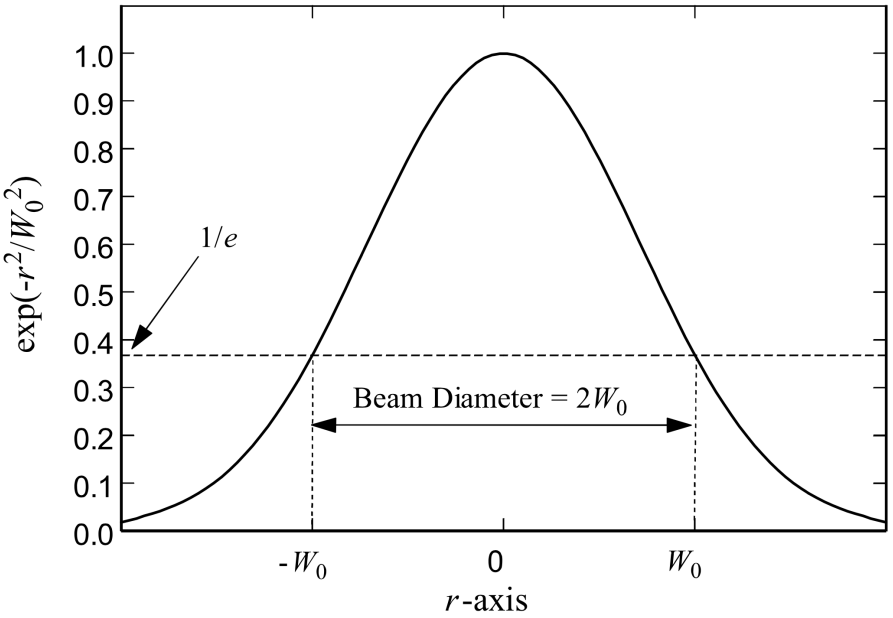

Figure 2.1: Amplitude profile of a Gaussian beam; r is the radial distance from the center of the beam, W_0 is the beam waist, defined by the point where the amplitude is $1/e$ of the maximum value. (From [22]).

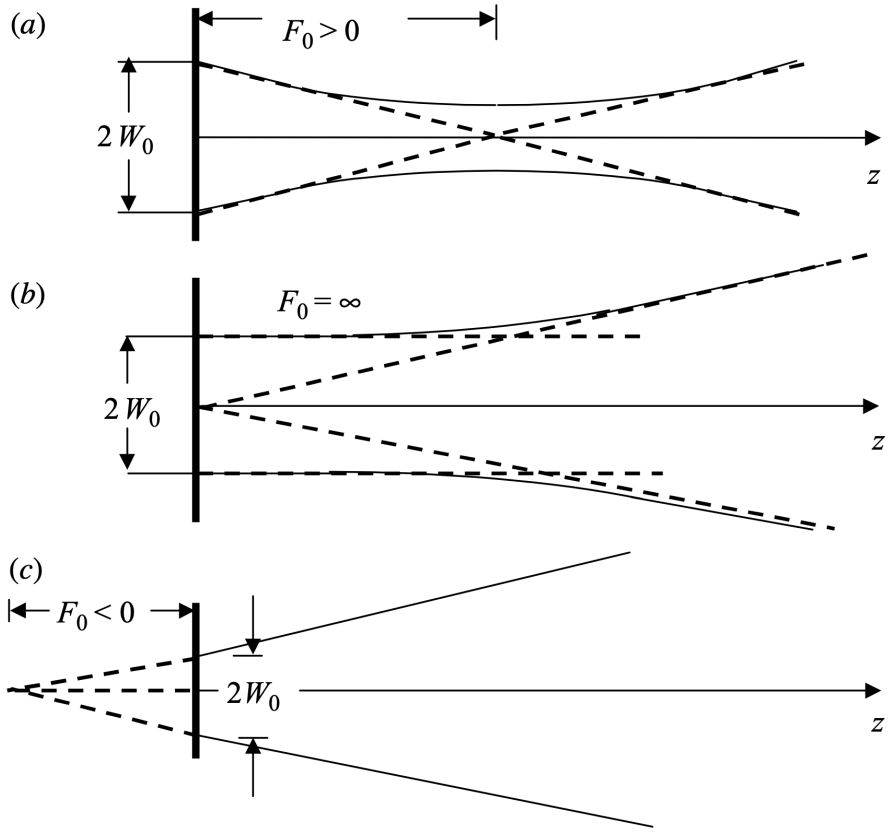

Figure 2.2: Definitions for beam focusing. F_0 is the radius of curvature for the parabolic phase front. (a) Convergent beam, F_0>0. (b) Collimated beam, F_0=∞. (c) Divergent beam, F_0<0. (From [22]).

Subject to the divergence or convergence of the parabolic shape of the beam, F_0 is negative or positive respectively, while for a collimated beam $F_0 = \infty$.

Since the quantum states in our experiment are the transverse modes of light with cylindrical symmetry, they fall into the Gauss-Laguerre family. The field associated with this set of solutions is called a Laguerre-Gaussian beam. The higher order modes in this category for the case of a collimated beam are described by

$$z=0: \quad U_{lp}(r,\theta,0)=\left(\frac{\sqrt{2}\,r}{W_0}\right)^{l}(-i)^{l}\exp(il\theta)\exp\left(-\frac{r^2}{W_0^2}\right)L_p^{(l)}\left(\frac{2r^2}{W_0^2}\right), \tag{2.19}$$

considering the exit aperture of the monochromatic light source is at z=0. r and θ are the amplitude and the azimuthal angle of the vector in cylindrical coordinate system and W_0 is the radius of the plain Gaussian mode (TEM_{00}). The term L in this equation represents the Laguerre polynomials in which l and p denote the angular and radial numbers. The general form of this equation to include nonzero z can be achieved by solving the Huygens-Fresnel integral [8, 23],

$$\begin{aligned} U_{lp}(r,\theta,z) = {} & C_{lp}\frac{W_0}{W}\left(\frac{\sqrt{2}\,r}{W(z)}\right)^{l}L_p^{(l)}\left(\frac{2r^2}{W^2(z)}\right) \\ & \times\exp[-i(2p+l+1)\varphi(z)]\exp\left(ikz+il\theta-\frac{r^2}{W^2}-i\frac{kr^2}{2F}\right); \quad l,p=0,1,2,\ldots, \end{aligned} \tag{2.20}$$

in which C_{lp} is a phase constant, F is the radius of curvature of phase front for the zero mode and W is the spot size of the beam.

The square of the absolute value of this equation results in the irradiance of the beam at each point,

$$\begin{aligned} I(r,\theta,z) &= \left|U_{lp}(r,\theta,z)\right|^2 \\ &= \frac{W_0^2}{W^2}\left(\frac{2r^2}{W^2}\right)^{l}\left[L_p^{(l)}\left(\frac{2r^2}{W^2}\right)\right]^2\exp\left(-\frac{2r^2}{W^2}\right). \end{aligned} \tag{2.21}$$

It is worth mentioning that the beam parameters such as spot size and the radius of curvature are similar for all the higher-order Gaussian modes and the same propagation relations govern their spatial transformation. However, because of having different field distribution patterns, the concentration of energy for these higher order modes is further away from the propagation axis which means the population of the photons and as the result the probability of finding photons in the region close to the paraxial axis is less comparing to the fundamental zero mode. The cross-section and top view of the concentric rings of the Laguerre-Gaussian modes are demonstrated in Figures 2.3 and 2.4.

The phase discontinuities in which the intensity of the mode jumps down from the local maximum to zero, characterize the type of symmetry as well as the mode number for the Gaussian mode families. For the case of LG modes, Figure 2.3, l and p are the number of azimuthal and radial phase jumps, respectively.

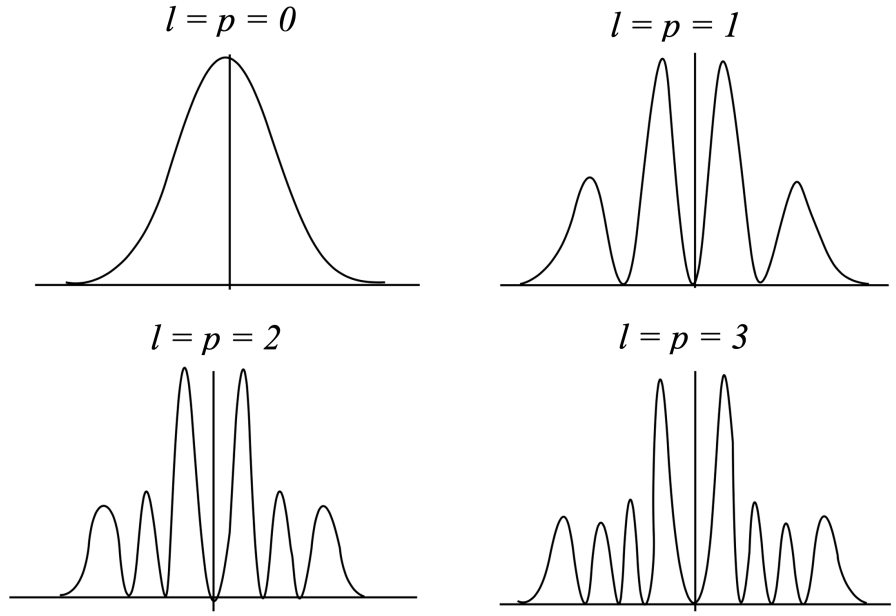

Figure 2.3: Cross-section of higher dimensional Laguerre-Gaussian modes. x-axis is radial distribution, r, y-axis is field intensity. (From [22]).

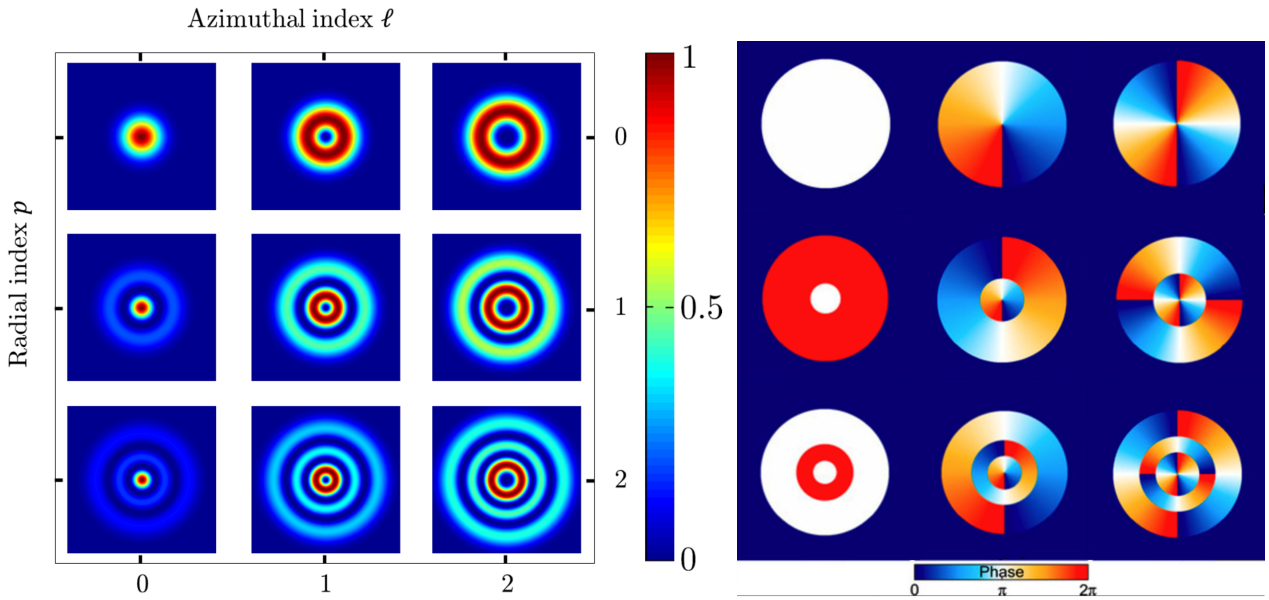

Figure 2.4: Simulated intensity (left) and phase (right) pattern of a number of Laguerre-gaussian beams. The x-axis shows the azimuthal indices, l; the y-axis shows the radial indices, p. (From [24, 25]).

2.5 Spatial Mode Generation

There are two types of Laguerre-Gaussian modes: vortex and non-vortex. What we have used in our experiment are the vortex beams (LGV). There are two kinds of vector vortex (VV) fields: uniformly polarized where the vortex is in phase, or polarization vortices. These can be made by either active or passive methods [26]. The mechanism in active methods is to induce a specific vortex mode by the manipulation of the laser cavity. Uniformly-polarized vortices can be made by using gain to lock different spatial modes to the same frequency [27], or polarization-vortices can be formed using birefringence and dichroism [28, 29]. Passive methods utilize a variety of techniques to generate inhomogeneous optical fields. Uniformly polarized vortices can be produced by computer generated

holograms [30–35]; polarization vortices can be produced by using birefringent and dichroic optical elements [36], or by applying phase retarders that rotate the polarization locally [37] and stressed fiber lasers [38]. The only reason the polarization matters to us is because the materials that spatial light modulators are made of (the little cells that make the phase) are sensitive to polarization. So the beam needs to be polarized when it hits the surface to get the best encoding.

In this experiment, in order to prepare and measure the Laguerre-Gaussian modes as our quantum states, we employ computer-generated holograms (CGH). These holographic patterns are built via a spatial light modulator (SLM) which is used to control the transverse optical field. The modulator is illuminated by our reference light beam—the lowest order Gaussian mode, l=p=0—producing vortex modes in the output. If we consider $T(x,y)$ as the complex transmission function of the hologram and $U_I(x,y)$ the complex field coming from the laser, then the output beam as the result of incident between the laser light and the hologram will be given by

$$U(x,y) = T(x,y) \times U_I(x,y). \tag{2.22}$$

In principle we can encode an arbitrary complex-valued function $T(x,y)$ using a computer-controlled spatial light modulator (SLM) where each pixel can modulate both amplitude and phase. In practice however, SLMs tend to modulate either just amplitude, or just phase, and so more indirect SLM encodings are necessary to achieve the desired result. For example, writing a spatially-varying diffraction grating into a phase SLM lets us achieve spatially varying amplitude into the diffracted mode, Figure 2.5. In such a case, $T(x,y)$ will be a spatially periodic function which can be expanded by Fourier transform

$$T(x,y) = \sum_m T_m e^{im(\mathbf{G}\cdot\mathbf{r})}, \tag{2.23}$$

in which

$$\mathbf{G} = (2\pi/\Lambda)(\cos(\theta)\hat{\mathbf{x}} + \sin(\theta)\hat{\mathbf{y}}) \tag{2.24}$$

is in the role of the wave vector for the grating with the periodicity of Λ along a θ angled direction and T_m is the amplitude of the mth order of the diffracted beam. That is

$$T_m = \frac{\iint_\Lambda T(x,y)e^{-im(\mathbf{G}\cdot\mathbf{r})}\mathrm{d}\mathbf{r}}{\iint_\Lambda \mathrm{d}\mathbf{r}} = \frac{1}{A}\iint_\Lambda T(x,y)e^{-im(\mathbf{G}\cdot\mathbf{r})}\mathrm{d}\mathbf{r}, \tag{2.25}$$

where the area of each single period of the grating is represented by A.

Regardless of its physical origin, the transformation of the grating function, $T(x,y)$, makes it possible to provide any phase onto the diffracted beam. Such a shift can be applied by the replacement $\mathbf{r} \to \mathbf{r} + \mathbf{\Delta r}$ in the Eq. 2.23 in which

$$T(x,y) = \sum_m T_m e^{im(\mathbf{G}\cdot(\mathbf{r}+\mathbf{\Delta r}))} = \sum_m T_m e^{im(2\pi\delta)} e^{im(\mathbf{G}\cdot\mathbf{r})} = \sum_m T'_m e^{im(\mathbf{G}\cdot\mathbf{r})}, \tag{2.26}$$

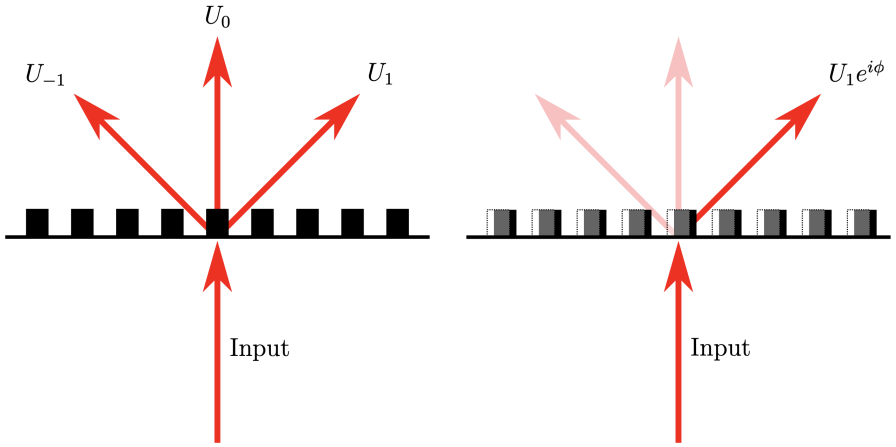

Figure 2.5: Left: The input beam incident on the periodic pattern splits into multiple diffraction orders. Right: The phase of diffracted orders established by shifting the grating. (Dotted line indicates original grating position; gray and black indicates new grating position). (From [39]).

$$2\pi\delta = \mathbf{G} \cdot \mathbf{\Delta r} \tag{2.27}$$

and δ denotes the relative shift in terms of the periodicity of the grating. In practice, this type of phase modulation is equivalent to changing the optical path as the consequence of shifting the grating which results in the accretion of an additional phase [40].

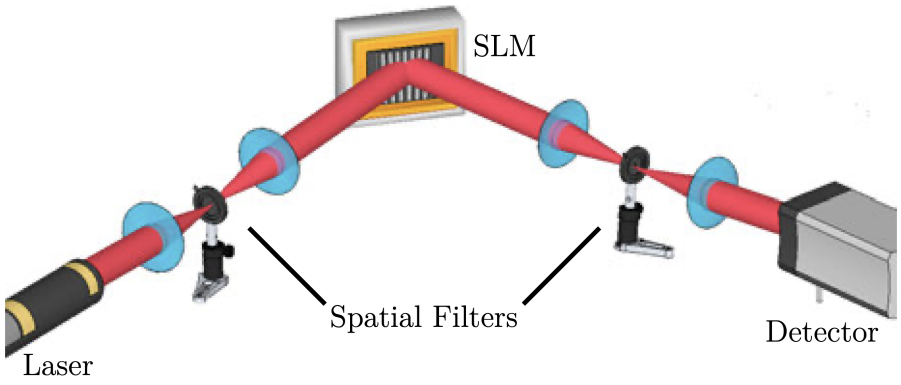

Figure 2.6: A simple experimental setup to generate the transverse spatial modes of light using computer generated holograms displayed on a SLM. The laser beam is filtered spatially both before and after the SLM. The filter before the SLM ensures the beam is in the lowest order, the filter after the SLM selects out higher-order spatial modes, passing only the desired target mode, e.g. $LG_{+1,0}$, but filtering out $LG_{+1,p>0}$. (From [39]).

Full control over the phase and amplitude of the modes is possible through defining an additional modulation on the periodic pattern. Figure 2.6 shows a simple version of such a system. In order to attain a standard collimation all through the setup, the laser light with the basic Gaussian mode travels through a spatial filter before reaching the SLM. After the laser beam incidence with the encoded grating pattern on the SLM, another spatial filter selects out the desired modulated light among multiple diffraction orders and finally a detector registers the intensity of the generated field. It is worth mentioning that the spatial frequency of the modulated grating should not exceed **G**, as it will result in the overlap of different diffraction orders.

2.5.1 Phase Modulator SLMs

As we use a phase only spatial light modulator in our experiment, here we talk about it in more detail. The transmission function for such an SLM is

$$T(x,y) = e^{i\Psi(x,y)} \tag{2.28}$$

where $\Psi(x,y)$ is the phase at the point (x,y). If our desired beam in the output is of the form

$$U(x,y) = A(x,y)e^{i\phi(x,y)}, \tag{2.29}$$

then the function Ψ should meet the requirements to modulate the amplitude, A and the phase, ϕ of it. This can be done by encoding the desired amplitude and phase via the modulation functions $f(A)$ and $\Phi(\phi)$, respectively. Therefore, the SLM phase will look like

$$\Psi = f(A)\Phi(\phi). \tag{2.30}$$

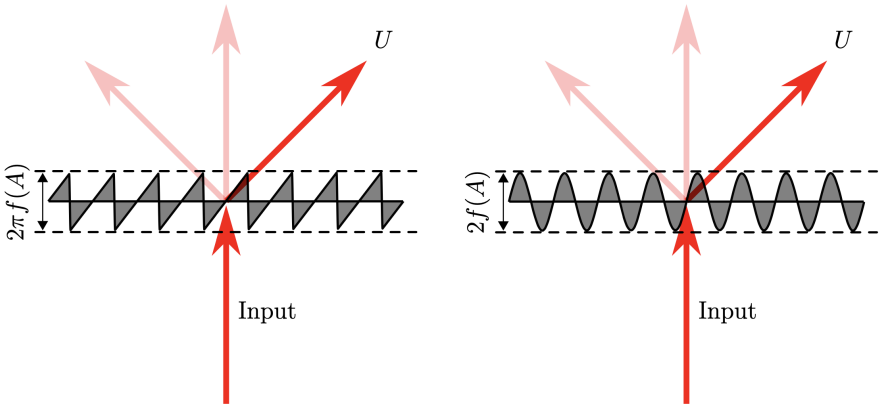

Figure 2.7: Two different types of phase grating functions. Left: encoding scheme of blazed grating; in the paraxial case, the ideal diffraction efficiency is 100%. Right: encoding scheme of sinusoidal grating; in the paraxial case, the ideal diffraction efficiency is 33.86%. (From [39]).

$\Phi(\phi)$ is a periodic function that defines the grating pattern. Two types of encoded holographic patterns on SLMs are shown in Figure 2.7. Comparing the two schemes, a sinusoidal grating may cover a broader spectral range [41] while in terms of efficiency a blazed grating works better. Ideally, in the paraxial limit the maximum efficiency of sinusoidal grating is 33.86% [42], whereas a blazed grating can have 100% efficiency.

In any application of spatial light modes we require measurements that decipher the information encoded in the spatial distribution of the beam. The basic idea—mentioned at the start of this chapter—is projective measurement. This scheme—known as the standard method—is constructed on a mathematical function named projection-valued measure (PVM), similar to real-valued measures with the difference that their values are not real numbers but self-adjoint projections.

To understand the mathematical description of a projective measurement, consider the encoded state on a system as U_0. We are interested in quantifying the overlap of the system with the mode ψ_n. It is calculated via

$$|\langle \psi_n \mid U_0 \rangle|^2 = |a_n|^2 . \tag{2.31}$$

The experimental realization of such a measurement is displayed in Figure 2.8. The applied technique is based on the Fourier filtering of the incident beam [43].

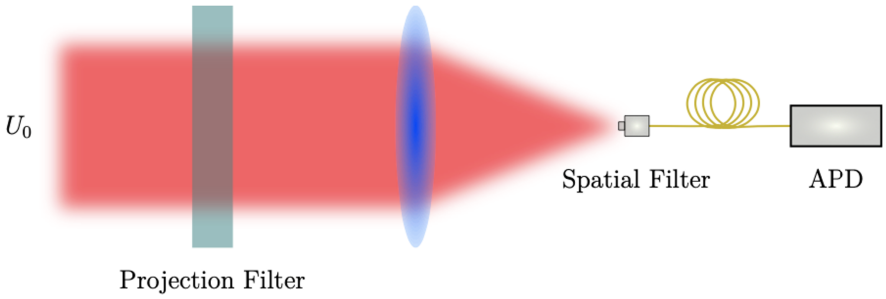

Figure 2.8: Projective measurement of transverse spatial modes. The light beam passes through a projection filter with a complex transmission function ψ_n^* that converts the target mode into the lowest-order Gaussian mode, TEM_{00}. The convex lens focuses this through a spatial filter before sending it to the detector (in this case, an avalanche photodiode, APD). (From [39]).

The transmission function $T(r)$ acts on the incident field, U_0, and the resultant $U_0 T$ is passed through a lens and focused onto an optical fiber which spatially filters the field. If the output of the Fourier plane is of the form

$$\tilde{U}(\boldsymbol{\rho}) = \frac{1}{i\lambda f}\mathcal{F}[U_0(\mathbf{r})T(\mathbf{r})] = \frac{1}{i\lambda f}\iint U_0(\mathbf{r})T(\mathbf{r})e^{-i\frac{2\pi}{\lambda f}\mathbf{r}\cdot\boldsymbol{\rho}}\mathrm{d}\mathbf{r}, \tag{2.32}$$

then the overall coupling efficiency of such a setup can be evaluated by

$$\eta = \left|\iint \tilde{U}(\boldsymbol{\rho})f(\boldsymbol{\rho})\mathrm{d}\boldsymbol{\rho}\right|^2 \approx \left|\tilde{U}(0)\iint \tilde{f}(\boldsymbol{\rho})\mathrm{d}\boldsymbol{\rho}\right|^2 \propto |\tilde{U}(0)|^2, \tag{2.33}$$

provided that filter function $f(\rho)$ does not trigger any significant change in the Fourier transform of the field $\tilde{U}(\rho)$ inside the fiber as the result of having too broad area of impact. The complex function of the projection filter is

$$T(\mathbf{r}) = \psi_n^*(\mathbf{r}). \tag{2.34}$$

which is a projective measurement, with an efficiency of

$$\eta \propto |\tilde{U}(0)|^2 \propto \left|\iint U_0(\mathbf{r})\psi_n^*(\mathbf{r})\mathrm{d}\mathbf{r}\right|^2 = |a_n|^2 . \tag{2.35}$$

2.6 Communication Limiting Factors

As previously mentioned at the start of this chapter, having access to higher dimensional systems in order to encode information provides significantly larger communication rates as well as higher levels of security in quantum key distribution techniques [5, 14, 44, 45]. Among several physical resources which have a large number of distinguishable states N, the spatial degree of freedom of light is of the most remarkable ones, in the sense that it offers an unbounded number of modes in order to construct an optical field. In practice, none of these resources can be exploited in their full capacity and therefore N will always remain finite and limited depending on the practical boundaries in each case.

In general, the various factors influencing the ability of free space as our optical channel to communicate information can be divided into two categories. The first are those that affect the population of the carriers (photons) by reducing the probability of their transmission through the communication channel. Of the factors in this group that result in photon loss in the system are transmission losses, such as diffraction, and detection losses, e.g. due to non-ideal detectors. It is possible to minimize the portion of diffraction through careful optical design, but the detector characteristics are fixed features of the system that cannot be evaded. The second category includes factors that affect the coherence in the system, causing the information encoded into the carriers to become scrambled. In free-space, atmospheric turbulence is one of the main factors in this category, in fibre-optics, mechanical disturbance and optically-induced noise. Here we talk about two of these imperfections in free-space communication systems in more detail.

2.6.1 Diffraction

In free-space, one of the most basic limiting factors of N is as the result of the diffraction and loss pertained to the finite aperture size of both sender and receiver systems. Let us figure out the possible size of N under the effect of diffraction. The transmitted data as the form of a beam focused into the aperture of the receiver is distinguishable only when any two beams received at this aperture are separable considering the Rayleigh criterion

$$\delta x \propto \lambda z / D_T, \tag{2.36}$$

in which, λ is the wavelength, z is the distance between the sender and receiver apertures and D_T is the transmitter diameter. So, the area of each spot can be estimated by

$$(\delta x)^2 \propto (\lambda z)^2 / A_T, \tag{2.37}$$

with A_T representing the area of the transmitting aperture.

Subsequently, by calculating the number of spots which can be fitted inside the receiver aperture area A_R, we estimate N as

$$N \approx A_R/(\delta x)^2 \approx \frac{A_R A_T}{(\lambda z)^2} = D_F, \tag{2.38}$$

where D_F in the equation is the Fresnel number product of the sender and receiver (see Figure 2.9).

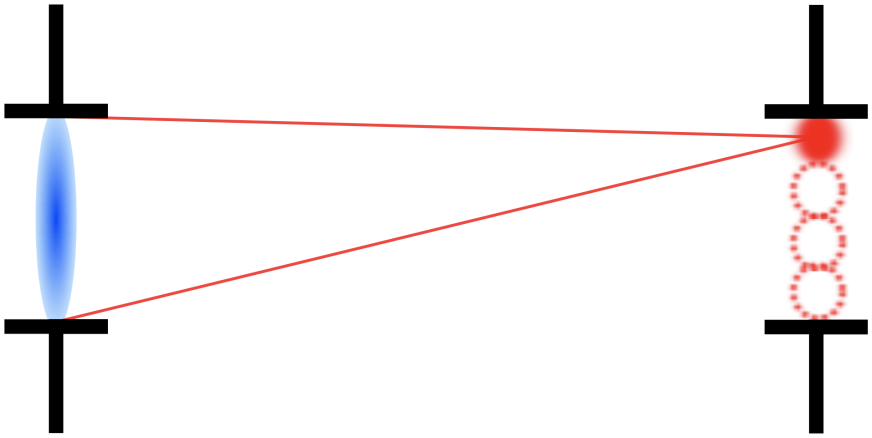

Figure 2.9: In a real communication channel using the transverse spatial modes, the sender and receiver have limited number of possible states, N to communicate—due to diffraction as well as having finite apertures. An estimate of N can be obtained by focusing a beam from the sender aperture, blue spot, to a spot in the receiver side, red spot. Every two spots in the receiver aperture are distinguishable provided that their separation satisfies the Rayleigh criterion. The Fresnel number product D_F gives the number of these separable spots. (From [39]).

2.6.2 Atmospheric Turbulence

At first glance, it might seems straightforward to study light propagating through the air by considering it similar to the vacuum, but air is a viscous fluid and observing light propagation over a sufficiently long distance exhibits its stochastic behavior caused by the fluctuations due to the atmospheric turbulence. These random fluctuations will result in inhomogeneous variations in the refractive index along the light pathway.

Turbulence is a noticeable phenomenon in any fluid characterized by a large ratio between its mean velocity $\bar{v}$, and viscosity ν, called the Reynolds number,

$$\mathcal{R} = \bar{v}\mathcal{L}/\nu, \tag{2.39}$$

where $\mathcal{L}$ is the length scale of the area of the fluid for which turbulence is considered. In shorter length scales, the fluid behaves like a cluster of turbulent eddies until at very small length scales, $\mathcal{L} = l_0$—also known as the inner scale, on the order of millimeter near the ground—the turbulence can be ignored. For the lengths smaller than inner scale close to the ground the Reynolds number is < 1, and the kinetic energy of the turbulence is released in the form of heat [46]. The length of communication

networks is typically much larger than l_0 [22]. Close to the earth's surface, the air viscosity is of the order 10^{-5} m^2/s, and considering the usual wind speeds on the order of 1 to 5 m/s results in a Reynold number,

$$\mathcal{R} \sim 10^5 \gg 1, \tag{2.40}$$

which suggests that we must always consider the atmosphere as a turbulent media for communication systems. For such systems that the length scales are much larger than l_0, the structure function governing the turbulence in the fluid follows "Kolmogorov statistics",

$$D_v = C_v^2 \delta r^{2/3}, \tag{2.41}$$

in which C_v is the velocity structure parameter that specifies the strength of the fluctuations and $\delta r \equiv \|\mathrm{r}_1 - \mathrm{r}_2\|$ is the distance measure between any two considered points of the fluid [46]. Different velocities in the fluid results in different temperatures and accordingly pressures in different regions of it. As the consequence of these fluctuations, the refractive index will also vary in different parts of the fluid which is expressed by refractive index structure function [47],

$$D_n = C_n^2 \delta r^{2/3}. \tag{2.42}$$

This leads to establishing a random phase $\phi(\mathbf{r})$ arriving at the receiver. Under the Kolmogorov conditions, the structure function that controls these phase variations is given by [48]

$$D_\phi = 6.88 \left(\frac{\delta r}{r_0} \right)^{5/3}, \tag{2.43}$$

where r_0 is known as the Fried parameter in honor of the discoverer of this equation that represents the effective coherence length of a turbulent fluid in the entrance aperture of the receiver [48, 49]. These fluctuations of an optical beam initiated by the phase randomness of the fluid will also result in amplitude variations of the beam called "scintillations". Eq. (2.44) displays the resultant optical field $U(r)$, modified by both phase and amplitude changes.

$$U(\mathbf{r}) = U_0(\mathbf{r}) \exp(i\phi(\mathbf{r}) + \chi(\mathbf{r})), \tag{2.44}$$

that U_0 is the optical field without considering the turbulence effect, ϕ is the random phase and χ is the log-amplitude variations.

In the study of astronomical systems—in order to image the celestial bodies through the turbulent atmosphere—the problem is often simplified by ignoring the amplitude fluctuations and approximating the turbulence only by a random phase screen located at the receiver's aperture. This "thin phase screen approximation" provides a simple model to study and track the optical field through atmospheric heterogeneities. This model works well for imaging astronomical objects, since the turbulence effects

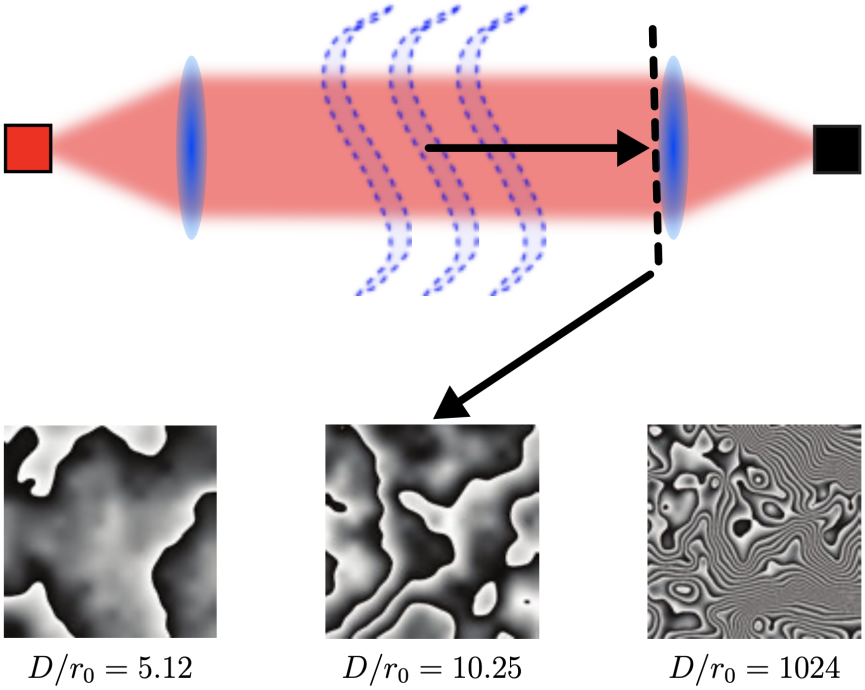

Figure 2.10: Top: A communication channel between a sender (red box) and receiver (black box). Turbulence in the channel is simulated by a phase screen before the final focusing lens. Bottom: Three instances of the simulated phase screens of different turbulence strengths D/r_0. (From [39]).

are maximum close to the telescope aperture, but it is less suitable for the cases with a long turbulent path like communication channels. However, here in this research we take advantage of its simplicity to achieve an estimate of the light propagation through real atmospheric conditions and it still works with high accuracy in the case of our experiment.

The result of applying thin phase approximation is to characterize the turbulence strength C_n by the factor D/r_0 with D as the effective diameter of the beam. Figure 2.10 displays a simple scheme of this model. As the figure shows, the sum of all the turbulent effects through the path are simulated by a single thin phase screen at the place of receiver's aperture which is controlled by the factor D/r_0. Also, three different turbulence strengths, modeled as the phase screens are shown in the figure as well.

As we can see the degree of turbulence will affect the quality of beam propagation for the amount of information we can encode. This now arises the question of how do we measure the information we encode in the beam and that leads onto quantum state tomography.

Chapter 3

Quantum State Tomography

In this Chapter we look at how to measure information encoded in a quantum state—a methodology known as quantum state tomography. It is common in the literature to see this done for qubits [50–52]. Recently there has been an explosion of interest in applying tomography to qudit systems, and meeting the challenges that arise from the rapidly increasing parameter spaces—technically the Hilbert spaces—of these systems.

3.1 Bloch Sphere

A bit is a basic binary unit of information encoded as 0 or 1. The quantum counterpart of this classical bit is a *qubit*—quantum bit—which in addition to the quantum states $|0\rangle$ and $|1\rangle$—which form one orthogonal basis of the state space—can also take a linear combination of these two states to encode the quantum information,

$$|\psi\rangle = \alpha|0\rangle + \beta|1\rangle. \tag{3.1}$$

This is called the state vector representation of the quantum states. α and β are probability amplitudes that represent the portion of each basis in the construction of the qubit and therefore under normalization the sum of their squares equals to one.

$$|\alpha|^2 + |\beta|^2 = 1 \tag{3.2}$$

The best-known instance of binary quantum states is the spin degree of freedom of a particle such as an electron. The photonic analogue of spin states is the polarization of light, so that for example the right $|R\rangle$ and left $|L\rangle$ circular polarization states perform the role of computational basis [53]. The general form of a polarization qubit can be written as

$$|\psi\rangle = \cos(\theta/2)|R\rangle + \exp(i\varphi)\sin(\theta/2)|L\rangle. \tag{3.3}$$

The angle θ specifies the weight of each basis in the superposition state while $\varphi \in [0, 2\pi]$ determines the phase difference between the eigenstates. By normalizing the Eq. (3.3) as following

$$|\langle \psi \mid \psi \rangle|^2 = \cos^2(\theta/2) + \sin^2(\theta/2) = 1, \tag{3.4}$$

we scale the wave function ψ so that all probabilities add to 1. This is the equation of a unit circle in which θ varies the probability amplitudes for $|0\rangle$ and $|1\rangle$.

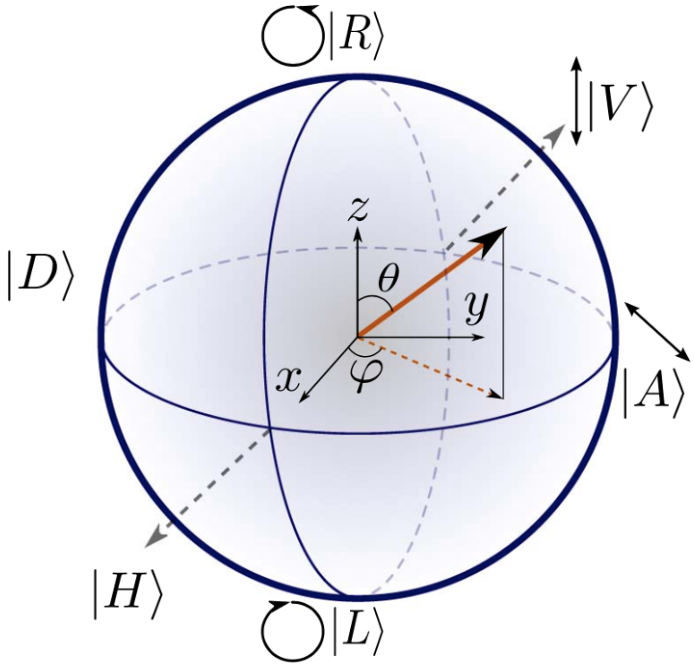

Figure 3.1: Poincaré sphere; a graphical platform to characterize any polarization state as the superposition of two orthonormal states. In this example, the parameters φ and θ represent the phase difference and the probability weight of two eigenstates, $|R\rangle$ and $|L\rangle$. (From [54]).

We can visualize Eq. (3.3) for polarization states as a vector pointing to a specific coordinate on the surface of a sphere of radius one: known as the Poincaré sphere, Figure 3.1. The polarization eigenstates $|R\rangle$ and $|L\rangle$ are characterized as the north and south poles in this sphere, respectively. In addition to this basis of orthogonal states, there are two mutually unbiased bases (MUBs) on the equator, $|H\rangle$-$|V\rangle$ and $|A\rangle$-$|D\rangle$, which are the equally weighted linear superpositions of $|R\rangle$ and $|L\rangle$ eigenstates. By definition, MUBs are sets of orthonormal bases in which the states in the basis have an overlap (inner product square) of $1/d$ with any other orthogonal state, where d is the dimension of the state space.

The spin version of the Poincaré sphere—commonly used to describe any two-level quantum state—is called the Bloch sphere: both exhibit the same Hilbert space. Through this sphere, it is also possible to characterize any transformation of the qubit states via having a reference point as well as rotations around x, y and z axes, so the final state will be distinctively measurable. As an example, consider a set of three linearly independent measurements to find an unknown state in the Bloch sphere, Figure 3.2. Regardless of the order, the measurements determine the free parameters of the

desired state one by one, isolating that quantum state to a plane, then to a line and finally to a point, respectively. This is exactly the aim behind tomographic measurements. Before we get into that we still need to arm ourselves with more tools. One of the most important ones is the density matrix.

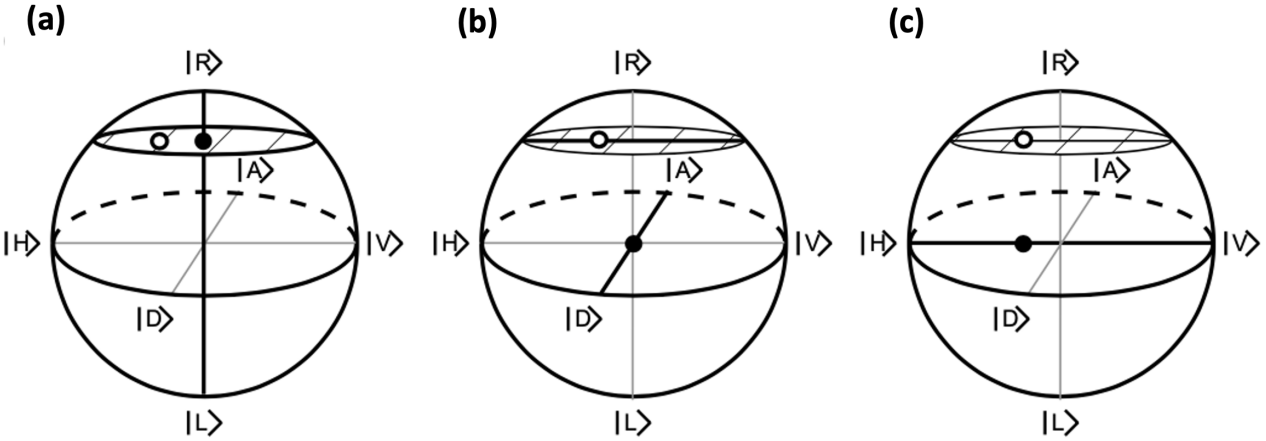

Figure 3.2: (a) Poincare sphere representation of standard quantum tomography in two-dimensional state space. A series of three measurements along the (i) right-circular, (ii) diagonal, and (iii) horizontal axes. The black dot is the projection of the true state—represented by the white dot—in the direction on the measurement. It can be interpreted so that the first projection of the unknown state identifies the plane in which the quantum state is lying. The second and third measurements however isolate this area to a line and finally a point, respectively. (From [55]).

3.2 Density Matrix

The state vector description is an idealized format that only characterizes pure quantum states: it does not support the statistical mixtures of quantum states which happen normally in nature. So, we need a comprehensive description which covers all possibilities to be able to use it for practical purposes. Imagine an ensemble of K identically prepared quantum objects (here single photons). Then a unique quantum state can characterize the whole objects in this set, $|\psi_n\rangle = |\psi\rangle$ in which $n = \{1,2,\ldots,K\}$. We call such quantum state a pure state. In contrast, if not all the elements in the ensemble be in similar quantum state, they form a weighted sum of the pure states which we call a mixed state. Since there is no correlation between the subsystems of the ensemble under such condition, the phase difference among them is totally random. The density matrix formalism is a generalization of the state vector description, Eq. (3.3) By definition, the density matrix of a pure state $|\psi\rangle$ is as follows

$$\rho := |\psi\rangle\langle\psi|. \tag{3.5}$$

So, the pure state mentioned in Eq. (3.3) in this new demonstration becomes

$$\begin{aligned}\rho =& |\psi\rangle\langle\psi| = \cos^2(\theta/2)|R\rangle\langle R| + \sin^2(\theta/2)|L\rangle\langle L| \\ &+ \cos(\theta/2)\sin(\theta/2)\exp(-i\varphi)|R\rangle\langle L| \\ &+ \cos(\theta/2)\sin(\theta/2)\exp(i\varphi)|L\rangle\langle R|.\end{aligned} \tag{3.6}$$

Consequently, a mixed state can be shown as a weighted sum of the pure states

$$\rho_{\text{mixed}} = \sum_m c_m \rho_m^{\text{pure}} = \sum_m c_m \left|\psi_m\right\rangle \left\langle\psi_m\right|, \tag{3.7}$$

in which $\sum_m \frac{N_m}{N} = \sum_m c_m = 1$. This means that any N_m of the total N subsystems in the statistical mixture are in the pure state $\left|\psi\right\rangle_m$. In addition to the Dirac (braket) notation, the density matrix can be expressed as a scalar product

$$\hat{\rho} = \frac{1}{2}(\mathbf{I} + \vec{n}\cdot\vec{\sigma}), \tag{3.8}$$

that highlights the connection between the density matrix, $\hat{\rho}$, the identity operator, I, and the rotation operators $\vec{\sigma}$. These rotation operators are known as the Pauli matrices, and express rotations around the coordinate axes, x, y and z—see Figure 3.2. The unit vector, $\vec{n}$, in Eq. (3.8) is built of the expectation values of the Pauli operators that satisfy $\|\vec{n}\| = 1$.

$$\vec{n} = (n_x, n_y, n_z) = \left(\left\langle\hat{\sigma}_x\right\rangle, \left\langle\hat{\sigma}_y\right\rangle, \left\langle\hat{\sigma}_z\right\rangle\right). \tag{3.9}$$

The matrices for the Pauli operators are

$$\sigma_1 = \begin{pmatrix} 0 & 1 \\ 1 & 0 \end{pmatrix}; \sigma_2 = \begin{pmatrix} 0 & -i \\ i & 0 \end{pmatrix}; \sigma_3 = \begin{pmatrix} 1 & 0 \\ 0 & -1 \end{pmatrix}; \mathcal{I} = \begin{pmatrix} 1 & 0 \\ 0 & 1 \end{pmatrix}. \tag{3.10}$$

3.3 Spatial Mode Qubit

In the previous section we addressed the case of two-level photonic quantum system—the polarization degree of freedom of photons—as a simple instance for pedagogical purposes. However, in this research we deal with higher dimensional quantum systems. We choose to work with the transverse spatial mode degree of freedom of light [56], as it gives us access to infinitely large dimensions. As we already talked about in detail in previous chapter, these modes are the transverse solutions of Helmholtz equation under the paraxial approximation, in which the variation ratio of transverse mode comparing to longitudinal momentum is ignorable. Although we have covered this topic in detail in chapter 2, it will be helpful to have a pictorial description of a special case of this observable known as Orbital Angular Momentum (OAM) in two dimensions in an analogue version of Bloch sphere.

The equivalent version of Eq. (3.3) for OAM can be written as [57],

$$\left|\psi\right\rangle = \cos(\theta/2)\left|\ell_1\right\rangle + \exp(i\varphi)\sin(\theta/2)\left|\ell_2\right\rangle \tag{3.11}$$

where $\left|\ell\right\rangle$ represents a paraxial field carrying $\ell\hbar$ units of orbital angular momentum. In cylindrical coordinates this is [58]

$$\left|\ell\right\rangle \equiv A(r,z)\exp(i\ell\phi). \tag{3.12}$$

$A(r,z)$ indicates the amplitude variations in the radial and longitudinal directions, the term $\exp(i\ell\phi)$ characterizes the phase variation along the azimuthal direction. Figure 3.3 shows the changes of these two parameters for a set of Laguerre Gauss OAM modes.

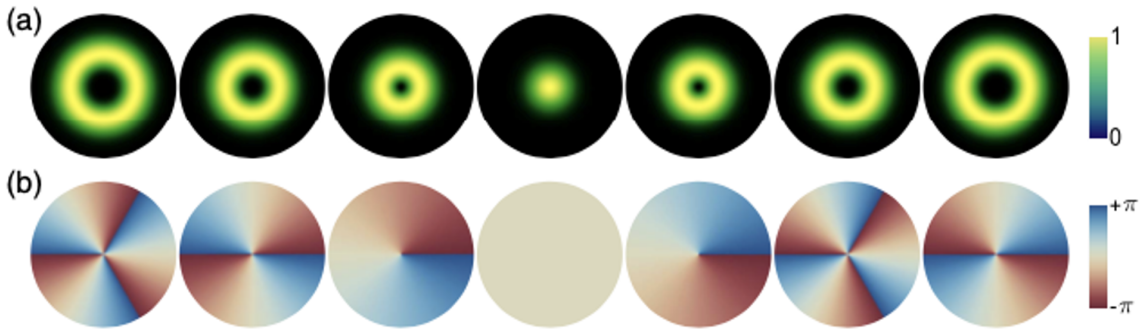

Figure 3.3: (a) Intensity profiles and (b) phase maps of a sequence of OAM modes, $p = 0$. From left to right, $l = -3, -2, \ldots, +2$, and $+3$, units of OAM. The Guoy phase shift changes with the total value $2p + |l| + 1$. (From [54]).

Similar to the polarization case, in the Poincare/Bloch sphere for OAM qubits the surface represent pure states, the poles represent the logical states, which here have maximal orbital angular momentum, and the equatorial plane are their superpositions, Figure 3.4, which have zero orbital angular momentum.

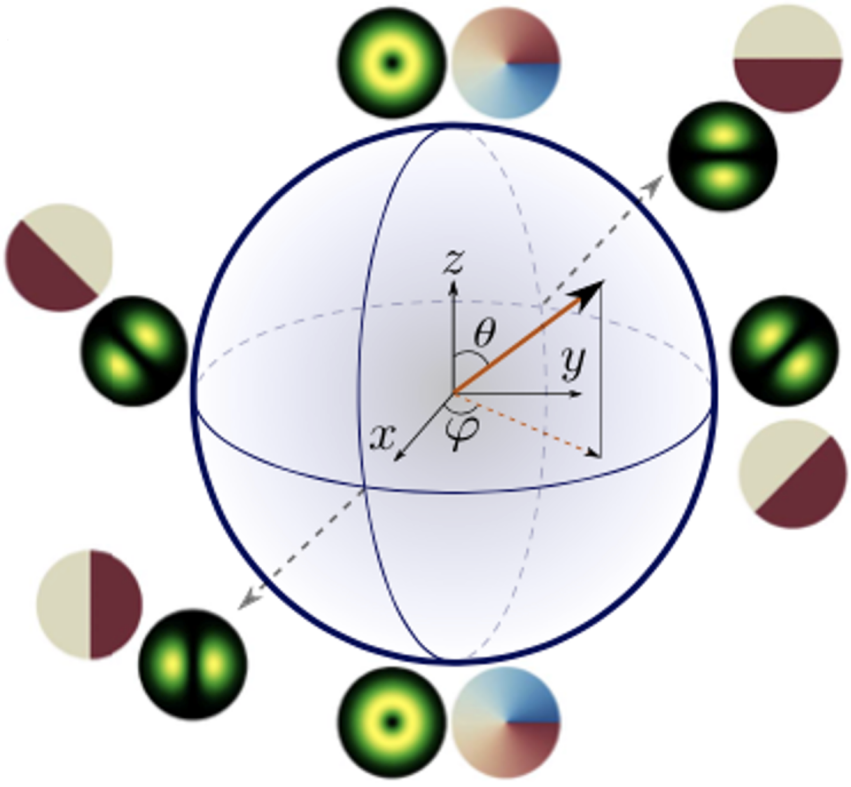

Figure 3.4: The qubit sphere: the poles correspond to the OAM eigenstates p=0, l=$\pm$1; the equator contains the MUBs, p=$\pm$1, l=0 and a version of that rotated by 45°, as shown. H+V and D+A. (From [54]).

Now having a comprehensive formalism to parameterize either pure or mixed quantum state as well as familiarity with the graphical demonstration of simple case of two-level quantum states in two different

degrees of freedom, we are ready to get into QST in more detail. The aim for doing tomographic measurements on quantum states is to rebuild their density matrices through a appropriate set of measurements [59–62].

3.4 Basic Concepts of Quantum State Tomography

To characterize the state of a physical system, we need to do a set of measurements on it to uncover its different properties. Consider a classical system such as a particle: we can determine its position, velocity, weight and all other different properties which gives us a clear vision of its state. Here only one copy of the classical system under investigation is enough to do all the measurements. But it is not the case in quantum mechanics. The interactions between the quantum system and the measurement tool changes its quantum state [63], meaning the perturbed system is no longer conducive to further measurements as the quantum state under study is no longer available [64]. To solve this problem, we need several copies of the system with the exact quantum state. But based on the no-cloning theorem, making perfect copies of an unknown quantum system is impossible and therefore our set of measurements cannot be done on the exact copy of the quantum state [65]. Furthermore, when the state of a system is unknown, it implies that there is no data about the purity and dimensionality of the system and this lack of information makes the sequence of measurements as well as choice of basis entirely nontrivial [59, 66–68]. These are some limitations of the measurement process in quantum systems. As the result, just a tiny piece of information is achievable as the outcome of each measurement on a specific aspect of the quantum system under study on an ensemble of quantum systems provided under the same condition [69]. As we discussed last chapter, projective measurements are the standard method of collecting data from a quantum state by performing multiple measurements on the system. This approach is known as quantum state tomography and was named due to the similarity with medical computed tomography, commonly known as “CT” scans. Doing an adequate number of projective measurements—known as a complete set—on a quantum state makes it possible to obtain a comprehensive image of that state through processing all-inclusive superpositions of the projections.

In resemblance with industrial drawings where the goal is to reconstruct the 3-dimensional object and map it via 2D projection images from different perspectives, quantum state tomography (QST) aims to rebuild the desired quantum state via a complete set of measurements which covers the characteristics of the quantum state projected on each basis of the state space [70]. A simple example of tomography is to regenerate a 3D object by processing its shadows on different surfaces as shown in Figure 3.5. For the case of a quantum object, these projections are the statistical measures of the desired state based on the weighted probability of the eigenstates overlapping with it [71].

In an inverse process, putting together the outcomes of these measurements can determine the density matrix of the quantum state [72–74]. The common problems among all the variations of QST is their complexity and timing since number of measurements and consequently the degree of difficulty of a tomography problem grows exponentially with the dimension of the quantum state [75, 76].

Also, these methods are very sensitive to noise [77–80] and on top of that it should be mentioned the outcomes of QSTs are achieved with the assumption of having quite identical copies of the quantum state under study which in practice does not apply [81].

Consider a photonic quantum system with the total number of dimensions $D{=}d^N$ in which N is the number of photons and d is the dimensionality of the observable to be measured for each photon. The density matrix of such system contains $d^{2N}-1$ independent elements. Mathematically, this means d^{2N} measurements give sufficient data to rebuild the quantum state of the system, however in practice—to account for drift and normalization in different bases—it is normal to perform an overcomplete number of measurements [60, 73, 82–84]. This increases the time required since there are more measurements. For instance, the minimum number of measurements required for the state tomography of a two photon $(N{=}2)$ qudit state (d dimension) is d^4, while $[d(d{+}1)]^2$ measurements are needed for an over-complete state tomography [60]. To overcome the restrictions that appear in this primary method of tomography—which is known as Standard Quantum Tomography (ST)—many proposals have been published [85–90] with the aim to minimize the number of measurements while still obtaining as much information as possible [91–93].

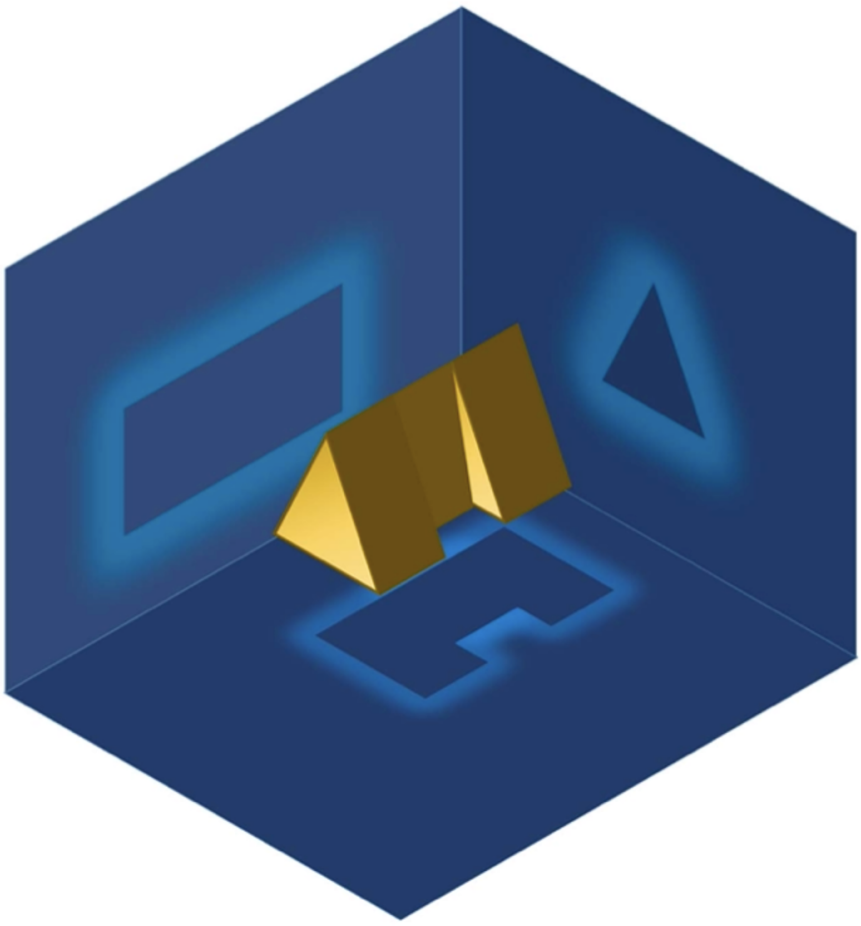

Figure 3.5: The aim for quantum state tomography is to rebuild a multi-dimensional complex quantum state through a series of projective measurements in every single dimension. It is similar to estimating the shape of a complicated object with a comprehensive interpretation of juxtaposing its shadows at different angles. (From [54]).

3.5 Brief Historical Review

Although the problem of inferring a quantum mechanical picture of a physical system has been of interest to researchers from the earliest days of quantum mechanics, the first systematic approach to characterize a quantum state through a complete set of measurements on identical copies of a system was first proposed in late fifties by Fano [71]. However, it was only in 1989 with a proposal by Vogel and Risken in which the tomographic measurements as we know it today was introduced [94] (the analogy of medical imaging in the topic of quantum state estimation was first raised there). Four years later, first experiments were accomplished to reconstruct the coherent and squeezed states [95]. Despite its successes, this primary method was not consistent to measure an unknown quantum state as it would introduce some arbitrary smoothing parameters which produce biases in the results. In 1995 D'Ariano et al. proposed [96] and then simplified [97] the first unbiased method which would resolve this problem. Based on their work, the first exact homodyne tomography experiments were done to characterize the photon statistics of a semiconductor laser [98] and the quantum state of a squeezed vacuum [99]. The satisfactory results achieved in first trials allowed researchers to apply this method to characterize numerous quantum states [100–106] such as atomic beams [107], vibrational modes of molecules [108], helium atoms [109] and single ions in a Paul trap [110].

In optics, the polarization degree of freedom of photons has received the most attention from researchers as it provides the simplest platform to study quantum optics phenomena. Since high-efficiency experimental elements are readily available it is a platform accessible to many research groups. As a result, many new achievements in the field of quantum optics have occurred using this property of light [111–114]. The same process applies to ST research and experiments by means of polarization [61, 115–117]. However, the relatively unexplored territory of other degrees of freedom is attracting more researchers every day [14–16, 43, 118–127].

Over the last few years, interest in high dimensional quantum states—qudits—has been rising since they provide a gateway to larger Hilbert spaces, offering advantages in many practical applications. For example, in the field of quantum communication, qudits give access to a higher information capacity [18], and noise resilience and robustness against eavesdropping [3]. They have also brought about many developments in the fields of quantum computation [128, 129] and quantum foundations [125, 130]. Despite all the advantages of qudits, their complex nature triggers many difficulties in their physical implementation, control, and measurement. These complexities in applying qudits have highlighted the weaknesses of ST and emphasized the need for a more efficient method. The main drawback as mentioned before is that quantum state characterization is a problem that becomes exponentially harder with the number of qubits: and even harder for qudits [131]. Meanwhile many proposals have been trying to improve the efficiency and precision of tomographic measurements by using state dependent methods [50, 51, 132–137], known as adaptive tomography. Furthermore, Maximum likelihood techniques have decreased the number of required measurements for tomography of the quantum states without losing precision [73]. But still the consistency of the results from ST is very sensitive to statistical noise and experimental errors regardless of the size of the system [2].

To solve this problem, we need a new method that is robust against noise and errors. At the same time, we do not want it to be affected by the exponentially growing post processing costs when the quantum states become more complicated. In answer to these requirements a new method was proposed by Ferrie [131] named as self-guided tomography (SGT) which meets all these needs to a very good extent. The experimental performance of SGT has been demonstrated in the case of qubits [2] and qudits [1] with satisfactory results. In the following, we talk about self-guided tomography in more details.

3.6 Self-guided Quantum Tomography (SGT)

SGT is a stochastic approximation procedure that does tomography following a recursive gradient ascent algorithm [138]. The point that distinguishes this method from other algorithms is that its tomographic measurements are based on optimization rather than quantum state estimation. In more detail, regardless of the system dimensionality, the SGT algorithm converges to the unknown desired state by iteratively maximizing its overlap with the current estimate through accomplishing a set of two projection measurements at every step. It is also an online method, meaning it does not keep the past measurements data. As the result, it provides robustness against statistical noise as well as experimental errors, while requiring a considerably smaller number of measurements, storage space, and processing time [131].

In every type of quantum state tomography, after providing an estimate of the quantum state that we are doing tomography process on, we need to determine how close the result is to the original state. In contrary with the standard quantum tomography and other prevalent methods in which an inverse problem gets solved to determine an accurate estimate of the true state using a set of projection data, in self-guided tomography we start by evaluating the distance measure between the desired state and a randomly chosen state, $m(\rho_2, \rho_1)$ in every step. Although we are free to choose any distance measure arbitrarily, the quicker it can be obtainable through the experiment, the more efficient will be the estimation process and so the more rapidly the algorithm converges. There are several different measures to specify the quality of the reconstructed state such as fidelity, concurrence, and linear entropy. We only address fidelity here as SGT utilizes this method. Fidelity is a measure of similarity between the estimated state and the target state. However, because of high levels of accuracy in the results of our experiments, we also utilize infidelity—i.e. (1−fidelity)—that gives a measure of the difference between the two states. Comparing the density matrices of the two states via the equation,

$$F = \left[\mathrm{Tr} \sqrt{\sqrt{\rho_1}\, \rho_2 \sqrt{\rho_1}} \right]^2, \tag{3.13}$$

gives a normalized benchmark of the operational quality of the estimation system: where 1 is a perfect match and 0 has the least similarity. ρ_1 and ρ_2 are the density matrices of the estimated and target states, respectively. This is the general definition which applies to both pure and mixed quantum states.

While for the case of a pure state, $\rho_1 = |\psi_1\rangle\langle\psi_1|$, Eq. (3.13) reduces as follows,

$$F = \mathrm{Tr}[\rho_1\rho_2] = \langle\psi_1|\rho_2|\psi_1\rangle, \tag{3.14}$$

which is in the form of an inner product of the two density matrices. The fidelity is a metric for distance from the target state; in the SGT algorithm it manifests itself in each iteration as a gradient approximation on two randomly chosen states $|\sigma_\pm\rangle$ with the expectation values $f(|\sigma_\pm\rangle)$. Based on these results the algorithm updates the current estimated state with one of the random states with higher fidelity to the target state. This procedure is repeated at every step until approaching the target state to the desired accuracy. Figure 3.6 demonstrates this trend for an arbitrary target state in a d dimensional Hilbert space, $\mathcal{H}_d$.

In order to find any arbitrary true state, $|\psi\rangle$, the starting point is irrelevant, and the algorithm may start from any point in the state space. Supposing we are at the step k and the current estimated state is $|\sigma_k\rangle$, the algorithm generates a stochastic direction $(\Delta_k)_j \in \{1,-1,i,-i\}$ and then along the positive and negative orientation of that direction performs projection measurements on two random states $|\sigma_\pm\rangle = |\sigma_k \pm \beta_k\Delta_k\rangle$, shown as the blue and purple vectors. Finally, through calculating the gradient,

$$g_k = \frac{f(\sigma_k+\beta_k\Delta_k) - f(\sigma_k-\beta_k\Delta_k)}{2\beta_k}\left(\Delta_k^{-1}\right)^* \tag{3.15}$$

the system updates the current estimate with

$$|\sigma_{k+1}\rangle = |\sigma_k + \alpha_k g_k\rangle, \tag{3.16}$$

in the direction with the highest expectation value. α_k and β_k are two functions that self-guided tomography calculates for each iteration in order to decrease the upcoming step size. Both functions simultaneously control the size as well as the rate with which the steps become smaller between iterations. Their parameters are user defined and follow

$$\alpha_k = \frac{a}{(k+1+A)^s}, \quad \beta_k = \frac{b}{(k+1)^t}, \tag{3.17}$$

where k is the iteration number and a, A, b, s and t are the hyperparameters.

3.7 Self Guided Tomography with Qubits

The first self-guided tomography trial was done by Chapman et al. [2] using the polarization degree of freedom of photons. A spontaneous parametric down conversion source was utilized as the light source [139] in which, one high energy photon transforms to two photons of lower energy—known as heralded single photons—where detection of one photon indicates the presence of the other. As Figure 3.7 shows, half- and quarter- waveplates are used to determine the polarization of the second photon. Together with a polarization beam splitter (PBS), they are also used for projective

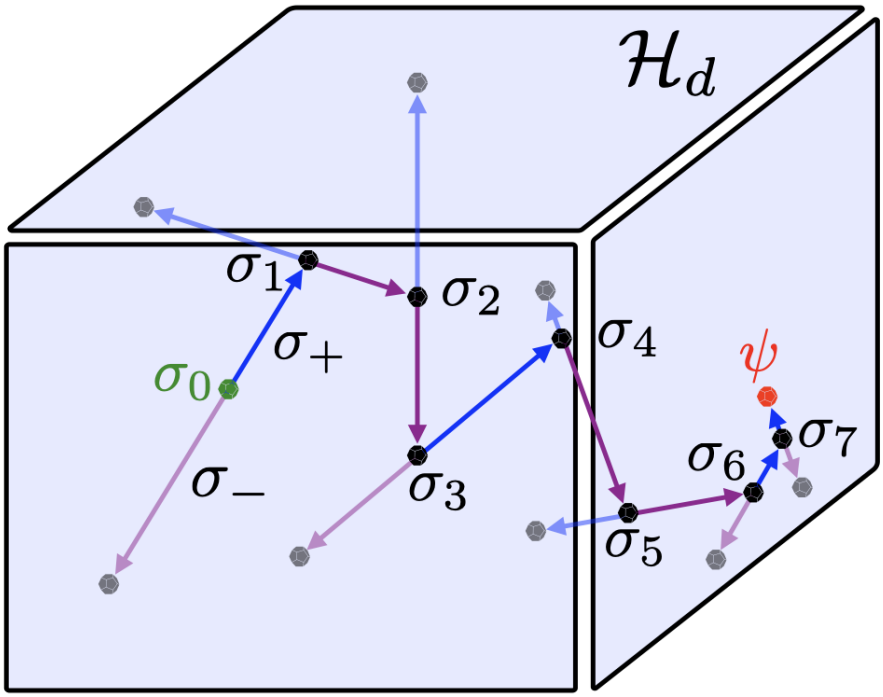

Figure 3.6: Graphical demonstration of self-guided tomography in an arbitrary Hilbert space of d dimension $\mathcal{H}_d$. The state ψ represents the unknown quantum state to be characterized (true state) and σ_0 is an arbitrary starting point. The blue and purple vectors illustrate the proposed state by the algorithm in each iteration. The algorithm estimates the best direction by measuring the overlap between the true state and the blue and purple projectors and thus it takes a step toward the higher expectation values and updates the current estimate of the state. This process becomes repeated for a pre-determined number of iteration until it converges to ψ. (From [1]).

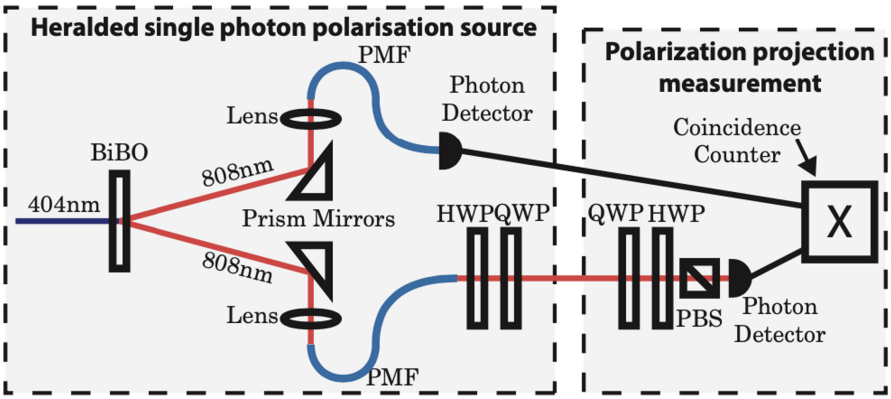

Figure 3.7: The experimental setup for self-guided tomography with qubits. Pairs of heralded single photons are produced via spontaneous parametric down conversion (SPDC). Directly detecting of one of the photons announces the existence of its twin. The polarization of the photon on the bottom path is encoded by passing it through a half- (HWP) and quarter- (QWP) wave plates. The subsequent HWP/QWP set—together with a polarization beam splitter—are responsible for the projection measurement on the encoded qubit of previous step. (From [2]).

measurements on that photon which make the projection into any pure qubit state feasible. The degree of overlap with the directly detected photon is measured through recording the photon counts on both paths and then calculating the proportion to the total over a certain period.

The results of self-guided tomography under high levels of statistical noise are shown in Figure (3.8a). The fidelity results of SGT for three different true states (red, green and purple points) demonstrate robustness against high levels of noise comparing with the average fidelity of standard quantum tomography on the same states, (blue points). The red dashed line is the mean fidelity results for SGT and the red band indicates the error range of one standard deviation. Figure (3.8b) compares the numerical fidelity data of SGT and ST against photon counts. According to that, while SGT reaches $99.3 \pm 0.2\%$ overlap with only about 280 photons involved in the measurement, ST requires one order of magnitude more photons to achieve the comparable results. This verifies that SGT has privileged performance in high noise regimes.

(a)

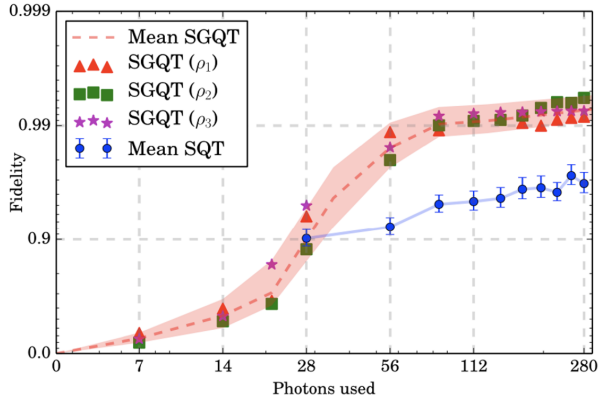

(b)

Method	Photon count	Fidelity
SQT	$\sim 2\text{x}10^5$	$99.9 \pm 0.1\%$
SQT	$\sim 3.9\text{x}10^3$	$99.5 \pm 0.7\%$
SQT	~ 280	$96.7 \pm 0.6\%$
SGQT	~ 280	$99.3 \pm 0.2\%$

Figure 3.8: (a) The red, green, and purple markers are the average fidelity of self-guided tomography for each one of the three target states under test, while the red dashed line represents the average fidelity over all of those. The blue points characterize the overall average fidelity obtained by standard tomography. (b) For the same number of photons ($N \sim 280$), under high statistical noise regime, self-guided tomography has a distinctive performance which standard tomography cannot reach unless with an order of magnitude more photons $\left(\sim 3.9 \times 10^3\right)$. A measurement with significantly higher number of photons is performed $N \sim 2 \times 10^5$) as the benchmark to evaluate the other results. (From [2]).

To evaluate the influence of measurement errors, the experimenters applied a large amount of uncertainty to the projection measurements by manipulating random orientations to the waveplates. The results are displayed in Figure 3.9. Four levels of uncertainty are applied to the waveplates during both SGT and ST measurements. Figure (3.9a) shows the average fidelities on each level for SGT (dotted lines) and ST (solid lines). Although the higher levels of uncertainty decrease the speed of convergence of SGT measurements with the cost of more iterations, SGT will continue its asymptotic flow toward higher fidelities. However, the ST results are not only highly dependent on these errors, due to the nature of this method they don't improve with number of iterations: as shown by the straight solid lines in Figure (3.9a).

(a)

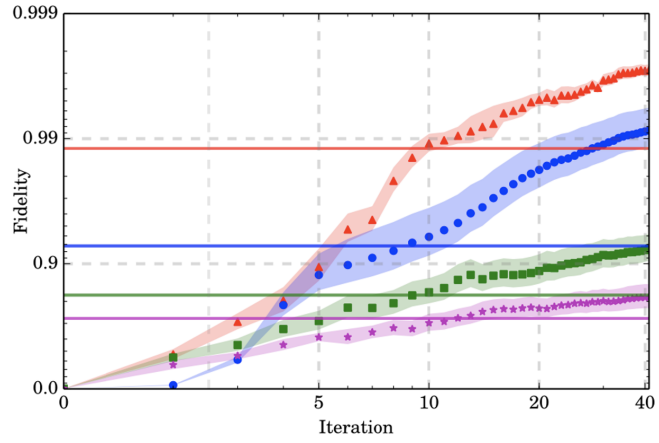

(b)

SQT 40 measurements (10 repeats)	SGQT 40 iterations
$98.8 \pm 0.5\%$	$99.72 \pm 0.03\%$
$92.8 \pm 1.2\%$	$99.2 \pm 0.3\%$
$82.2 \pm 3.5\%$	$92.5 \pm 1.8\%$
$72.6 \pm 4.6\%$	$81.1 \pm 4.0\%$

Figure 3.9: The performance of self-guided tomography in the presence of experimental errors. (a) Fidelity graphs of self-guided tomography (dotted lines) and standard tomography (solid lines) for four different levels of error. Each point is the average of ten measurements and the shaded areas represent one standard deviation of error. (b) Comparing the fidelity values of standard tomography (with ten repetition) and self-guided tomography (after 40 iterations). (From [2]).

Chapter 4

Self-guided Tomography with Qudits

4.1 Introduction

In our experiment we use the transverse spatial shape of single photons—described by Laguerre Gaussian modes characterized by two indices $\{l, p\}$—to encode the quantum states. So, any random quantum state can be written as the superposition of these modes $|\psi\rangle = \sum_i c_i |l_i, p_i\rangle$. As mentioned in Chapter 2, when using the transverse modes of light, the range of our bases is much wider than, and different from, just using the orbital angular momentum modes of light. This gives the advantage of having access to a larger set of modes to encode the quantum states. Another advantage is that we can choose a condition under which the spatial profile of the modes for any dimension d, does not rotate throughout the propagation length. The circumstance that fulfills this condition is to set the *Guoy phase* of the modes to the same order by applying the following relation,

$$d = 2p + |l| + 1. \tag{4.1}$$

Satisfying this condition does not require $p \neq 0$, i.e the modes do not have to have angular momentum.

Our setup includes two crystal Spatial Light Modulators (SLMs) which prepare the true state (Encoding-eSLM) and the estimated states (Measurement-mSLM) through displaying computer generated holograms, as shown in Figure 4.1.

An attenuated coherent light in $|0,0\rangle$ Laguerre-Gauss mode from an 807nm CW laser diode travels through two lenses and a set of half and quarter wave plates in order to align the polarization of laser beam with the orientation of the liquid crystal axes in the eSLM. The eSLM encodes the illuminated light to an unknown quantum state $|\psi\rangle$ and reflects it into a $4f$-lens setup—the diagonal beam path in Figure 4.1—that projects the image formed on the eSLM onto the mSLM. This path consists of two identical positive lenses with distance $2f$ of each other, while the input and the output planes are at a distance of a focal length before and after the first and the second lenses, respectively. The reflected light gets focused by the first lens towards an iris which excludes the light with all orders of diffraction but the first order. Then the second lens collimates the remainder of the beam toward the mSLM at which the overlap between $|\psi\rangle$ and the estimated state $|\sigma_k\rangle$ is measured. The light beam

reflected from the mSLM contains quantitative information about the degree of overlap between these two quantum states, $f(\sigma)=|\langle\sigma \mid \psi\rangle|^2$. After the mSLM, we spatially filter the beam by passing it through an iris and a single mode fiber: this minimizes the crosstalk between the target mode and other modes; after this the beam is sent to the detector. Computing the holograms on both SLMs, as well as data collection is controlled through a computer. The data regarding the overlap between the patterns prepared on the SLMs is measured via a silicon Avalanche photodiode detector (Perkin-Elmer AQR-14) coupled with a time tagging module (Swabian TT20). The counting rate of our detector is $\sim 10^5$ photons/s while the dark count is $\sim$300 photons/s. As already mentioned, at every iteration the system proposes two estimations $|\sigma_\pm\rangle$ along a random direction to measure their overlap with $|\psi\rangle$. Applying the experimental data for these two estimations directly in Eq. (3.15) gives

$$\begin{aligned} & f(\sigma_+) - f(\sigma_-) = f(\sigma_k + \beta_k\Delta_k) - f(\sigma_k - \beta_k\Delta_k) \\ \Rightarrow & \frac{|\langle\sigma_k + \beta_k\Delta_k \mid \psi\rangle|^2 - |\langle\sigma_k - \beta_k\Delta_k \mid \psi\rangle|^2}{|\langle\sigma_k + \beta_k\Delta_k \mid \psi\rangle|^2 + |\langle\sigma_k - \beta_k\Delta_k \mid \psi\rangle|^2} = \frac{N_+ - N_-}{N_+ + N_-}, \end{aligned} \tag{4.2}$$

in which $N_\pm$ are the registered number of counts correspond to the measurements done in the directions $\pm\beta_k\Delta_k$ at every iteration of self-guided tomography.

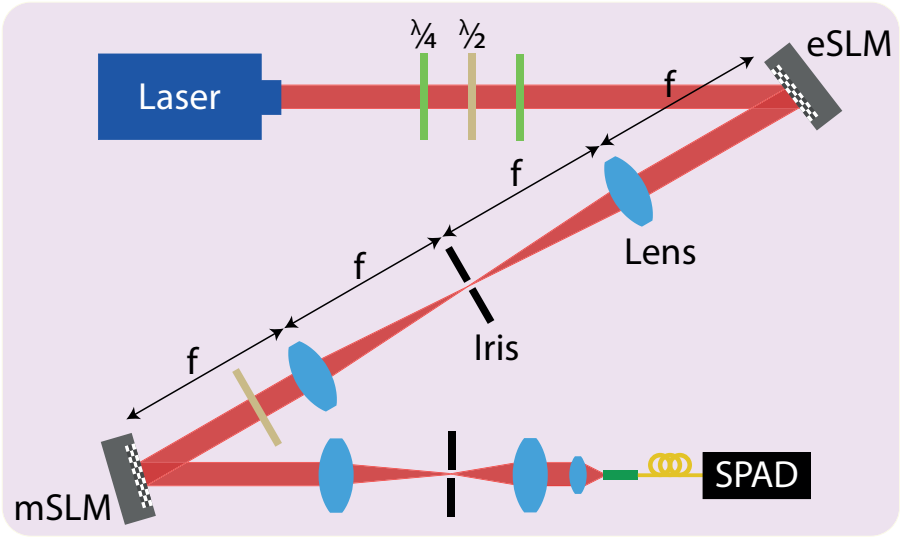

Figure 4.1: Experimental setup to evaluate the performance of self-guided tomography with the transverse spatial modes of light. The attenuated light from the laser passes through a set of half- and quarter waveplates which align the beam polarization with the orientation of the liquid crystal axes in the SLMs. The eSLM encodes the transverse shape of the illuminated beam to the qudit state $|\psi\rangle$ and reflects it to a $4f$-lens configuration which images the encoded state to the mSLM that is ready to measure the estimated state $|\sigma_k\rangle$. This projection measurement contains the data about the amount of overlap between the encoded and the measurement states. From there the light becomes redirected toward an iris and then a single mode fiber—both acting as spatial filters. After that a single photon avalanche detector (SPAD) registers the number of photons which is proportional to the overlap degree of $|\psi\rangle$ and $|\sigma_k\rangle$. This data is used to modify the estimated state $|\sigma_{k+1}\rangle$ in the next iteration. (From [1]).

As already introduced in chapter 3, the functions α_k and β_k are the hyperparameters to control the convergence. Although the numerical studies on a variety of different problems can approximate the range of values of these parameters, the optimal values, particularly for a,A, and b, must be found individually for each system. So before applying self-guided tomography to unknown qudits, we have examined different values for each of the hyperparameters to find their optimum values. To have comparable results, we pick one specific quantum state for a qutrit $(d{=}3)$ and always use the same starting point $|\sigma_0\rangle$ for the algorithm. The resulting infidelities can be seen in Figure 4.2. Our benchmarks for selecting the best coefficients is the convergence of the infidelity—i.e. $(1-\text{fidelity})$—as well as the rate of convergence, i.e. achieving the smallest infidelities in the least number of iterations. In every graph, the green line is the optimum result, although the behavior for the selected values is very similar. For example, Figure (4.2a) shows no significant change between the orange, green and red lines ($a{=}5,6$ and 7), with just the blue line ($a{=}1$) converging more slowly. The situation is similar for the green and red lines ($b{=}0.1$ and 1, respectively) in Figure (4.2b); both converge at a comparable rate, and the orange and blue line ($b{=}0.01$ and 0.001) with one and two orders of magnitude smaller values for b, respectively, converge very slowly. Figure (4.2(c-e)), showing the convergence results for s,t,A, respectively, further indicate the high robustness of these hyperparameters to large changes. Note, as self-guided tomography uses different random states in each iteration of each run, we expect slight deviations between consecutive measurements even for the same set of hyperparameters.

In this research we probed and compared the performance of self-guided tomography and standard quantum tomography for three different qudits: qutrits, $d{=}3$, ququints, $d{=}5$, and quvingints, $d{=}20$. First for $d = 3$, as the first qudit state space, second for $d = 5$ as a higher dimension which still makes it possible to compare the data collected for both methods, and then for $d = 20$ as a proof that self-guided tomography still works efficiently in a high dimension state space in which standard quantum tomography is not feasible neither in terms of run-time nor the required resources. For each d also three different regimes have been assessed: low statistical noise, significant statistical noise, and weak turbulence.

In our experiments, we picked the estimated state with a large number of iteration found through self-guided tomography as the true state $|\psi\rangle$. In the next section we discuss the considerations on this matter in more detail.

4.2 Considerations on the True Encoded State

The quality of state preparation is of high importance in the topic of quantum state estimation. Achieving higher degrees of fidelity will result in better compatibility between the simulated and actual quantum states. However, achieving this becomes increasingly harder as we increase the dimensions of the qudits. The performance of the tomography algorithm is impacted as the dimension of the Hilbert space is increased. To characterize this impact on the fidelities of different methods, we investigated the degree of overlap of different true state options: the theoretically encoded state $|\psi_{th}\rangle$, the state

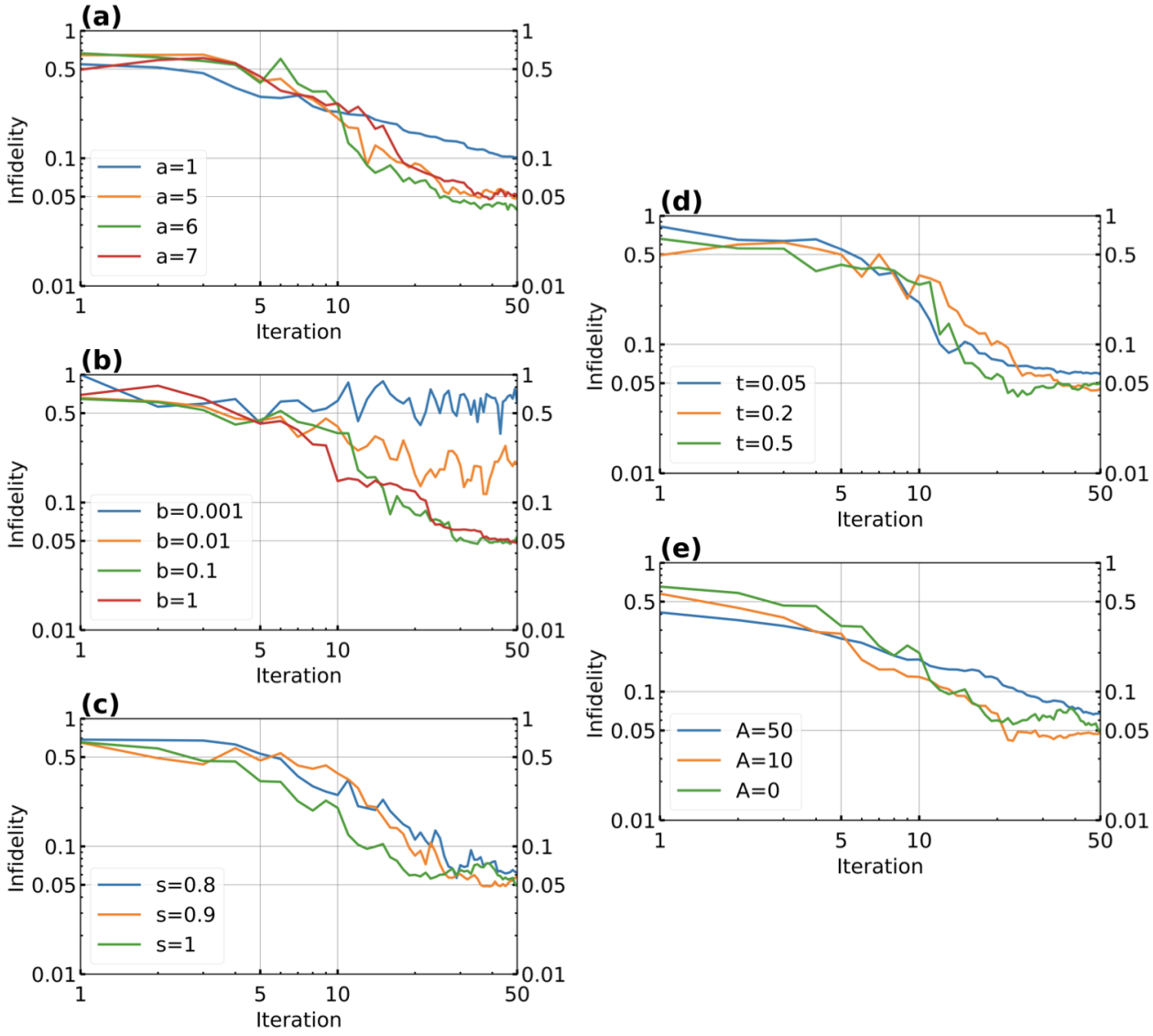

Figure 4.2: Experimental results for the infidelity as a function of iterations for different values of the hyperparameters, a, b, s, t, and A for d=3. Starting from (a), the optimal value of the corresponding parameter is substituted to perform measurements on the following parameter. (a) variation of the parameter 'a'; other parameters are kept unchanged, [a, 0.1,1,0.5,0]. (b) Varying 'b',[6, b, 1,0.5,0]. (c) Varying 's', [6,0.1, s, 0.5,0]. (d) Varying 't',[6,0.1,1, t, 0]. (e) Varying 'A', [6,0.1,1,0.5, A]. The green line in every graph indicates the optimal value of the corresponding hyperparameter selected in our experiment, however, all values within a certain range as large as one order of magnitude, e.g. in (b, d, e), result in similar convergence behaviour.

found by long measurements of overcomplete standard tomography $|\psi_{ST}\rangle$ and the state found by self-guided tomography after a high number of iterations $|\psi_{SGT}\rangle$. Table 4.1 shows the results. To reach higher fidelities with the standard tomography, we collected, $\sim$10 million copies of the unknown state in 10 seconds which is 10 times more than our regular measurements. To provide the true state using self-guided tomography, we added $5, 2.5$, and 4 times more iterations to the process comparing with our regular measurements for qutrit (500 iterations), ququint (500 iterations) and quvigint (2000 iterations), respectively. These numbers are chosen in a balance between time constraints and desired accuracy. From the data provided in the Table 4.1, regardless of the dimension, the degree of overlaps between the $|\psi_{ST}\rangle$ and either of $|\psi_{th}\rangle$ and $|\psi_{SGT}\rangle$ are much lower than that between $|\psi_{th}\rangle$ and $|\psi_{SGT}\rangle$. So, it

will be a poor choice to use $|\psi_{ST}\rangle$ as the true state, since its operation is too susceptible to any small imperfection or error in the system. For example, a major source of error in our system that highly affects standard tomography measurements is the mode dependent losses which cause nonuniform detection efficiencies for different modes. So, we decided to use $|\psi_{SGT}\rangle$ as the true state that as it can be seen from the table, provides high degrees of fidelities without any substantial vulnerability to the sources of error. Of course, another option would be picking $|\psi_{th}\rangle$ as the true state which would result in steady convergence toward higher (lower) fidelities (infidelities) with a lower rate.

Table 4.1: Pairwise fidelities of three considered true states: $|\psi_{th}\rangle$, theoretical true state; $|\psi_{ST}\rangle$, state found by overcomplete standard tomography on ~ 10 million copies of the unknown state; $|\psi_{SGT}\rangle$, true state found by self-guided tomography after 500 (qutrit and ququint) or 2000 (quvigint) iterations of the algorithm. The lowest fidelities are for the overlaps of standard tomography with theoretical true state and self-guided tomography, respectively. Therefore, clearly $|\psi_{ST}\rangle$ is not the best option to be used as the true state. On the other hand, regardless of the dimension, the overlap between $|\psi_{th}\rangle$ and $|\psi_{SGT}\rangle$ is always high. We chose $|\psi_{SGT}\rangle$ as our true state to minimize the preparation inaccuracies in calculations.

Dimension		$\|\psi\rangle_{\mathrm{SGT}}$	$\|\psi\rangle_{\mathrm{ST}}$
3	$\|\psi\rangle_{\mathrm{th}}$	$99.66^{+0.13}_{-0.19}$	$95.8^{+0.1}_{-2.9}$
	$\|\psi\rangle_{\mathrm{ST}}$	$96.3^{+1.0}_{-2.6}$	–
5	$\|\psi\rangle_{\mathrm{th}}$	$99.52^{+0.11}_{-0.26}$	$95.3^{+1.4}_{-1.4}$
	$\|\psi\rangle_{\mathrm{ST}}$	$96.2^{+1.6}_{-0.8}$	–
20	$\|\psi\rangle_{\mathrm{th}}$	$95.4^{+0.6}_{-3.8}$	–

Figure 4.3 shows the results of self-guided tomography under low statistical noise condition. The figures (a) to (c) show the results for qutrit (d=3), ququint (d=5) and quvigint (d=20), respectively. To draw these diagrams, we have used infidelity to provide a clearer view of the results. The dashed blue curves represent the experimental data which for the case of qutrit and ququint are the median of 50—and for the quvigint the median of 20—randomly chosen quantum states. The red solid lines are the simulated data achieved under the comparable condition with our experiment: the same count rate of $\sim$105 Hz, dark count rate, and technical noise (to simulate the alignment imperfections). Since the simulation process is much quicker than experiment, the results are the median of 1000 random states in order to obtain higher precision. The shaded area around each line covers the 25% to 75% uncertainty margin around the median. we have achieved the fidelities of $99.92^{+0.04\%}_{-0.17\%}$ for qutrit (after 100 iterations), $99.92^{+0.04\%}_{-0.07\%}$ for ququint (after 200 iterations), $99.1^{+0.2\%}_{-0.6\%}$ for quvigint (after 600 iterations). However, the asymptotic trend of self-guided tomography data in all the graphs denotes that any degree of accuracy is attainable at the cost of taking more steps toward the true state. As can be seen, although there is a nice consistency between the simulation and experiment of self-guided tomography for $d = \{3,5\}$, for $d = 20$ the theoretical curve is deviated slightly from the experimental data which indicates inadequacy of the noise model in higher dimensions. Noise analysis for the case of quvigint shows that while crosstalk is dominant between the modes adjacent to the diagonal, the simulated noise model considers the crosstalk evenly distributed among all modes. To learn more about the nature of the discrepancies between our simulations and our experiments in self-guided

tomography of higher dimensions, we now explore the prepare-measure correlation matrices.

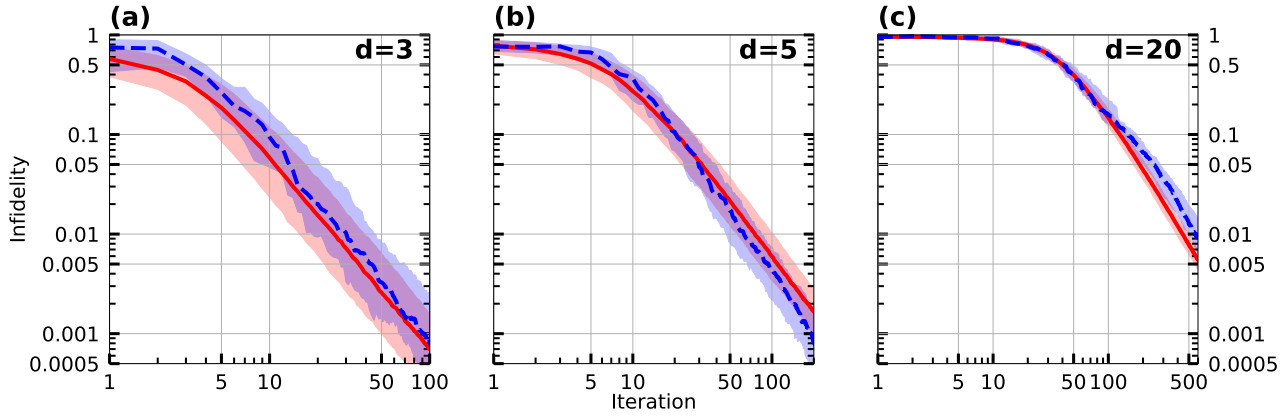

Figure 4.3: Self-guided tomography results for low statistical noise regime. The red solid lines represent the theoretical data while the blue dashed lines indicate the experimental results. The data is provided for (a) qutrit, (b) ququint, and (c) quvigint. The lines are the medians of the test results in each case, while the shaded regions cover the interval within 25% upper and lower of the fidelity median data. There is a nice consistency between theory and experiment for d=$\{3,5\}$. However, for d=20 there is a slight disagreement between the two which can be pertained to the inadequacies of the noise model in higher dimensions. Even so the shaded areas still overlap in this case. As we go to higher dimensions, there is a need for more iterations to obtain higher fidelities. For example, reaching 99% fidelity requires 29,62, and 566 iterations for 3,5, and 20 dimensions, respectively. Note that with the limitations of standard tomography, achieving such level of fidelity is practically impossible for quvigints. (From [1]).

4.3 Prepare-Measure Correlation Matrices

The prepare-measure correlation matrix is a $d\times d$ matrix which shows how well we can prepare and measure modes. The elements of the matrix are a measure for the overlap of the optical modes $\langle\sigma|\psi\rangle$, where $|\psi\rangle$ is the prepared mode and $|\sigma\rangle$ is the measured mode. Ideally, the matrix element will be high if we are preparing and measuring the same mode, and zero otherwise. Thus, the matrix shows the crosstalk between the orthogonal modes forming the basis set of our d -dimensional Hilbert space. We use transverse spatial modes of light as described by the Laguerre-Gaussian (LG) basis. To ascertain the accuracy of our measurements, we first experimentally derive the prepare-measure correlation coefficients for the states of the logical basis for each dimension d. It is important to ensure that the overlap between orthogonal modes is minimised.

The LG modes of light are prepared using two SLMs which encode the theoretical true state (encoding, eSLM) and measure the estimated state (measurement, mSLM). To measure each element of the prepare-measure correlation matrix, we prepare one of the eigenstates on the eSLM and measure it against all eigenstates on the mSLM. The maximum overlap is achieved when each spatial mode is projected onto itself resulting in a Gaussian beam shape which is then coupled into a single mode fibre and further to a single photon detector that records the number of counts.

To optimize the prepare-measure correlation matrix, the setup needs to be precisely aligned. Small degrees of misalignment in optical elements can result in significant overlap between orthogonal modes which appears as a none-zero off-diagonal correlation coefficient. We have measured the matrices for three different dimensions $d = 3, 5, 20$ as shown in Figure 4.4 in the left (simulation) and right (experiment) column.

We would like to highlight that in the experimental results, the off-diagonal matrix elements show some overlap between nominally orthogonal modes. This overlap is not equally distributed over the matrix but rather favours adjacent modes before quickly tapering off for more distant states. This implies there are mode-dependent correlations and losses leading to a complex dependence of the experimental errors on the encoded/measured modes. To compare the experiment with simulations we introduce the visibility V. It is defined as the ratio of the sum of diagonal entries to the sum over all matrix elements, i.e.

$$V = \frac{\sum_{i=1}^{d} N_{ii}}{\sum_{i,j=1}^{d} N_{ij}}, \tag{4.3}$$

where N_{ij} is the number of counts registered by the detector for encoded mode i and measured mode j. We reach a maximum experimental visibility of V=99.77±0.01% in our experiment for d=3.

Table 4.2: Experimental results for the visibilities of the prepare-measure correlation matrix for different dimensions given by Eq. (4.3). The uncertainties are calculated via error propagation of Poissonian counting noise.

Dimension	Visibility
$d = 3$	$99.77 \pm 0.01\%$
$d = 5$	$99.09 \pm 0.01\%$
$d = 20$	$97.64 \pm 0.01\%$

To simulate our experimental results, we recreate the experimental values for dark counts ($N \sim 10^2$–10^3) and counting noise ($\Delta N \sim 10^2$–10^3) and introduce a random noise parameter to simulate all other noise sources. We then use the parameters to calculate average visibilities and tune the noise parameter to recreate the experimental value. Unlike the experimental case, the simulated noise is uniformly distributed over all values N_{ij}. The mode dependent loss is different for each mode (superposition of modes) and largely depends on the efficacy of the phase-flattening. We did not implement these in the simulations and as a result, we expect some deviations between the theoretical and experimental results of the prepare-measure correlation matrix, especially for higher d where modes with a higher mode number have less counts compared to the modes that have a lower mode number, see Figure (4.4 c and f). This furthermore explains the mentioned differences between theory and practice of self-guided tomography of higher d with transverse spatial modes. Fortunately, the majority of the effect of mode-dependent loss is overcome by the self-guided tomography algorithm in our experiment as highlighted by the very small infidelities achieved in this research.

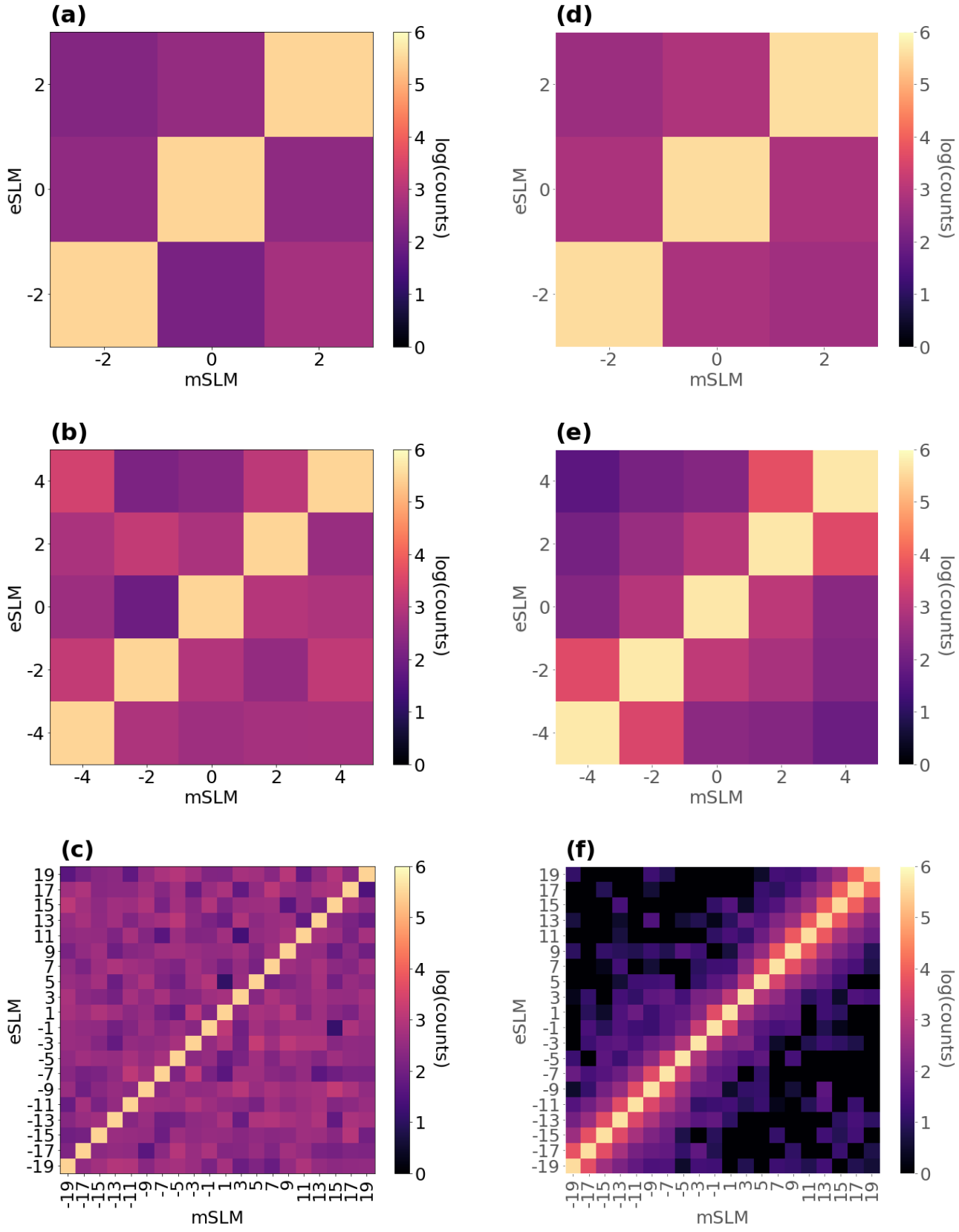

Figure 4.4: Comparison of simulated (a–c) and experimental (d–f) prepare-measure correlation matrices for different dimensions d=3, 5, 20, respectively. Each element of the matrix is determined by registering the counts when encoding one mode on the eSLM (vertical axis)—we show only the azimuthal index for brevity—and another mode on the mSLM (horizontal axis). The nature of the experimental crosstalk, favouring adjacent modes especially visible for higher dimensions, is different from our simulations which show uniformly distributed noise. We used the set of Laguerre-Gaussian modes for our experiment, but any set of orthogonal modes will suffice.

4.4 Self-guided Tomography in High Levels of Noise

In the next step, we implemented the self-guided tomography algorithm for low count rates to investigate its robustness to high statistical noise. To provide such a noise level, we decreased the number of copies of the quantum states per iteration, N. The number of counts has been reduced to around 8 counts—$\Delta N=\sqrt{N} \sim 9$—for d=3 and 5, and around 1200 counts—$\Delta N \sim 32$— for d=20 which resulted in fidelities of: $98.6^{+0.8\%}_{-1.3\%}$ for qutrits (after 100 iterations, Figure (4.5a); $97.6^{+1.2\%}_{-1.1\%}$ for ququints (after 200 iterations, Figure (4.5b)); and $95.1^{+1.0\%}_{-2.7\%}$ for quvigints (after 600 iterations, Figure (4.5c)). The graphs compare the experiment (dashed blue line) versus the equivalent simulated data (solid red line) for different dimensions. The experimental data shows continuing convergence to small infidelities, comparable with the theoretical results and highlights the robustness of self-guided tomography to high statistical noise. Similar to the high statistical noise condition, while the infidelities for lower dimensions still overlap within the shaded uncertainty regions, the simulation for the quvigint faces the same limitations as we already discussed.

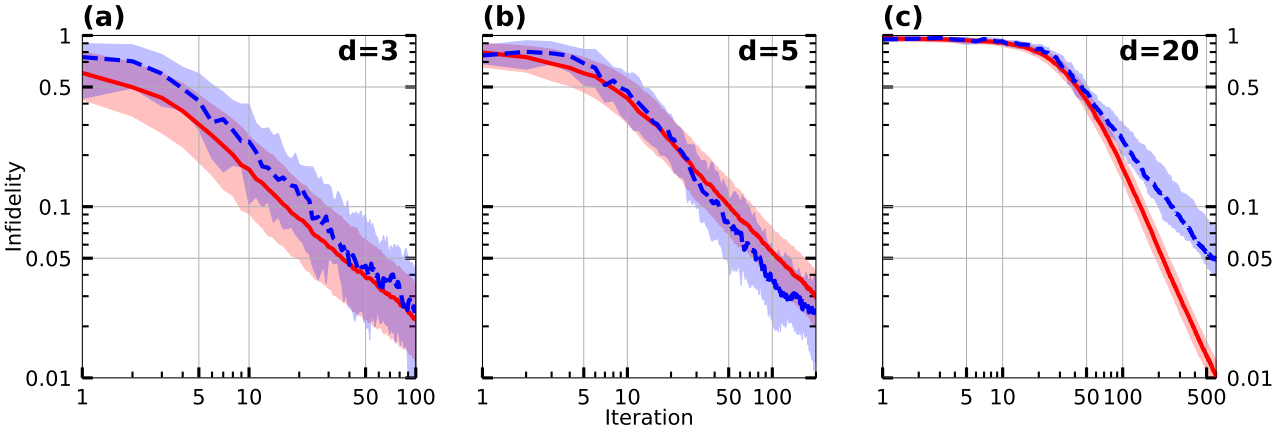

Figure 4.5: Self-guided tomography in the presence of high statistical noise for (a) qutrit in 100 iterations, (b) ququint in 200 iterations, and (c) quvigint in 600 iterations. The dashed blue lines indicate the self-guided tomography results under the presence of high statistical noise, whereas the solid red lines are the equivalent simulations. The shaded area around each line surrounds the data 25% above and below the median. Although the simulations predict the experimental results with high precision for d=3, 5, there is a slight deviation between the theory and experiment in the case of d=20, since the ability of the noise model to simulate the noise sources diminish in higher dimensions. (From [1]).

4.5 Self-guided Tomography in Turbulent Atmosphere

Atmospheric turbulence is a major source of fluctuations in optical communication systems. It particularly affects the transverse modes of light in both intensity and phase causing considerable deviation of the original shape. So as the third test of self-guided tomography we investigated the transmission of the light beam through a weak turbulent atmosphere. To do so we generated the

phase holograms using a theoretical approximation known as Kolmogorov thin-phase aberration which already has been tested on photons carrying orbital angular momentum [140–142]. The impact rate of turbulence in this simulation method is controlled by a set of parameters embedded in the formulation including the beam size, Fried parameter r_0, and the atmospheric turbulence strength C_n^2. To simulate a weak turbulence atmosphere, we chose C_n^2=10^{-18} $\mathrm{m}^{-2/3}$ in a transmission distance of $Z\sim$1 km resulting in a phase value range of $\sim(-\pi/5, \pi/5)$. The relation is

$$r_0 = 0.185 \left(\frac{\lambda^2}{C_{\mathrm{n}}^2 \cdot Z} \right)^{\frac{3}{5}}, \tag{4.4}$$

where λ is the light beam wavelength. Using the selected parameters, the intensity profiles are comparable to Krenn et al. [143]. As discussed earlier in section 2.6.2, Kolmogorov turbulence approximation governs the exponent and pre-factor. Although we considered C_n^2 to be constant in our experiment, for real conditions the values of C_n^2 and consequently r_0 are strongly influenced by several items such as location,—e.g. urban vs. country areas, altitude—time of the day, atmospheric condition, and the photonic mode size. In our experiment, the beam diameter D is about 1 mm which is rather small comparing with experiments done under real life condition—in the order of several centimeters—e.g. in [143]. The ratio between D and r_0 is an important scale of the mode shape susceptibility to the detrimental effects of the environment. According to the works done on optical angular momentum of dimensions up to 11, an acceptable stability was obtained for D/r_0<0.1 [142]. In our experiment, we set our parameters such that $D/r_0 \ll 1$ which easily satisfies this stability condition.

In order to minimize the simulation time of the phase hologram (which scales up with the total number of pixels) and also to avoid boundary effects, we chose its dimensions just large enough to fully cover the cross-section of the beam. For the beam diameter of 1 mm, our phase hologram dimensions were 150 by 150 pixels ($\sim$1.4$\times$1.4 mm) projected on the measurement state hologram. An instance of these generated screens is shown in Figure 4.6. At every measurement, we generate a new phase hologram and append it on the mSLM to the hologram of the state. This makes the simulation match well with the dynamic nature of the atmosphere.

Figure 4.7 compares the self-guided tomography results for high statistical noise (green dotted line) and weak atmospheric turbulent condition (purple dash-dotted lines). The sturdy operation of the algorithm is observable, leading to fidelities of $99.4^{+0.4\%}_{-0.6\%}$ for qutrits (after 100 iterations, Figure (4.7a)), $99.2^{+0.3\%}_{-0.5\%}$ for ququints (after 200 iterations, Figure (4.7b)), $96.8^{+1.0\%}_{-1.8\%}$ for quvigints (after 600 iterations, Figure (4.7c)). It is noteworthy that regardless of the type of noise in the system, the infidelity curves continue their descending trend allowing any desired accuracy to be achieved at the cost of more steps. This will be of more importance when the issue of quantum communication is raised in higher dimensions.

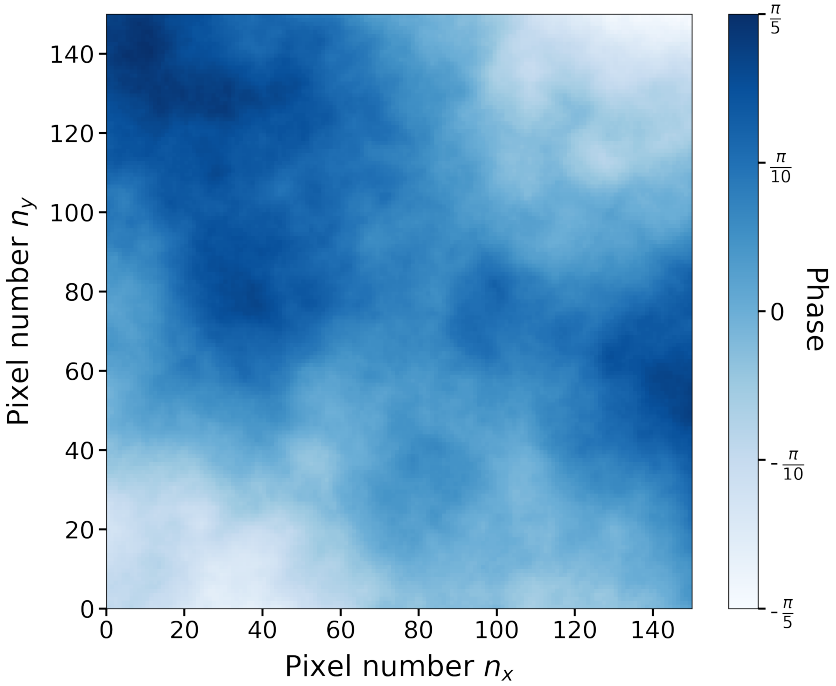

Figure 4.6: A sample phase screen to simulate the atmospheric turbulence. In order to avoid long simulation times, the size of phase screen is chosen 150 by 150 pixels, approximately 1.4 by 1.4 mm which is large enough to surround the cross-section of the beam. The phase variation range is $\sim\pm\pi/5$, specified in the spectrum between white and dark blue. The turbulence holograms were displayed on the mSLM together with the hologram of the estimated quantum states. (From [1]).

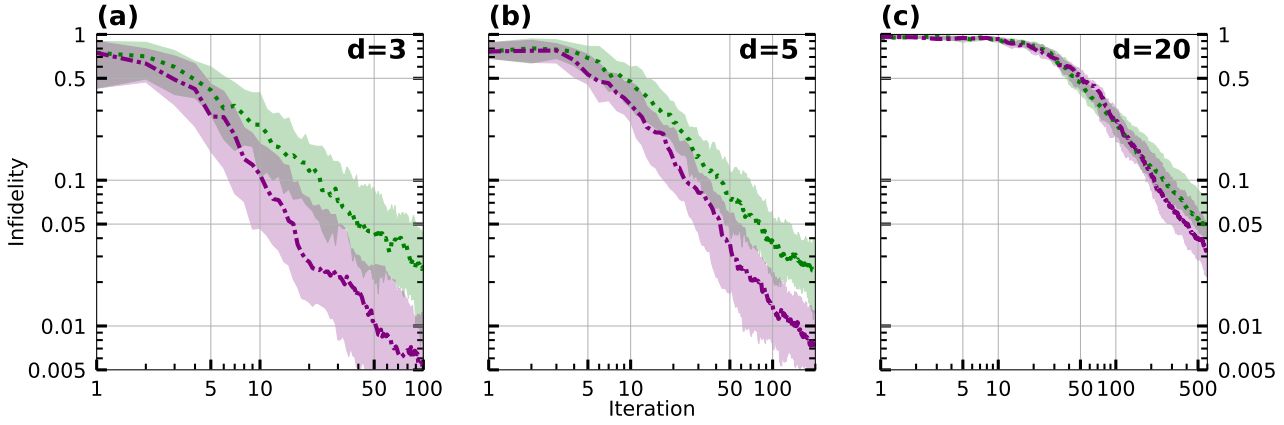

Figure 4.7: Self-guided tomography results for high statistical noise (dotted green line) and weak atmospheric turbulence (dash-dotted purple line) for (a) qutrit, (b) ququint, and (c) quvigint. The lines are the median performance, and the shaded areas cover the region between 25% upper and lower bands of the median infidelities ($(50 \pm 25)\%$). For all dimensions and under any condition, the infidelity results follow a descending trend. It indicates the robustness of self-guided tomography against imperfect environmental and experimental conditions. This ensures that any arbitrary precision is achievable just at the cost of more iteration. (From [1]).

To form a better understanding of comparing two methods, Figure 4.8 shows the tomography results for self-guided and standard tomography in 3 and 5 dimensions for which a fixed number of copies of the unknown states is used.

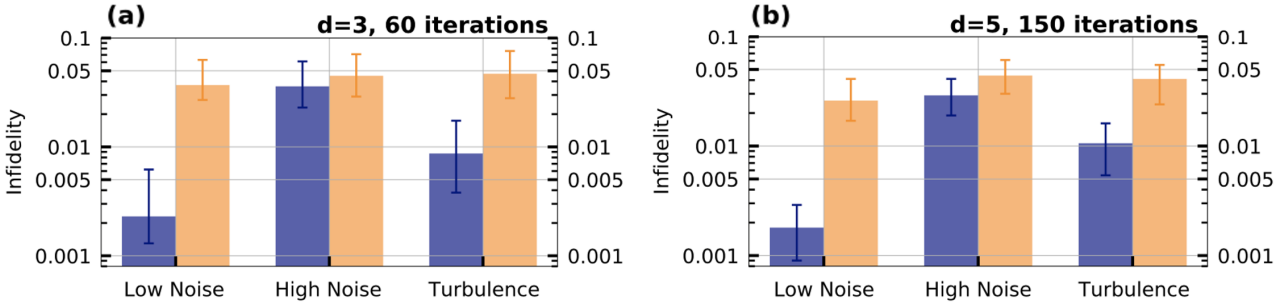

Figure 4.8: Fidelities obtained by self-guided tomography (blue) vs. standard tomography (orange) for the same number of copies of the (a) qutrit, (b) ququint unknown states. The left, middle, and right pairs of bar graphs are respectively for low statistical noise, high statistical noise, and weak turbulence. On average, self-guided tomography outperforms by a factor of $\approx 15, 1.4$, and 5 , respectively in these regimes. It should be noted that self-guided tomography is still prone to converge to higher fidelities with more iterations. However, at the consequence of mode-dependent losses in our system, the fidelities achieved by standard tomography are fundamentally limited to the presented values. (From [1]).

In the process of standard tomography, we exploited maximum likelihood and root estimators [144] in measuring the full array of mutually unbiased bases (MUBs). For example, for a qutrit there are total of 12 states which are made of four bases, each one having three states [145]. Note that in practice standard tomography is not feasible in the case of quvigints, as it requires an overcomplete set of 780 states to be measured (as in [75, 146]) and then further demands considerable post-processing.

We realized that no matter which dimension we are working on, standard quantum tomography is unable to reach infidelities lower than a few percent range. However, as already mentioned there is no such restriction for self-guided tomography as it continuously steps toward more accurate results by taking more steps (Figure 4.3 and Figure 4.7). It also works more efficient than standard tomography as it reaches lower infidelities for the same number of copies of the state. Figure 4.8 affirms this by showing average of $15\times$, $1.4\times$, and $5\times$ improved infidelities for low noise, high noise, and weak turbulence, respectively.

Table 4.3 represents the theoretical and experimental numerical data collected for self-guided tomography in all three dimensions under test as well as standard tomography data for qutrits and ququints. The data attained by both methods are for a fixed number of copies of the unknown state that makes them comparable in terms of efficiency (the accuracy and operating speed in estimating the unknown state) and required resources. To obtain more precise results for standard tomography on qutrits (ququints), each measurement was repeated ten times, therefore in total it was $120(300)$ experiments corresponding to $60(150)$ iterations in self-guided tomography, since each iteration of self-guided tomography contains two measurements. It is clear from the table that for self-guided tomography the experimental data are well fitted in the uncertainty ranges of simulated results. Also, independent of the dimension of the system, the fidelity values achieved through the standard tomography method do not exceed a certain range. The major cause of that is the existence of mode dependent losses in our system. While this imperfection has no effect on the efficiency of self-guided tomography.

Table 4.3: Fidelity data of self-guided tomography (SGT) vs. standard tomography (ST). To be comparable, an equal number of measurements for both self-guided tomography and standard tomography are performed (for d=3,5). In the case of quvigints for which standard tomography is not practically possible, we consider the least necessary number of measurements equivalent to an over-complete tomography [146] ($\sim$ 800, i.e. 400 iterations). All the fidelities are the medians over the number of repetitions, and the uncertainties cover the range of median $\pm 25\%$. sim$\equiv$ simulations with 1000 random states; exp$\equiv$ experiments with 50 and 20 random states for d=3,5 and d=20, respectively. (From [1]).

	Qutrit, d = 3			Ququint, d = 5			Quvigint, d = 20	
Iterations	Self-guided 60		Standard -	Self-guided 150		Standard -	Self-guided 400	
	sim	exp		sim	exp		sim	exp
Low noise	$99.81^{+0.12}_{-0.25}$	$99.77^{+0.10}_{-0.39}$	$96.3^{+1.0}_{-2.6}$	$99.72^{+0.11}_{-0.20}$	$99.82^{+0.09}_{-0.11}$	$97.4^{+0.9}_{-1.5}$	$98.80^{+0.25}_{-0.31}$	$97.9^{+0.3}_{-0.8}$
High noise	$96.6^{+1.4}_{-2.2}$	$96.4^{+1.3}_{-2.5}$	$95.5^{+1.6}_{-2.6}$	$96.2^{+1.2}_{-1.6}$	$97.1^{+1.0}_{-1.2}$	$95.6^{+1.4}_{-1.7}$	$98.11^{+0.37}_{-0.40}$	$93.5^{+0.8}_{-3.8}$
Turbulence	-	$99.13^{+0.49}_{-1.49}$	$95.3^{+1.9}_{-2.9}$	-	$98.94^{+0.52}_{-0.55}$	$95.9^{+1.7}_{-1.0}$	-	$95.0^{+1.4}_{-2.8}$

4.6 Self-guided Tomography on Mixed Quantum States

When the state preparation process is not well controlled, obtaining a mixture of the pure states is unavoidable. As this may happen in almost any practical situation, it is worthy to examine the performance of SGT in this case. Of course here the quantum state estimation process changes to density matrix estimation. For this aim we adjusted the algorithm parameters as well as the Hyperparameters to run a test on 3-dimensional mixed states. A qutrit density matrix has nine elements randomly distributed in the positive or negative directions of each measurement step. We applied the same protocol to define the step size and direction as our work with pure states. This parameterization process eventually results in 3 eigenvalues $v_{\pm,k}$ and eigenvectors $\vec{w}_{\pm,k}$. By displaying these eigenvectors on the measurement SLM, we measured the probability distribution of the unknown mixed state.

$$p_{\pm,k,i} = n_{\pm,k,i}/N_{\pm,k}. \tag{4.5}$$

$n_{\pm,k,i}$ are the photon counts corresponding to the overlap with the ith eigenvector, $\vec{w}_{\pm,k,i}$ and $N_{\pm} = \sum_i n_{\pm,k,i}$ is the sum of the counts for all eigenvectors. The gradient for the jth component at iteration k is

$$g_{kj} = \frac{f\left(\sigma_{+,k}\right) - f\left(\sigma_{-,k}\right)}{2\beta_k \Delta_{kj}}, \tag{4.6}$$

while in the case of work with mixed states, the $f(\sigma_{\pm})$ is no longer simply a pseudo-normalized probability but the quantum relative entropy

$$f\left(\sigma_{\pm,k}\right) = \sum_i p_{\pm,k,i} \log\left(v_{\pm,k,i}\right). \tag{4.7}$$

Note that while we have used the entropy, for this aim any quick function used in the estimation and optimization process could be used. The mixed state fidelity in this case requires a full tomography that contradicts our goal in utilizing self-guided tomography. The density matrix of the estimated mixed

state is as Eq. (4.8). We wouldn't expect it to be fully decohered so we wouldn't use a maximally mixed state. To make a mix state, we need to randomize the states that we prepare, so we can create the statistics of a mix state by randomly sampling from different states.

$$\rho = \begin{pmatrix} p_1 & 0 & 0 \\ 0 & p_2 & 0 \\ 0 & 0 & p_3 \end{pmatrix} \tag{4.8}$$

The diagonal elements sum to one,

$$\sum_m p_m = 1. \tag{4.9}$$

The procedure to specify the density matrix, ρ is to randomly pick one of the logical bases, $(|0\rangle, |1\rangle, |2\rangle)$ at each iteration while their probabilities, p_i are distributed unevenly. The selected basis becomes encoded on eSLM at each step of measurement.

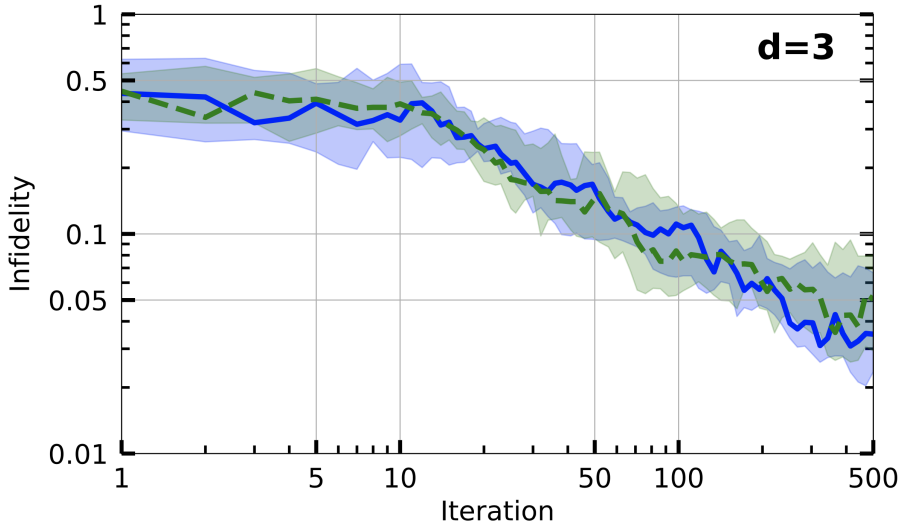

Figure 4.9: Self-guided tomography on qutrit mixed states. The blue solid (dashed green) line represents low (high) statistical noise regime. The lines are medians and the shaded areas demonstrate the data 25% above and below the lines. (From [1]).

The results for high and low statistical noise are displayed with dashed green and solid blue lines, respectively. The total number of counts, $N_{\pm}$ is about 800000 in low noise regime while it is just about 800 in high noise regime. we tested 20 randomly chosen mixed qutrits with purities $P \equiv \mathrm{Tr}\left(\rho^2\right)$ in the range 0.34 to 0.88. For 500 iterations of self-guided tomography these fidelity results are achieved: $96.5^{+1.1}_{-3.2}\%$ $\left(88.9^{+5.2}_{-2.8}\%\right)$ after 500 (100) iterations in the low noise case, and $94.9^{+2.2}_{-2.9}\%$ $\left(91.6^{+3.3}_{-5.9}\%\right)$ for high statistical noise. The theoretical results after 500(100) iterations shows 99.1% (93%) fidelity which is slightly more than the experimental data as expected. The asymptotic behavior of the trending line clearly shows the power law relation between the infidelity in vertical axis and the number of iteration in the horizontal axis. The satisfactory results of applying self-guided tomography on mixed qutrits even under the effect of high statistical noise promise the reliability of this method for practical situations and high dimensional quantum systems which can be the subject of further researches.

Part II

Nanofabrication of Lithium Niobate Integrated Circuits

Chapter 5

Edge Coupler Design for LN Integrated photonics

5.1 Efficient Quantum Router for Real-world Quantum Networks

In today's world, we are witnessing rapid and extensive progress in a variety of quantum technologies, with applications such as computing, sensors, simulation, and imaging. Connecting quantum devices to harness the full potential of these advancements requires a quantum network. An optical quantum network is the best option—similar to the classical networks—in terms of supporting high bandwidth, low operational costs, as well as overcoming on distance limitations via utilizing the speed of light and flexibility of optical fibers. However, in addition to these, a quantum network should possess some specific traits like having high efficiency, being ultra-low loss, and having the ability to support quantum features like coherence. To enable higher bandwidth, such a quantum network can support qudits, for example time-bin qudits which can be used in this project.

Although there have been several theoretical proposals to construct quantum networks, to date no fully quantum network has been built, because the real-world capabilities are lacking behind theory targets [147]. Generally, quantum network proposals have taken two different approaches. One is just to utilize linear photonic elements, where delay line play the part of memory; the second is to use both linear and nonlinear photonic components.

In this research, the goal of our team is to construct an efficient, robust, and fast quantum router that fulfills the requirements needed in a real-world quantum network. What makes this project practically unique is to take advantage of the exceptional properties of lithium niobate by utilizing the new essential discoveries in the Laboratory of Nanoscale Optics at Harvard [148]. Lithium niobate (LN) is the preferred optical platform for this project, since it has exceptional features which make it more suitable than silicon-on-insulator design of quantum routers. Namely: low loss rates in nanophotonic designs a hundred times better than silicon; three times more effective coupling to optical fiber; and fast electro-optic switching. The specific optical property expected of a material to be considered as a viable stage to apply nanophotonic designs on is to support active switching in the order of GHz

while still keeping the loss rates extremely low. Although LN thin film on insulator has been known as a very low loss structure for years [149], the issue of partially confining the optical modes typically reduce its effectiveness and speed of active switching.

In 2017 the Loncar group [148] showed that it is possible to have tight confinement of modes inside the LN waveguide while keeping the losses low. There have been some reports of successfully applying this new technique, which has resulted in promising outcomes [150, 151]. These breakthroughs in the fabrication process of LN thin-film are due to the recent developments in nanofabrication related technologies. These technologies, namely:

1. Improved lithography facilities to implement high-resolution patterns,
2. Inductively coupled Plasma-Reactive Ion Etching (ICP-RIE) technique to produce better-defined structures,
3. Plasma Enhanced Chemical Vapour Deposition (PECVD) to attain smoother and more homogeneous structures, and
4. Advanced modelling platforms like Lumerical Solution Software to design complex combinations of optical and electrical structures,

have been critical game-changers in enhancing the quality and precision of LN nanofabrication.

5.2 Approaches and Methods

A quantum router is a key component in universal linear-optics quantum computing. It has been proven by Rohde [152] that the device shown in Figure 5.1, containing two embedded fiber loops, a single photon source, three dynamically controlled beam-splitters, and a single time-resolved photodetector is a universal unitary, as it is the temporal equivalent of the Reck-Zeilinger universal unitary [153] and therefore qualified to be used for quantum computation purposes. The size of such a device depends on the materials used in different parts which specifies the refractive index of the photons. Other influential parameters on the circuit size are the lengths of the inner and outer loops which are dependent on the frequency of the photon pulses from the source as well as the number of photon pulses, n, in the circuit. So, in order to construct this device as our quantum router, the framework of the full quantum router project is divided into four subsections which are as follows:

1. Developing efficient fiber-to-chip coupling mechanism,
2. Providing efficient design of on-chip delay loops for Quantum Router timing,
3. Investigation for efficient switching rate designs,
4. Demonstration of the Quantum Router operating inside a quantum network.

As can be seen, in the first half of the project, the main focus is on the design optimization of the coupling structures and delay loops as the building blocks of the quantum routers. While on the second half, the primary focus is to construct an efficient composite structure of the components achieved in the first half as well as optimization of the initial product in real-world conditions in a compact but scalable quantum network. In this research our focus is on the first segment of the overall project, however, at this point let us talk about each step in more detail.

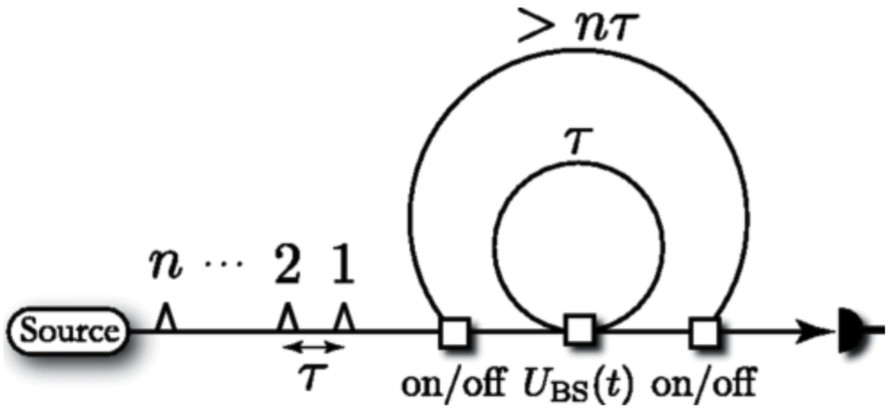

Figure 5.1: The schematic view of the Universal Quantum Processor. A beam splitter as an active element does the universal operations by inserting a fraction of the coming pulse into the inner loop and interacting it with the next pulse. The remainder of the first pulse goes through the outer loop to implement arbitrary transformations in the case of switch on or will be guided out of the device to be detected when the switch is off. (From [152]).

1. Developing efficient fiber to chip coupling mechanism. When we couple the light from an optical fiber into a nano-size waveguide, there is a huge difference between the mode field diameters in the fiber and the waveguide. The main goal here is to provide an efficient design to overcome the mode mismatch between the optical fiber and the nano-size waveguide. There has been a proposal that suggests an inverse taper structure to resolve this issue [154]. Such a design has shown a significant increase in the coupling between fiber and silicon-based chips, Figure 5.2. Other trials in this field have confirmed very low coupling losses in the range of 0.25dB for the mode diameter of $3\mu m$ and 0.5dB for $1.5\mu m$ modes [155, 156]. Our target diameters for the LN chip design are in this range as well. So, at this stage, I searched for the most efficient taper designs, and targeted mode sizes to improve the coupling losses to below 1dB. The first approach I am going to take is to modify the guiding taper shown in Figure 5.2 for our system. In case this approach does not meet our low-loss expectations, there are some alternative methods: **i**. exposed cantilevers [155]; and **ii**. inverse multimode splitters [157] where multiple smaller waveguides transfer the optical mode to a broad mode combination region. As a member of this project, my task is to investigate the most efficient coupling design.

2. Providing efficient design of on-chip delay loops for Quantum Router timing. For a real-world quantum network, it is necessary to provide a design which ensures high temporal flexibility. Delay loops are the structures considered for such a task. The aim of the second part is to design a minimized loss waveguide on LN which satisfies this timing property of a quantum network.

3. Investigation for efficient switching rate designs. In the third segment of the project, the main goal is to investigate the optimal electro-optical switching design that provides fast switching rates while still keeps the loss rates low.

4. Demonstration of the Quantum Router operating inside a quantum network. In the last part of this project, our team will examine the operational capabilities of our developed structure over the previous three steps by deploying it in a quantum network.

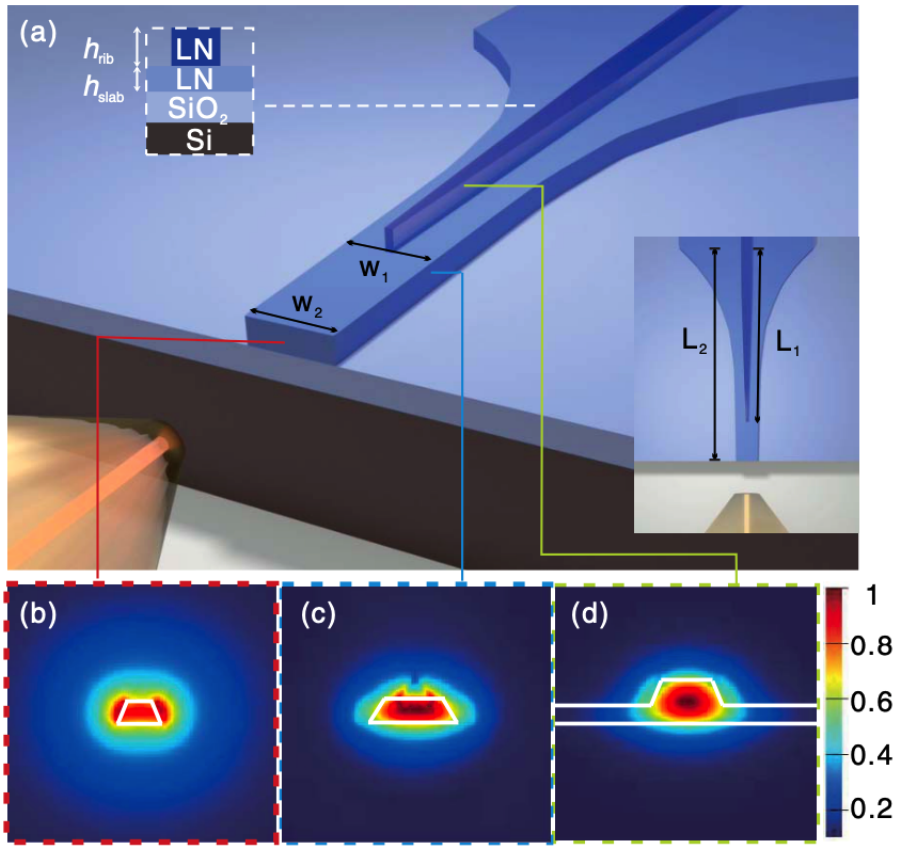

Figure 5.2: (a) A schematic view of the bilayer LN edge coupler designed and optimized to support a transverse electric (TE) optical mode. It is built of a tapered rib waveguide (of length L_1) on an adiabatically tapered slab layer (of length L_2). (b) to (d) display the variation of the beam cross-section while propagating through the coupler. The (TE) optical mode at (b) the tip of the slab waveguide with the width of W_2, (c) just before the connection point of the rib and slab layer with the slab width of W_1, and (d) bilayer region. (From [158]).

5.3 LN Photonics Edge Coupler

In Silicon-on-Insulator (SOI)-based photonics, the standard method to couple the light between the single mode fiber and any other photonic device—such as modulators, lasers, and detectors—is *edge coupling*. These couplers transform the highly confined mode of the waveguide to a larger mode of a fiber by gradually transforming the mismatches in the mode-size and the effective index of both sides of the junction. The main advantages of using edge couplers are their broadband response, low insertion loss—lower than 0.5 dB [156, 159]—and supporting both TE and TM modes. However, in conventional integrated lithium niobate (LN) photonics, despite the high performance and very low

on-chip losses ($\sim$ 0.03-0.1 dB/cm), their utilization has been challenged due to lossy fiber-to-chip coupling ($\gtrsim$ 10 dB/facet) [160, 161]. In 2019, the Loncar group in Harvard [158] proposed a low-loss mode size converter which demonstrates the coupling loss lower than 1.7 dB/facet between a standard lensed fiber and micrometer-scale LN rib waveguides.

The inversely tapered design increases the optical mode size on the chip, resulting in reduction of the insertion loss as well as improvement of the alignment tolerance during the assembly process of the integrated circuit. As seen in Figure 5.2(a), the mode converter is bilayer, consisting of a tapered rib waveguide on top of a tapered slab layer: both rib and slab are inversely tapered. Beneath the two layers is the buried layer of silicon oxide and beneath that the silicon substrate. Single layer inverse taper couplers, similar to the one proposed in [154], are not readily applicable in lithium niobate (LN) photonics. In an LN integrated circuit, the rib waveguide is a critical part of the design in order to couple the electric field efficiently into the slab waveguide. However the rib-only tapered structure poorly transmits the optical mode between the rib and slab. To overcome this problem, in the design shown in Figure 5.2 the slab waveguide is adiabatically tapered as well. Such a bilayer taper design gradually reforms the rib waveguide mode to a symmetric quasi-circular output mode. Figure 5.2 (b) to (d) demonstrates the gentle transformation of the input mode through the rib and slab waveguides.

In order to model and optimize this design, I used Lumerical solution software in 3D-FDTD (Finite Difference Time Domain) mode. The performance of this mode size converter as reported in the reference [158] is as shown in Figure 5.3. In this graph, the fiber-to-fiber transmission of the LN integrated ring resonator with and without the tapered coupler as a function of wavelength is drawn. The results show a reduction in coupling loss—from 11-14 dB (gray curve) to 3-5 dB (red curve)—in all range of the tested spectrum (1480 nm to 1680 nm).

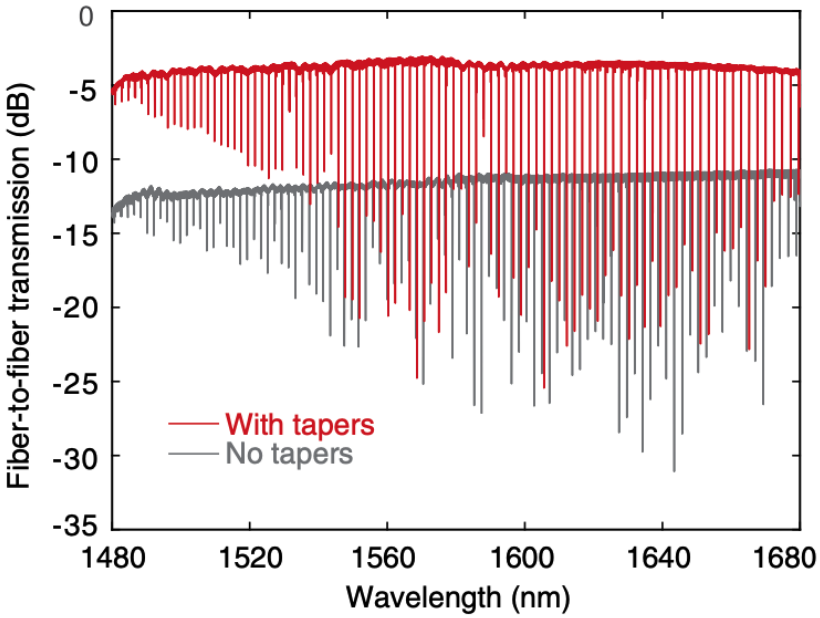

Figure 5.3: The fiber-to-fiber transmission loss diagram of a LN integrated ring resonator with (red curve) and without (gray curve) tapered coupler design introduced in Figure 5.2. The coupling loss has decreased from $\sim$ 11–14 dB with no tapered coupler to $\sim$ 3–5 dB with the bilayer tapered coupler. (From [158]).

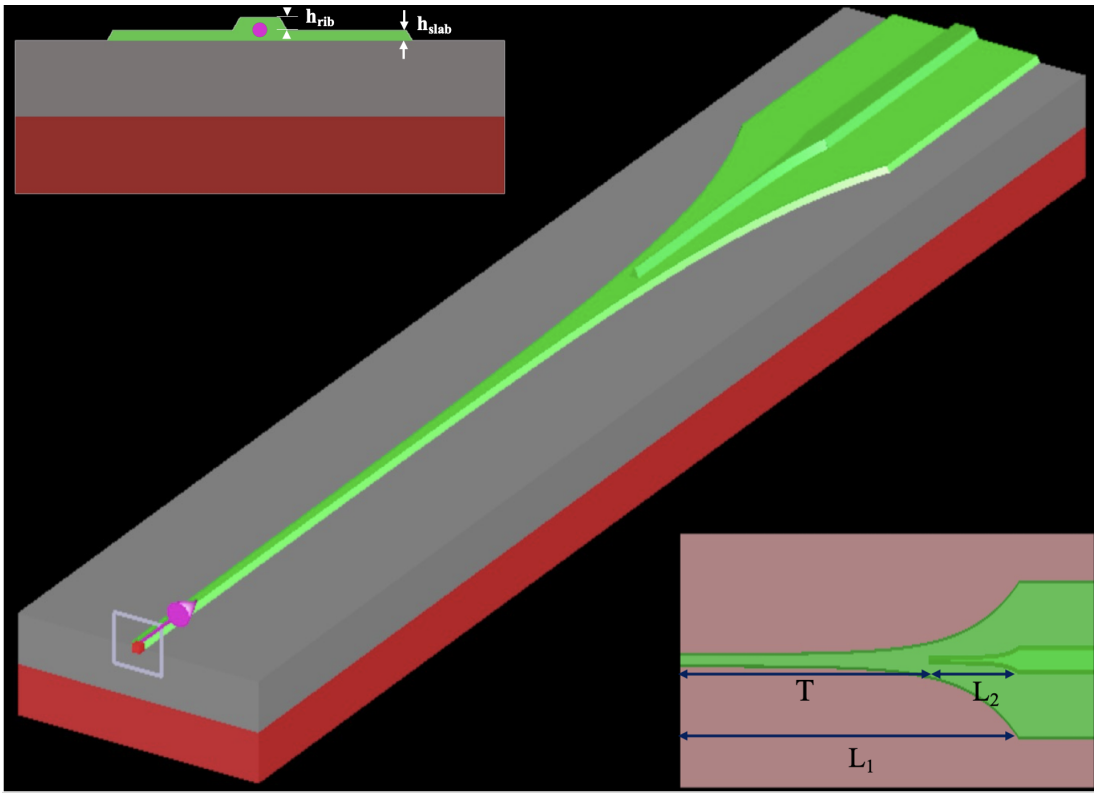

Figure 5.4: The inversely tapered bilayer edge coupler proposed in [158], simulated via Lumerical solution software. The parameters applied for this first implementation are those defined in the mentioned article. The purple circle at the end of back view of the waveguide—the top left figure—demonstrates the beam path through the rib-slab common region.

A schematic of the design simulated using Lumerical solution software is shown in Figure 5.4. It would be time consuming to consider all the factors that affect attenuation during coupling for a broad spectral range: to ensure speedy modelling, I based my design and optimization for the wavelength $1.55\mu m$. Figure 5.4 shows the simulated waveguide.

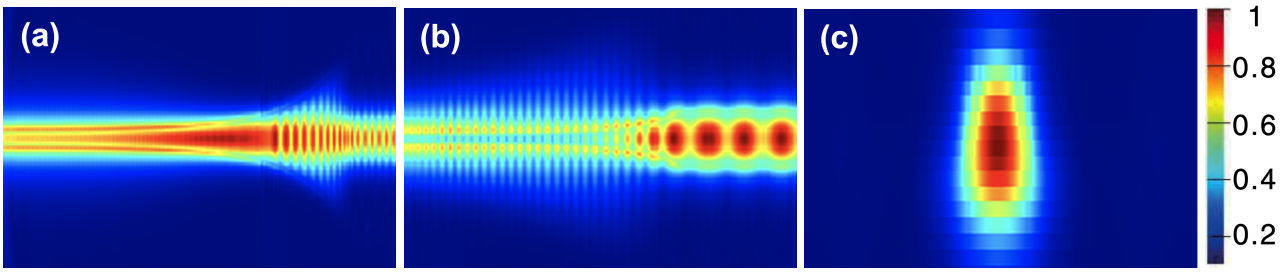

Figure 5.5: Propagation of the beam through (a) the slab waveguide, (b) the rib waveguide, as well as (c) the cross-section profile of the optical mode at the bilayer region, i.e. the rib-slab common region. Note that the length covered in (a) and (b) is the whole length of the edge coupler shown in Figure 5.4 including both tapered and straight parts of the waveguide. The monitor in figure (a) is placed at the middle of the slab waveguide, while in figure (b), the monitor is at the height center of the rib waveguide. Figure (c) also is the beam profile monitored at the end of the edge coupler structure; (see the top left of Figure 5.4).

Figure 5.5 demonstrates the propagation of the beam through the slab waveguide: Figure 5.5a) is for the slab waveguide, Figure (5.5b) for the rib waveguide, and Figure 5.5c) is the cross-section profile of the optical mode at the bilayer region. The total transmission of the TE field through the waveguide as a function of the wavelength is shown in Figure 5.6. At this step the parameters defined in [158] are applied. The transmission efficiency at the wavelength $1.55\mu m$ is about 79%.

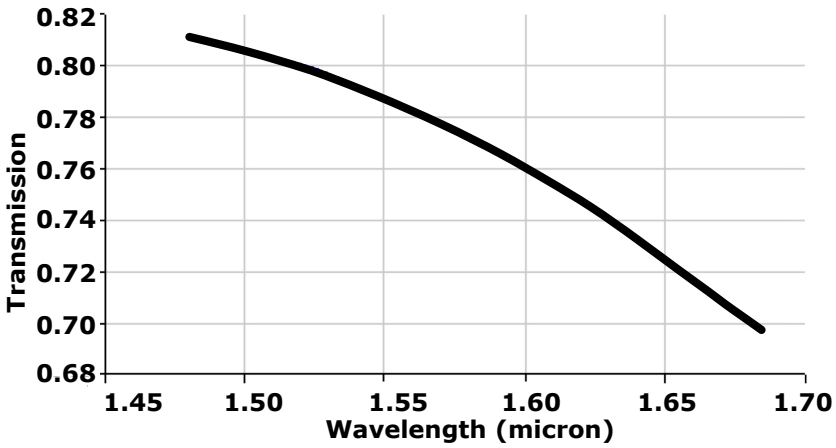

Figure 5.6: The total transmission of the simulated waveguide in Figure 5.4 as a function of the wavelength. In the spectral range $1.48\mu m$ to $1.68\mu m$ the transmission efficiency of the edge coupler is between 70 to 80%.

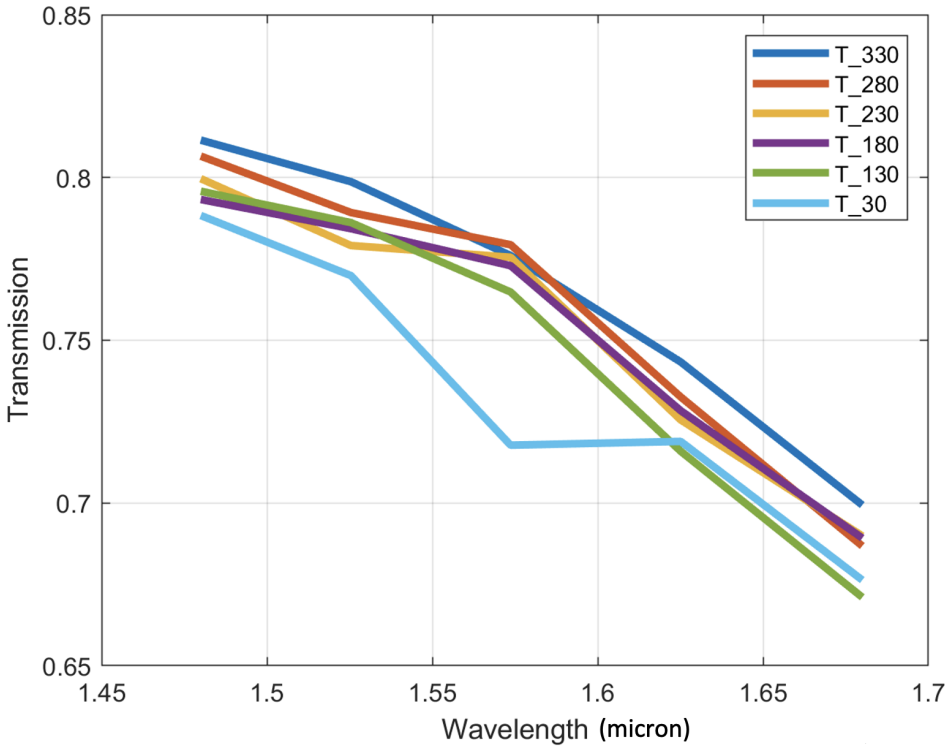

Figure 5.7: The transmission versus wavelength. The effect of varying distance between the edge of the circuit and the rib-slab junction, **T_x** (in micrometres).

To optimize the simulated structure, we investigated the performance of the edge coupler under variation of several design parameters including curvature coefficients and thicknesses of the rib and

slab waveguides, the distance of the light source from the edge of the circuit and the tapered length of the rib. The results are shown in Figures 5.7 to 5.11. The impact of varying the distance from edge of the circuit to the rib-slab junction, T—see Figure 5.4—was the first parameter we examined. This distance was suggested to be 330 μm in [158]. The length of the tapered rib waveguide, L_2, was kept constant during this test. As the graph in Figure 5.7 displays, the suggested distance—shown by the dark-blue curve—still has the best transmission.

In the next step, we assessed varying the light source position from the edge of the circuit. The variation has been chosen in the range from 0 to 2.5 μm. The graph in Figure 5.8 clearly suggests the least distance possible of the light source from the edge of the coupler, i.e. the dark blue curve. Note that the V-shape valleys appear to be an artifact of the simulation software: when we changed to higher level accuracy—which took more than eight times longer to run—the V-shapes moved to lower wavelengths but did not disappear. Further work will be needed to investigate how to remove these artifacts, which also feature in Figures 5.7 to 5.11.

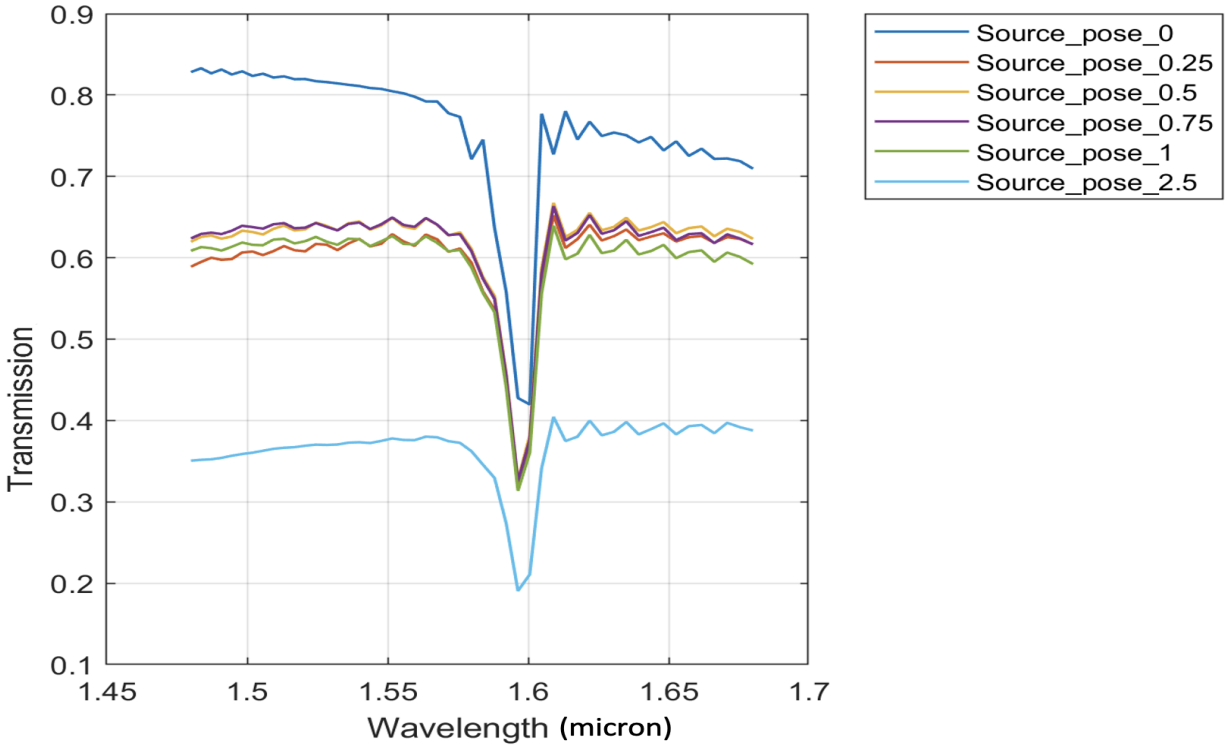

Figure 5.8: Variations of collective transmission from both the slab and rib cross-sections with different light source distances from the edge of the coupler. The length unit is in micrometer.

The thickness of the LN thin film utilized in the main paper was 600 μm which was divided to 250 μm the height of the slab waveguide, h_{slab} and 350 μm for the rib waveguide, h_{rib}. So we decided to examine the impact of different thickness ratios between the slab and the rib waveguide. The only conclusion from the results in Figure 5.9 is that for $h_{rib} > 350$ and $h_{slab} < 250$, the transmission of the coupler becomes worse, while for thicker slab and thinner rib waveguides, the efficiency is high and relatively unchanged. Of course, the best combination should be determined according to the optimal values for other parameters.

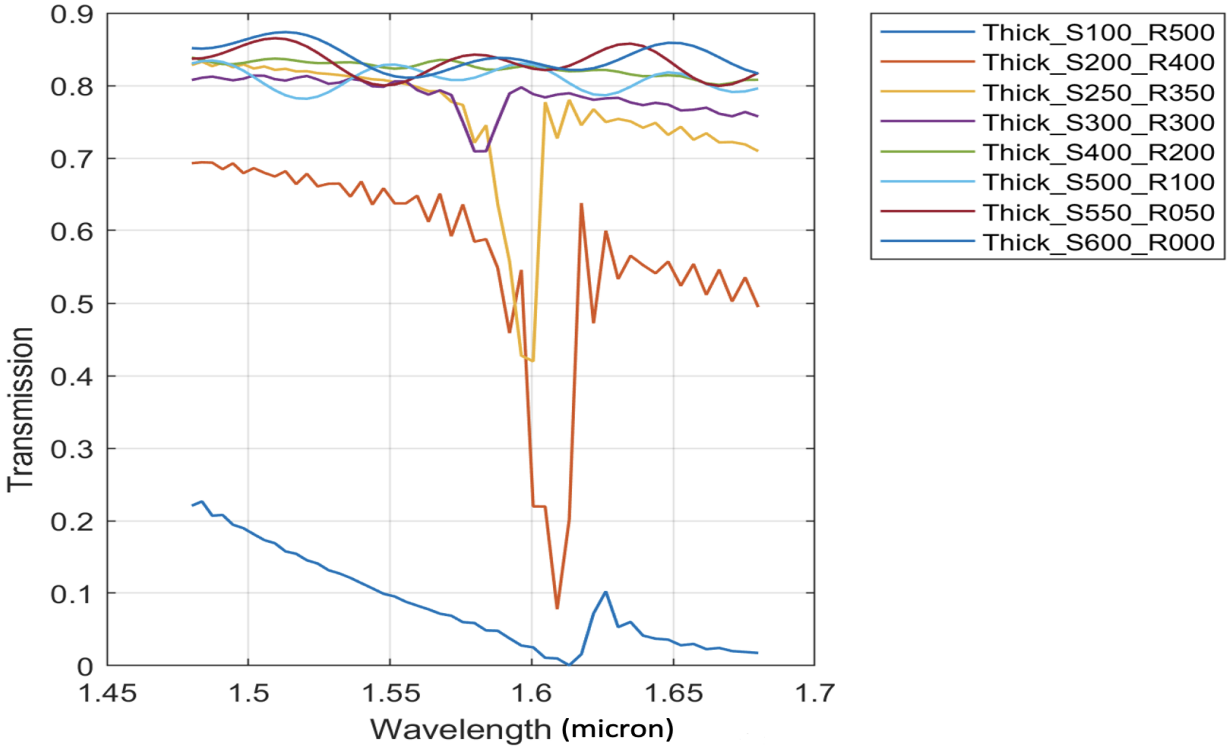

Figure 5.9: The effect of different ratios of the slab and rib waveguides thicknesses on the transmission efficiency. In the legends, *S* and *R* stand for the slab and rib waveguide thickness, respectively. The length unit is in micrometer.

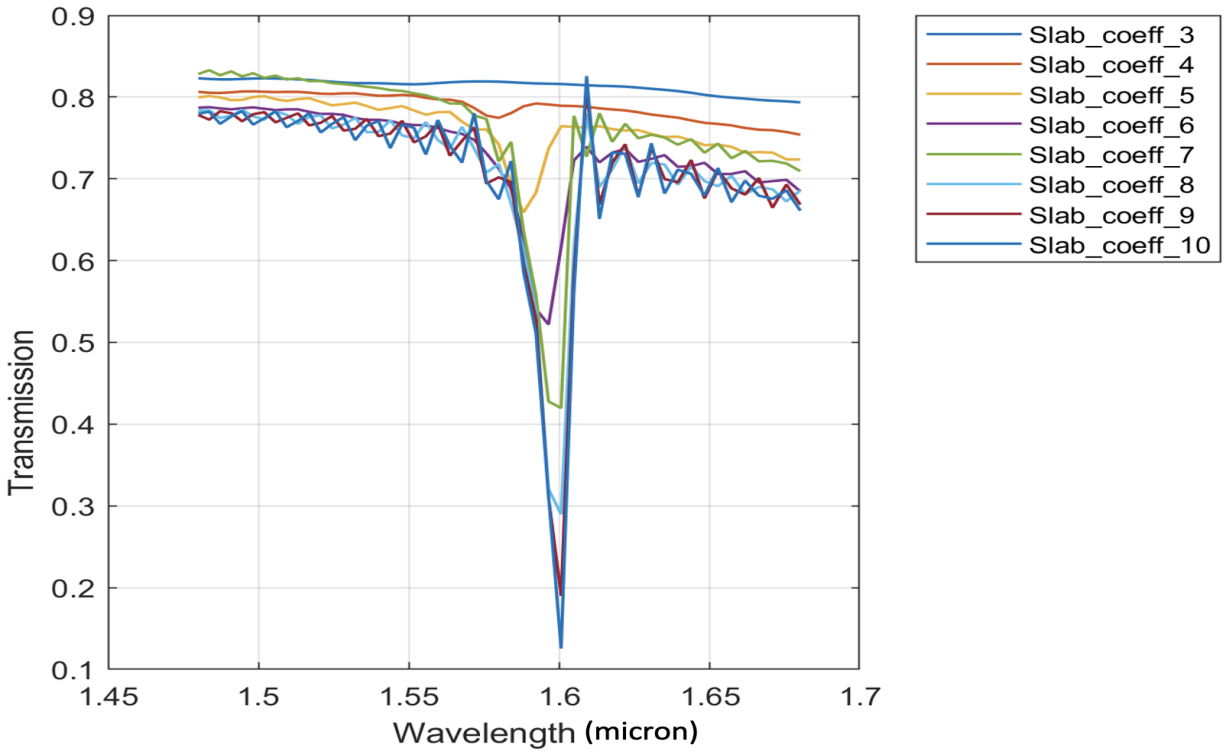

Figure 5.10: Changes in waveguide efficiency under the influence of changes in curvature coefficient of the slab layer.

We also have tested the effect of changing the curvature coefficients of the slab and the rib waveguides. Figures 5.10 and 5.11 show the results for these tests. The larger the coefficient, the more the curvature.

For the slab waveguide the smaller coefficients result in more transmission. Of course, for an optimized design, what matters is the collective efficiency of all parameters, but the graph can make us sure that for the current length of the slab waveguide, select its curvature coefficient in the range lower than 4. Interestingly, Figure 5.11 conveys that changing the rib tapered waveguide coefficient has no effect on the transmission of the waveguide. It is worth to test the truth of this argument with different lengths of the rib waveguide.

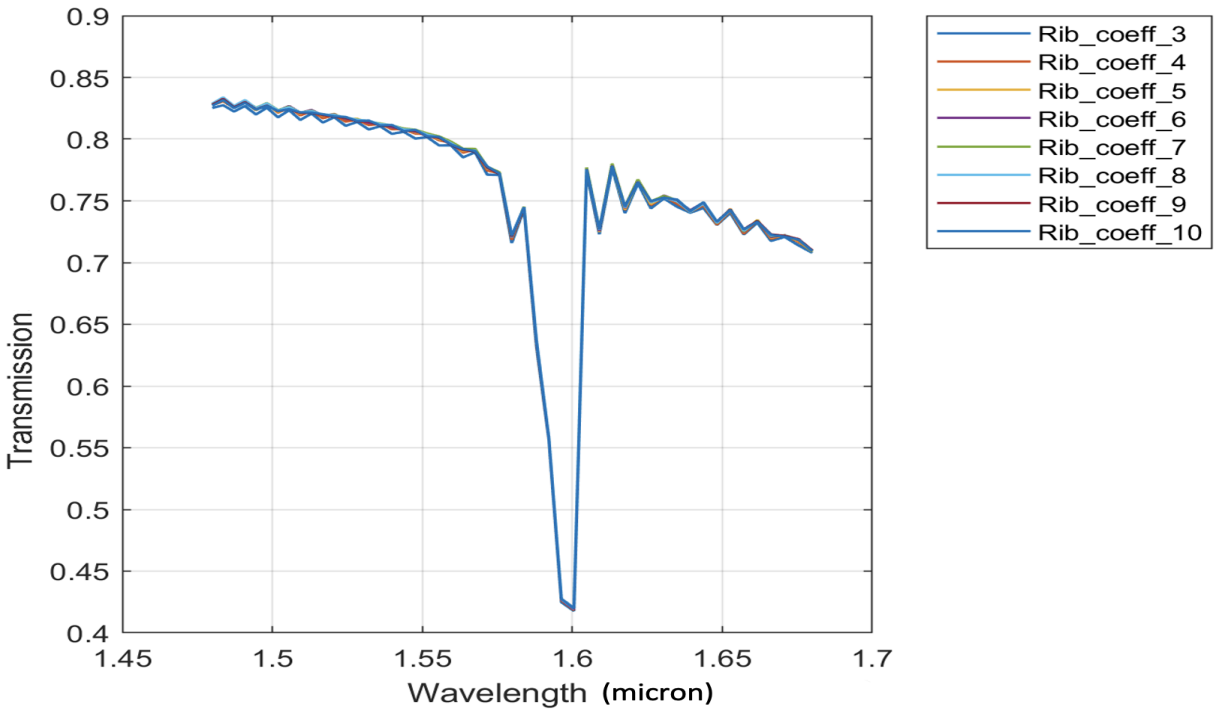

Figure 5.11: Changes in waveguide efficiency under the influence of changes in curvature coefficient of the rib layer.

In future work, remaining parameters to be investigated in order to achieve an optimum design could include wall angles, and widths and lengths of both waveguides. The optimal combination of parameters may be obvious, or may require computer-aided analysis. It is also not feasible to run all the simulations at the highest accuracy level as typically each curve for this structure—despite applying symmetry—takes $\sim$ 3 hours at the lowest accuracy level; the next level takes $\sim$ 24 hours (in Lumerical there are eight levels of accuracy overall). Altogether, micro-circuit design using lithium niobate is rather new field and the applicability of many ideas from silicon photonics may be considered to be examined in lithium niobate photonics and of course our project in the future investigations.

Chapter 6

Conclusion

In this research, we experimentally investigated the functionality of self-guided quantum tomography in high-dimensional state spaces of a photonic system and showed its superiority to the standard quantum tomography method. Self-guided tomography can be applied on any other quantum system and is especially the better candidate for those with high preparation fidelity but limited capability in providing high numbers of copies, such as trapped ions.

We tested self-guided tomography in three qudit spaces of 3, 5, and 20 dimensions under three different regimes: low statistical noise; high statistical noise; and low atmospheric turbulence. The results generally show a converging trend to lower infidelities, independent of any experimental or environmental imperfection or error in the system, see Figures 4.6 and 4.7. Thus we can achieve any desired accuracy in estimating the unknown state at the cost of more iterations. Based on these findings—that SGT is robust against the impact of different noise sources—self-guided tomography can be considered as the preferred method of quantum state estimation for many complex systems, unlike standard quantum tomography which is highly susceptible to imperfections in the system, e.g. mode-dependent losses in our case, see Figure 4.8. Although our experiments have been done with highly pure quantum states, this method is also applicable for mixed quantum states, by adding a post-processing step on the outcomes obtained after each iteration [162]. An open question is what degree of mixture or entropy finally suppresses the performance of this powerful algorithm either in accuracy or scaling? Apart from quantum state estimation, self-guided tomography has been used to characterize the quantum processes of qubits [163] which again is extendable to the processes in higher dimensions. The consistency of self-guided tomography with underlying physical architecture makes it applicable in dealing with any high dimensional quantum system, from a simple spin-half qubit to an array of entangled qudits.

In the second part of this thesis we addressed designing a high performance edge coupler to be used in a quantum circuit. We started with simulating a micro-design proposed by Loncar group in Harvard [158]. This design suggests a low-loss fiber to chip connection for lithium niobate photonic integrated circuits. What we are following is to extract a modified version for our quantum router which requires an optimal combination of parameters via computer-aided analysis.

Bibliography

[1] M. Rambach, M. Qaryan, M. Kewming, C. Ferrie, A. G. White, J. Romero, Robust and efficient high-dimensional quantum state tomography, Physical Review Letters 126 (10) (2021) 100402.

[2] R. J. Chapman, C. Ferrie, A. Peruzzo, Experimental demonstration of self-guided quantum tomography, Physical Review Letters 117 (4) (2016) 040402.

[3] H. Bechmann-Pasquinucci, W. Tittel, Quantum cryptography using larger alphabets, Physical Review A 61 (6) (2000) 062308.

[4] E. Otte, I. Nape, C. Rosales-Guzmán, C. Denz, A. Forbes, B. Ndagano, High-dimensional cryptography with spatial modes of light: Tutorial, JOSA B 37 (11) (2020) A309–A323.

[5] N. J. Cerf, M. Bourennane, A. Karlsson, N. Gisin, Security of quantum key distribution using d-level systems, Physical Review Letters 88 (12) (2002) 127902.

[6] L. Sheridan, V. Scarani, Erratum: Security proof for quantum key distribution using qudit systems [phys. rev. a 82, 030301 (r)(2010)], Physical Review A 83 (3) (2011) 039901.

[7] N. Gisin, S. Massar, Optimal quantum cloning machines, Physical Review Letters 79 (11) (1997) 2153.

[8] A. Siegman, Lasers (Universe Science Books), University Science Books, 1986.

[9] R. Menzel, Topics in photonics, in: Photonics, Springer, 2001, pp. 1–9.

[10] K. Shimoda, Introduction to laser physics, Vol. 44, Springer, 2013.

[11] M. A. Bandres, J. C. Gutiérrez-Vega, Ince–gaussian beams, Optics Letters 29 (2) (2004) 144–146.

[12] M. A. Porras, R. Borghi, M. Santarsiero, Relationship between elegant laguerre–gauss and bessel–gauss beams, JOSA A 18 (1) (2001) 177–184.

[13] R. B. Griffiths, Consistent quantum theory, Cambridge University Press, 2003.

[14] M. Mirhosseini, O. S. Magaña-Loaiza, M. N. O'Sullivan, B. Rodenburg, M. Malik, M. P. Lavery, M. J. Padgett, D. J. Gauthier, R. W. Boyd, High-dimensional quantum cryptography with twisted light, New Journal of Physics 17 (3) (2015) 033033.

[15] S. Walborn, D. Lemelle, M. Almeida, P. S. Ribeiro, Quantum key distribution with higher-order alphabets using spatially encoded qudits, Physical Review Letters 96 (9) (2006) 090501.

[16] Y. Zhang, F. S. Roux, T. Konrad, M. Agnew, J. Leach, A. Forbes, Engineering two-photon high-dimensional states through quantum interference, Science Advances 2 (2) (2016) e1501165.

[17] M. Krenn, M. Malik, M. Erhard, A. Zeilinger, Orbital angular momentum of photons and the entanglement of laguerre–gaussian modes, Philosophical Transactions of the Royal Society A: Mathematical, Physical and Engineering Sciences 375 (2087) (2017) 20150442.

[18] M. Erhard, R. Fickler, M. Krenn, A. Zeilinger, Twisted photons: new quantum perspectives in high dimensions, Light: Science & Applications 7 (3) (2018) 17146–17146.

[19] A. Sit, F. Bouchard, R. Fickler, J. Gagnon-Bischoff, H. Larocque, K. Heshami, D. Elser, C. Peuntinger, K. Günthner, B. Heim, et al., High-dimensional intracity quantum cryptography with structured photons, Optica 4 (9) (2017) 1006–1010.

[20] F. Bouchard, R. Fickler, R. W. Boyd, E. Karimi, High-dimensional quantum cloning and applications to quantum hacking, Science advances 3 (2) (2017) e1601915.

[21] M. A. Nielsen, I. Chuang, Quantum computation and quantum information (2002).

[22] L. C. Andrews, Laser beam propagation through random media, in: SPIE-International Society for Optical Engineering, 2005, pp. 84–132.

[23] J. W. Goodman, Introduction to Fourier Optics, McGraw-Hill, New York, 1968.

[24] I. B. Ndagano, Encoding information into spatial modes of light, Master's thesis, Physics (2016).

[25] A. Faßbender, J. Babockỳ, P. Dvořák, V. Křápek, S. Linden, Invited article: Direct phase mapping of broadband laguerre-gaussian metasurfaces, APL Photonics 3 (11) (2018) 110803.

[26] Q. Zhan, Cylindrical vector beams: from mathematical concepts to applications, Advances in Optics and Photonics 1 (1) (2009) 1–57.

[27] M. Brambilla, F. Battipede, L. Lugiato, V. Penna, F. Prati, C. Tamm, C. Weiss, Transverse laser patterns. i. phase singularity crystals, Physical Review A 43 (9) (1991) 5090.

[28] K. Yonezawa, Y. Kozawa, S. Sato, Generation of a radially polarized laser beam by use of the birefringence of a c-cut nd: Yvo4 crystal, Optics letters 31 (14) (2006) 2151–2153.

[29] J.-F. Bisson, J. Li, K. Ueda, Y. Senatsky, Radially polarized ring and arc beams of a neodymium laser with an intra-cavity axicon, Optics Express 14 (8) (2006) 3304–3311.

[30] M. R. Beversluis, L. Novotny, S. J. Stranick, Programmable vector point-spread function engineering, Optics express 14 (7) (2006) 2650–2656.

[31] S. Trester, Computer simulated holography and computer generated holograms, American Journal of Physics 64 (4) (1996) 472–478.

[32] A. G. Porter, S. George, An elementary introduction to practical holography, American Journal of Physics 43 (11) (1975) 954–959.

[33] J. S. Marsh, R. C. Smith, Computer holograms with a desk-top calculator, American Journal of Physics 44 (8) (1976) 774–777.

[34] N. Heckenberg, R. McDuff, C. Smith, A. White, Generation of optical phase singularities by computer-generated holograms, Optics letters 17 (3) (1992) 221–223.

[35] P. Coullet, L. Gil, F. Rocca, Optical vortices, Optics Communications 73 (5) (1989) 403–408.

[36] Q. Zhan, J. R. Leger, Interferometric measurement of the geometric phase in space-variant polarization manipulations, Optics communications 213 (4-6) (2002) 241–245.

[37] G. Machavariani, Y. Lumer, I. Moshe, A. Meir, S. Jackel, Spatially-variable retardation plate for efficient generation of radially-and azimuthally-polarized beams, Optics Communications 281 (4) (2008) 732–738.

[38] R. Zheng, C. Gu, A. Wang, L. Xu, H. Ming, An all-fiber laser generating cylindrical vector beam, Optics express 18 (10) (2010) 10834–10838.

[39] B. Rodenburg, Communicating with transverse modes of light, University of Rochester, 2015.

[40] B. R. Brown, A. W. Lohmann, Complex spatial filtering with binary masks, Applied optics 5 (6) (1966) 967–969.

[41] E. G. Loewen, Diffraction gratings, ruled and holographic, Applied Optics and Optical Engineering 9 (2012) 33–71.

[42] J. E. Harvey, R. N. Pfisterer, Understanding diffraction grating behavior: including conical diffraction and rayleigh anomalies from transmission gratings, Optical Engineering 58 (8) (2019) 087105.

[43] A. Mair, A. Vaziri, G. Weihs, A. Zeilinger, Entanglement of the orbital angular momentum states of photons, Nature 412 (6844) (2001) 313–316.

[44] R. W. Boyd, A. Jha, M. Malik, C. O'Sullivan, B. Rodenburg, D. J. Gauthier, Quantum key distribution in a high-dimensional state space: exploiting the transverse degree of freedom of the photon, in: Advances in Photonics of Quantum Computing, Memory, and Communication IV, Vol. 7948, International Society for Optics and Photonics, 2011, p. 79480L.

[45] S. Etcheverry, G. Cañas, E. Gómez, W. Nogueira, C. Saavedra, G. Xavier, G. Lima, Quantum key distribution session with 16-dimensional photonic states, Scientific reports 3 (1) (2013) 1–5.

[46] A. Kolmogorov, Local structure of turbulence in incompressible fluid under very high values of reynolds numbers, Reports of AS USSR 30 (4) (1941) 299–303.

[47] V. Tatarski, Wave propagation in a turbulent medium mc graw hill book comp, New York (1961).

[48] D. Fried, Statistics of a geometrical representation of a deformed wavefront, Journal of the Optical Society of America 55 (1965) 1427.

[49] D. Fried, Diffusion analysis for the propagation of mutual coherence, JOSA 58 (7) (1968) 961–969.

[50] G. I. Struchalin, I. A. Pogorelov, S. S. Straupe, K. S. Kravtsov, I. V. Radchenko, S. P. Kulik, Experimental adaptive quantum tomography of two-qubit states, Physical Review A 93 (1) (2016) 012103.

[51] B. Qi, Z. Hou, Y. Wang, D. Dong, H.-S. Zhong, L. Li, G.-Y. Xiang, H. M. Wiseman, C.-F. Li, G.-C. Guo, Adaptive quantum state tomography via linear regression estimation: Theory and two-qubit experiment, NPJ Quantum Information 3 (1) (2017) 1–7.

[52] J. B. Altepeter, D. F. James, P. G. Kwiat, 4 qubit quantum state tomography, in: Quantum State Estimation, Springer, 2004, pp. 113–145.

[53] R. A. Beth, Mechanical detection and measurement of the angular momentum of light, Physical Review 50 (2) (1936) 115.

[54] E. Toninelli, B. Ndagano, A. Vallés, B. Sephton, I. Nape, A. Ambrosio, F. Capasso, M. J. Padgett, A. Forbes, Concepts in quantum state tomography and classical implementation with intense light: a tutorial, Advances in Optics and Photonics 11 (1) (2019) 67–134.

[55] M. Paris, J. Rehacek, Quantum state estimation, Vol. 649, Springer Science & Business Media, 2004.

[56] A. Forbes, A. Dudley, M. McLaren, Creation and detection of optical modes with spatial light modulators, Advances in Optics and Photonics 8 (2) (2016) 200–227.

[57] M. J. Padgett, J. Courtial, Poincaré-sphere equivalent for light beams containing orbital angular momentum, Optics letters 24 (7) (1999) 430–432.

[58] L. Allen, M. W. Beijersbergen, R. Spreeuw, J. Woerdman, Orbital angular momentum of light and the transformation of laguerre-gaussian laser modes, Physical review A 45 (11) (1992) 8185.

[59] A. G. White, D. F. James, P. H. Eberhard, P. G. Kwiat, Nonmaximally entangled states: production, characterization, and utilization, Physical Review Letters 83 (16) (1999) 3103.

[60] R. Thew, K. Nemoto, A. G. White, W. J. Munro, Qudit quantum-state tomography, Physical Review A 66 (1) (2002) 012303.

[61] D. F. James, P. G. Kwiat, W. J. Munro, A. G. White, On the measurement of qubits, in: Asymptotic Theory of Quantum Statistical Inference: Selected Papers, World Scientific, 2005, pp. 509–538.

[62] R. Schmied, Quantum state tomography of a single qubit: comparison of methods, Journal of Modern Optics 63 (18) (2016) 1744–1758.

[63] S. Luo, Using measurement-induced disturbance to characterize correlations as classical or quantum, Physical Review A 77 (2) (2008) 022301.

[64] G. M. D'Ariano, H. Yuen, Impossibility of measuring the wave function of a single quantum system, Physical Review Letters 76 (16) (1996) 2832.

[65] W. K. Wootters, W. H. Zurek, A single quantum cannot be cloned, Nature 299 (5886) (1982) 802–803.

[66] N. Brunner, S. Pironio, A. Acin, N. Gisin, A. A. Méthot, V. Scarani, Testing the dimension of hilbert spaces, Physical Review Letters 100 (21) (2008) 210503.

[67] M. Hendrych, R. Gallego, M. Mičuda, N. Brunner, A. Acín, J. P. Torres, Experimental estimation of the dimension of classical and quantum systems, Nature Physics 8 (8) (2012) 588–591.

[68] J. Ahrens, P. Badziag, A. Cabello, M. Bourennane, Experimental device-independent tests of classical and quantum dimensions, Nature Physics 8 (8) (2012) 592–595.

[69] L. M. Johansen, Quantum theory of successive projective measurements, Physical Review A 76 (1) (2007) 012119.

[70] G. M. D'Ariano, M. G. Paris, M. F. Sacchi, Quantum tomography, Advances in Imaging and Electron Physics 128 (2003) 206–309.

[71] U. Fano, Description of states in quantum mechanics by density matrix and operator techniques, Reviews of modern physics 29 (1) (1957) 74.

[72] L. P. Hughston, R. Jozsa, W. K. Wootters, A complete classification of quantum ensembles having a given density matrix, Physics Letters A 183 (1) (1993) 14–18.

[73] K. Banaszek, G. D'ariano, M. Paris, M. Sacchi, Maximum-likelihood estimation of the density matrix, Physical Review A 61 (1) (1999) 010304.

[74] S. R. White, Density matrix formulation for quantum renormalization groups, Physical Review Letters 69 (19) (1992) 2863.

[75] M. Agnew, J. Leach, M. McLaren, F. S. Roux, R. W. Boyd, Tomography of the quantum state of photons entangled in high dimensions, Physical Review A 84 (6) (2011) 062101.

[76] K. Banaszek, M. Cramer, D. Gross, Focus on quantum tomography, New Journal of Physics 15 (12) (2013) 125020.

[77] C. H. Bennett, G. Brassard, S. Popescu, B. Schumacher, J. A. Smolin, W. K. Wootters, Purification of noisy entanglement and faithful teleportation via noisy channels, Physical Review Letters 76 (5) (1996) 722.

[78] E. Knill, R. Laflamme, L. Viola, Theory of quantum error correction for general noise, Physical Review Letters 84 (11) (2000) 2525.

[79] P. Samuelsson, M. Büttiker, Quantum state tomography with quantum shot noise, Physical Review B 73 (4) (2006) 041305.

[80] T. Monz, P. Schindler, J. T. Barreiro, M. Chwalla, D. Nigg, W. A. Coish, M. Harlander, W. Hänsel, M. Hennrich, R. Blatt, 14-qubit entanglement: Creation and coherence, Physical Review Letters 106 (13) (2011) 130506.

[81] P. G. Kwiat, K. Mattle, H. Weinfurter, A. Zeilinger, A. V. Sergienko, Y. Shih, New high-intensity source of polarization-entangled photon pairs, Physical Review Letters 75 (24) (1995) 4337.

[82] M. D. De Burgh, N. K. Langford, A. C. Doherty, A. Gilchrist, Choice of measurement sets in qubit tomography, Physical Review A 78 (5) (2008) 052122.

[83] H. Zhu, Quantum state estimation with informationally overcomplete measurements, Physical Review A 90 (1) (2014) 012115.

[84] J. B. Altepeter, E. R. Jeffrey, P. G. Kwiat, Photonic state tomography, Advances in Atomic, Molecular, and Optical Physics 52 (2005) 105–159.

[85] D. J. Lum, S. H. Knarr, J. C. Howell, Fast hadamard transforms for compressive sensing of joint systems: measurement of a 3.2 million-dimensional bi-photon probability distribution, Optics Express 23 (21) (2015) 27636–27649.

[86] S. S. Straupe, Adaptive quantum tomography, JETP Letters 104 (7) (2016) 510–522.

[87] H. Sosa-Martinez, N. Lysne, C. Baldwin, A. Kalev, I. Deutsch, P. Jessen, Experimental study of optimal measurements for quantum state tomography, Physical Review Letters 119 (15) (2017) 150401.

[88] J. Bavaresco, N. H. Valencia, C. Klöckl, M. Pivoluska, P. Erker, N. Friis, M. Malik, M. Huber, Measurements in two bases are sufficient for certifying high-dimensional entanglement, Nature Physics 14 (10) (2018) 1032–1037.

[89] M. Cramer, M. B. Plenio, S. T. Flammia, R. Somma, D. Gross, S. D. Bartlett, O. Landon-Cardinal, D. Poulin, Y.-K. Liu, Efficient quantum state tomography, Nature Communications 1 (1) (2010) 1–7.

[90] G. Tóth, W. Wieczorek, D. Gross, R. Krischek, C. Schwemmer, H. Weinfurter, Permutationally invariant quantum tomography, Physical Review Letters 105 (25) (2010) 250403.

[91] J. G. Titchener, M. Gräfe, R. Heilmann, A. S. Solntsev, A. Szameit, A. A. Sukhorukov, Scalable on-chip quantum state tomography, NPJ Quantum Information 4 (1) (2018) 1–6.

[92] K. Wang, J. G. Titchener, S. S. Kruk, L. Xu, H. P. Chung, M. Parry, I. I. Kravchenko, Y. H. Chen, A. S. Solntsev, Y. S. Kivshar, et al., Quantum metasurface for multiphoton interference and state reconstruction, Science 361 (6407) (2018) 1104–1108.

[93] L. Banchi, W. S. Kolthammer, M. Kim, Multiphoton tomography with linear optics and photon counting, Physical Review Letters 121 (25) (2018) 250402.

[94] K. Vogel, H. Risken, Determination of quasiprobability distributions in terms of probability distributions for the rotated quadrature phase, Physical Review A 40 (5) (1989) 2847.

[95] D. Smithey, M. Beck, M. G. Raymer, A. Faridani, Measurement of the wigner distribution and the density matrix of a light mode using optical homodyne tomography: Application to squeezed states and the vacuum, Physical Review Letters 70 (9) (1993) 1244.

[96] G. d'Ariano, C. Macchiavello, M. Paris, Detection of the density matrix through optical homodyne tomography without filtered back projection, Physical Review A 50 (5) (1994) 4298.

[97] G. D'ariano, U. Leonhardt, H. Paul, Homodyne detection of the density matrix of the radiation field, Physical Review A 52 (3) (1995) R1801.

[98] M. Munroe, D. Boggavarapu, M. Anderson, M. Raymer, Photon-number statistics from the phase-averaged quadrature-field distribution: Theory and ultrafast measurement, Physical Review A 52 (2) (1995) R924.

[99] S. Schiller, G. Breitenbach, S. Pereira, T. Müller, J. Mlynek, Quantum statistics of the squeezed vacuum by measurement of the density matrix in the number state representation, Physical Review Letters 77 (14) (1996) 2933.

[100] F. Mallet, M. Castellanos-Beltran, H. Ku, S. Glancy, E. Knill, K. Irwin, G. Hilton, L. Vale, K. Lehnert, Quantum state tomography of an itinerant squeezed microwave field, Physical Review Letters 106 (22) (2011) 220502.

[101] M. Crispino, G. Di Giuseppe, F. De Martini, P. Mataloni, H. Kanatsoulis, Towards a fock-states tomographic reconstruction, Fortschritte der Physik: Progress of Physics 48 (5-7) (2000) 589–598.

[102] A. Lvovsky, M. Raymer, Continuous-variable quantum-state tomography of optical fields and photons, in: Quantum Information with Continuous Variables of Atoms and Light, World Scientific, 2007, pp. 409–433.

[103] D. Gross, Y.-K. Liu, S. T. Flammia, S. Becker, J. Eisert, Quantum state tomography via compressed sensing, Physical Review Letters 105 (15) (2010) 150401.

[104] M. Ghalaii, M. Afsary, S. Alipour, A. Rezakhani, Quantum imaging as an ancilla-assisted process tomography, Physical Review A 94 (4) (2016) 042102.

[105] K. J. Resch, P. Walther, A. Zeilinger, Full characterization of a three-photon greenberger-horne-zeilinger state using quantum state tomography, Physical Review Letters 94 (7) (2005) 070402.

[106] V. Man'ko, O. Man'ko, Spin state tomography, Journal of Experimental and Theoretical Physics 85 (3) (1997) 430–434.

[107] R. S. Cohen, M. Horne, J. Stachel, Experimental metaphysics ˙ quantum mechanical studies for abner shimony. volume one, Boston Studies in the Philosophy of Science 193 (1997).

[108] T. Dunn, I. Walmsley, S. Mukamel, Experimental determination of the quantum-mechanical state of a molecular vibrational mode using fluorescence tomography, Physical Review Letters 74 (6) (1995) 884.

[109] C. Kurtsiefer, T. Pfau, J. Mlynek, Measurement of the wigner function of an ensemble of helium atoms, Nature 386 (6621) (1997) 150–153.

[110] D. Leibfried, D. Meekhof, B. King, C. Monroe, W. M. Itano, D. J. Wineland, Experimental determination of the motional quantum state of a trapped atom, Physical Review Letters 77 (21) (1996) 4281.

[111] A. Aspect, P. Grangier, G. Roger, Experimental tests of realistic local theories via bell's theorem, Physical Review Letters 47 (7) (1981) 460.

[112] A. Aspect, J. Dalibard, G. Roger, Experimental test of bell's inequalities using time-varying analyzers, Physical Review Letters 49 (25) (1982) 1804.

[113] D. Bouwmeester, J.-W. Pan, K. Mattle, M. Eibl, H. Weinfurter, A. Zeilinger, Experimental quantum teleportation, Nature 390 (6660) (1997) 575–579.

[114] P. G. Kwiat, E. Waks, A. G. White, I. Appelbaum, P. H. Eberhard, Ultrabright source of polarization-entangled photons, Physical Review A 60 (2) (1999) R773.

[115] J. L. O'Brien, G. J. Pryde, A. G. White, T. C. Ralph, D. Branning, Demonstration of an all-optical quantum controlled-not gate, Nature 426 (6964) (2003) 264–267.

[116] A. Chefles, 12 quantum states: discrimination and classical information transmission. a review of experimental progress, Quantum State Estimation (2004) 467–511.

[117] Ö. Bayraktar, M. Swillo, C. Canalias, G. Björk, Quantum-polarization state tomography, Physical Review A 94 (2) (2016) 020105.

[118] M. McLaren, M. Agnew, J. Leach, F. S. Roux, M. J. Padgett, R. W. Boyd, A. Forbes, Entangled bessel-gaussian beams, Optics Express 20 (21) (2012) 23589–23597.

[119] M. Krenn, R. Fickler, M. Huber, R. Lapkiewicz, W. Plick, S. Ramelow, A. Zeilinger, Entangled singularity patterns of photons in ince-gauss modes, Physical Review A 87 (1) (2013) 012326.

[120] E. Karimi, R. Boyd, P. De La Hoz, H. De Guise, J. Řeháček, Z. Hradil, A. Aiello, G. Leuchs, L. L. Sánchez-Soto, Radial quantum number of laguerre-gauss modes, Physical Review A 89 (6) (2014) 063813.

[121] V. Salakhutdinov, E. Eliel, W. Löffler, Full-field quantum correlations of spatially entangled photons, Physical Review Letters 108 (17) (2012) 173604.

[122] Y. Zhang, S. Prabhakar, C. Rosales-Guzmán, F. S. Roux, E. Karimi, A. Forbes, Hong-ou-mandel interference of entangled hermite-gauss modes, Physical Review A 94 (3) (2016) 033855.

[123] S. Gröblacher, T. Jennewein, A. Vaziri, G. Weihs, A. Zeilinger, Experimental quantum cryptography with qutrits, New Journal of Physics 8 (5) (2006) 75.

[124] M. Mafu, A. Dudley, S. Goyal, D. Giovannini, M. McLaren, M. J. Padgett, T. Konrad, F. Petruccione, N. Lütkenhaus, A. Forbes, Higher-dimensional orbital-angular-momentum-based quantum key distribution with mutually unbiased bases, Physical Review A 88 (3) (2013) 032305.

[125] D. Collins, N. Gisin, N. Linden, S. Massar, S. Popescu, Bell inequalities for arbitrarily high-dimensional systems, Physical Review Letters 88 (4) (2002) 040404.

[126] A. C. Dada, J. Leach, G. S. Buller, M. J. Padgett, E. Andersson, Experimental high-dimensional two-photon entanglement and violations of generalized bell inequalities, Nature Physics 7 (9) (2011) 677–680.

[127] Y. Zhang, M. Agnew, T. Roger, F. S. Roux, T. Konrad, D. Faccio, J. Leach, A. Forbes, Simultaneous entanglement swapping of multiple orbital angular momentum states of light, Nature Communications 8 (1) (2017) 1–7.

[128] E. T. Campbell, H. Anwar, D. E. Browne, Magic-state distillation in all prime dimensions using quantum reed-muller codes, Physical Review X 2 (4) (2012) 041021.

[129] B. P. Lanyon, M. Barbieri, M. P. Almeida, T. Jennewein, T. C. Ralph, K. J. Resch, G. J. Pryde, J. L. O'brien, A. Gilchrist, A. G. White, Simplifying quantum logic using higher-dimensional hilbert spaces, Nature Physics 5 (2) (2009) 134–140.

[130] M. Kewming, S. Shrapnel, A. White, J. Romero, Hiding ignorance using high dimensions, Physical Review Letters 124 (25) (2020) 250401.

[131] C. Ferrie, Self-guided quantum tomography, Physical Review Letters 113 (19) (2014) 190404.

[132] G. M. D'Ariano, M. G. Paris, Adaptive quantum homodyne tomography, Physical Review A 60 (1) (1999) 518.

[133] D. G. Fischer, S. H. Kienle, M. Freyberger, Quantum-state estimation by self-learning measurements, Physical Review A 61 (3) (2000) 032306.

[134] F. Huszár, N. M. Houlsby, Adaptive bayesian quantum tomography, Physical Review A 85 (5) (2012) 052120.

[135] T. Hannemann, D. Reiss, C. Balzer, W. Neuhauser, P. Toschek, C. Wunderlich, Self-learning estimation of quantum states, Physical Review A 65 (5) (2002) 050303.

[136] D. H. Mahler, L. A. Rozema, A. Darabi, C. Ferrie, R. Blume-Kohout, A. Steinberg, Adaptive quantum state tomography improves accuracy quadratically, Physical Review Letters 111 (18) (2013) 183601.

[137] K. S. Kravtsov, S. S. Straupe, I. V. Radchenko, N. M. Houlsby, F. Huszár, S. P. Kulik, Experimental adaptive bayesian tomography, Physical Review A 87 (6) (2013) 062122.

[138] J. C. Spall, et al., Multivariate stochastic approximation using a simultaneous perturbation gradient approximation, IEEE Transactions on Automatic Control 37 (3) (1992) 332–341.

[139] D. C. Burnham, D. L. Weinberg, Observation of simultaneity in parametric production of optical photon pairs, Physical Review Letters 25 (2) (1970) 84.

[140] C. Paterson, Atmospheric turbulence and orbital angular momentum of single photons for optical communication, Physical Review Letters 94 (15) (2005) 153901.

[141] G. A. Tyler, R. W. Boyd, Influence of atmospheric turbulence on the propagation of quantum states of light carrying orbital angular momentum, Optics Letters 34 (2) (2009) 142–144.

[142] M. Malik, M. O'Sullivan, B. Rodenburg, M. Mirhosseini, J. Leach, M. P. Lavery, M. J. Padgett, R. W. Boyd, Influence of atmospheric turbulence on optical communications using orbital angular momentum for encoding, Optics Express 20 (12) (2012) 13195–13200.

[143] M. Krenn, R. Fickler, M. Fink, J. Handsteiner, M. Malik, T. Scheidl, R. Ursin, A. Zeilinger, Communication with spatially modulated light through turbulent air across vienna, New Journal of Physics 16 (11) (2014) 113028.

[144] Y. I. Bogdanov, Unified statistical method for reconstructing quantum states by purification, Journal of Experimental and Theoretical Physics 108 (6) (2009) 928–935.

[145] D. Giovannini, J. Romero, J. Leach, A. Dudley, A. Forbes, M. J. Padgett, Characterization of high-dimensional entangled systems via mutually unbiased measurements, Physical Review Letters 110 (14) (2013) 143601.

[146] N. K. Langford, R. B. Dalton, M. D. Harvey, J. L. O'Brien, G. J. Pryde, A. Gilchrist, S. D. Bartlett, A. G. White, Measuring entangled qutrits and their use for quantum bit commitment, Physical Review Letters 93 (5) (2004) 053601.

[147] S. Wehner, D. Elkouss, R. Hanson, Quantum internet: A vision for the road ahead, Science 362 (6412) (2018).

[148] M. Zhang, C. Wang, R. Cheng, A. Shams-Ansari, M. Lončar, Monolithic ultra-high-q lithium niobate microring resonator, Optica 4 (12) (2017) 1536–1537.

[149] L. Chang, Y. Li, N. Volet, L. Wang, J. Peters, J. E. Bowers, Thin film wavelength converters for photonic integrated circuits, Optica 3 (5) (2016) 531–535.

[150] I. Krasnokutska, J.-L. J. Tambasco, X. Li, A. Peruzzo, Ultra-low loss photonic circuits in lithium niobate on insulator, Optics Express 26 (2) (2018) 897–904.

[151] L. Cai, A. Mahmoud, G. Piazza, Low-loss waveguides on y-cut thin film lithium niobate: towards acousto-optic applications, Optics Express 27 (7) (2019) 9794–9802.

[152] P. P. Rohde, Simple scheme for universal linear-optics quantum computing with constant experimental complexity using fiber loops, Physical Review A 91 (1) (2015) 012306.

[153] M. Reck, A. Zeilinger, H. J. Bernstein, P. Bertani, Experimental realization of any discrete unitary operator, Physical Review Letters 73 (1) (1994) 58.

[154] V. R. Almeida, R. R. Panepucci, M. Lipson, Nanotaper for compact mode conversion, Optics Letters 28 (15) (2003) 1302–1304.

[155] B. B. Bakir, A. V. de Gyves, R. Orobtchouk, P. Lyan, C. Porzier, A. Roman, J.-M. Fedeli, Low-loss ($<$1 db) and polarization-insensitive edge fiber couplers fabricated on 200-mm silicon-on-insulator wafers, IEEE Photonics Technology Letters 22 (11) (2010) 739–741.

[156] M. Pu, L. Liu, H. Ou, K. Yvind, J. M. Hvam, Ultra-low-loss inverted taper coupler for silicon-on-insulator ridge waveguide, Optics Communications 283 (19) (2010) 3678–3682.

[157] J. Wang, Y. Xuan, C. Lee, B. Niu, L. Liu, G. N. Liu, M. Qi, Low-loss and misalignment-tolerant fiber-to-chip edge coupler based on double-tip inverse tapers, in: Optical Fiber Communication Conference, Optical Society of America, 2016, pp. M2I–6.

[158] L. He, M. Zhang, A. Shams-Ansari, R. Zhu, C. Wang, L. Marko, Low-loss fiber-to-chip interface for lithium niobate photonic integrated circuits, Optics Letters 44 (9) (2019) 2314–2317.

[159] N. Fang, Z. Yang, A. Wu, J. Chen, M. Zhang, S. Zou, X. Wang, Three-dimensional tapered spot-size converter based on (111) silicon-on-insulator, IEEE Photonics Technology Letters 21 (12) (2009) 820–822.

[160] A. J. Mercante, P. Yao, S. Shi, G. Schneider, J. Murakowski, D. W. Prather, 110 ghz cmos compatible thin film linbo3 modulator on silicon, Optics Express 24 (14) (2016) 15590–15595.

[161] C. Wang, M. Zhang, B. Stern, M. Lipson, M. Lončar, Nanophotonic lithium niobate electro-optic modulators, Optics Express 26 (2) (2018) 1547–1555.

[162] C. Granade, C. Ferrie, S. T. Flammia, Practical adaptive quantum tomography, New Journal of Physics 19 (11) (2017) 113017.

[163] Z. Hou, J.-F. Tang, C. Ferrie, G.-Y. Xiang, C.-F. Li, G.-C. Guo, Experimental realization of self-guided quantum process tomography, Physical Review A 101 (2) (2020) 022317.

Appendix A

Appendix

A.1 Python Code to Produce Holograms and Aligning the SLMs

The procedure of aligning the SLMs for tomography measurements is a time consuming process that requires high levels of accuracy. Here we present a code that is able to center the encoding and measurement SLMs in a reasonable time and with considerable accuracy. At the start, the algorithm prepares gaussian mode, TEM_{00}, on the measurement SLM and a higher order Laguerre Gaussian Vortex mode, LGV_{0i}—doughnut mode, where i is the azimuthal mode index—on the eSLM—see part 2. Then it produces the holograms corresponding to these quantum states on the SLMs screen—see part3. Now by keeping the Gaussian mode on the measurement SLM still and translating the doughnut mode on the eSLM horizontally, it registers the overlapping map of the two quantum states. According to the results, it substitutes a new set of coordinates for the moving hologram. This becomes repeated until a sharp V shape Valley appears out of this step—see part 4. Then at the next step, the doughnut mode will be replaced by Gaussian mode the same as the quantum state and its corresponding hologram on the measurement SLM. This time in the vertical direction, the overlap of both modes becomes registered—see part (5.1). The result is a bell curve shape. Again the coordinates become replaced with more accurate ones. Now algorithm changes the order. It translates the hologram of the Gaussian mode on the mSLM—that was constant up to this step—over the hologram of the encoding SLM—see part (5.2). Through analyzing the data obtained from the bell shape curves, the alignment optimization continues. Repeating this process results in more and more accurate coordinates. With the new coordinates, both SLMs centers will be well aligned.

0.1 Start by loading all required packages

[1]:
```
# General packages for scientific programming
import numpy as np
from scipy.special import eval_genlaguerre
from scipy.misc import factorial
import matplotlib.pyplot as plt
from scipy.optimize import curve_fit

# Import functions and objects for slm_essentials and encoding (included in bin)
from bin.slm_essentials import *
from bin.encoding import *
```

0.2 General SLM parameters

[2]:
```
pxl_x, pxl_y = 1200,1200

x_dim, y_dim = 12, 12                    # x,y dimensions of SLM in mm

ratio = pxl_x/x_dim
pxl_s = 1/ratio

wavelength = (820e-9)*1e3                # Wavelength in mm
```

1 Hologram Parameters

[3]:
```
################## --------- Encoding Hologram e parameters ------ ##############

x0_e, y0_e = 0, 0                       # Center of beam on SLM (x,y) in mm

beam_waist_e = 1.0                      # beam radius of input beam (mm)

xrad_e, yrad_e = -1,0                    #  Diffraction grating angles

focal_e = 10e3                          #  Digital lens focal length in mm

################## ------- Measurement Hologram M parameters ------ ##############

x0_m, y0_m = 0, 0                       # Center of beam on SLM (x,y) in mm

beam_waist_m = 1.0                      # beam radius of input beam (mm)

xrad_m, yrad_m = 1,0                    #  Diffraction grating angles

focal_m = 10e3                          # digital lens focal length in mm
```

[4]:
```
############------ Encoding Hologram e parameters ------ ###########

# Create blanck array with SLM parameters

x_e = np.linspace(-x_dim/2+x0_e, x_dim/2+x0_e,pxl_x)
y_e = np.linspace(-y_dim/2+y0_e ,y_dim/2+y0_e ,pxl_y)
X_e, Y_e = np.meshgrid(x_e,y_e)
r_mesh_e, phi_mesh_e = cartesian2polar(X_e,Y_e)


########## --------- Measurement Hologram M parameters ------ ##############


# Create blanck array with SLM parameters

x_m = np.linspace(-x_dim/2+x0_m, x_dim/2+x0_m,pxl_x)
y_m = np.linspace(-y_dim/2+y0_m ,y_dim/2+y0_m ,pxl_y)
X_m, Y_m = np.meshgrid(x_m,y_m)
r_mesh_m, phi_mesh_m = cartesian2polar(X_m,Y_m)
```

2 Generate Measurement State

Encoding state

[5]:
```
l_e = np.array([1,0,0])                 # Define charge values

p_e = np.array([0,0,0])                  # Define radial index

A_e = np.array([1,0,0])                  # Define a_i values

theta_e = np.array([0,0,0])              # Define theta values angles

# Create parameter array
parameter_array_e = create_parameter_array(A_e, theta_e, l_e, p_e)

# Make blanck Qstate e-field profile object using the SLM parameters above
Encoding = Qstate(r_mesh_e,phi_mesh_e, wavelength=wavelength, w0=beam_waist_e)

# Update the e-field according to our state
Encoding.superposition(parameter_array_e)

Psi_r_phi = Encoding.state
```

[6]:
```
plt.imshow(np.abs(Psi_r_phi))
plt.xticks([])
plt.yticks([])
plt.show
```

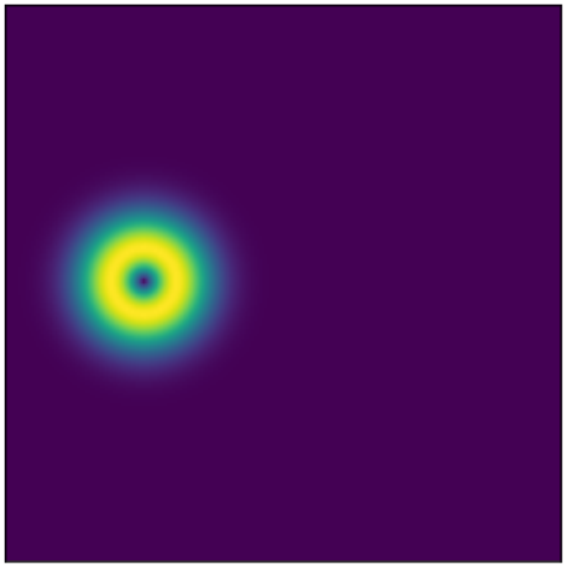

Measurement state

[7]:
```
l_m = np.array([0,0,0])                    # Define charge values

p_m = np.array([0,0,0])                     # Define radial index

A_m = np.array([1,0,0])                     # Define a_i values

theta_m = np.array([0,0,0])                 # Define theta values angles

# Create parameter array
parameter_array_m = create_parameter_array(A_m, theta_m, l_m, p_m)

# Make blanck Qstate e-field profile object using the SLM parameters above
Measurement = Qstate(r_mesh_m,phi_mesh_m, wavelength=wavelength, w0=beam_waist_m)

# Update the e-field according to our state
Measurement.superposition(parameter_array_m)

M_r_phi = Measurement.state
```

[8]:
```
plt.imshow(np.abs(M_r_phi))
plt.xticks([])
plt.yticks([])
plt.show()
```

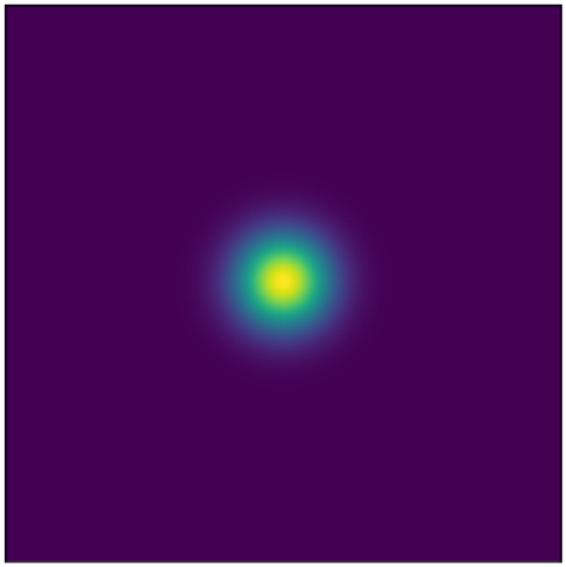

3 Creating Holograms

[9]:
```
################## Encoding Hologram ####################


# Create hologram object of encoded amplitude matrix
hologram_e = QHologram(Encoding)

# Add diffraction grating using angles defined earlier
hologram_e.add_angles(xrad_e, yrad_e)

#Add lense using focal length defined earlier
hologram_e.LensHologram(focal_e)

# modulate the amplitude of the array
hologram_e.josa_array()

# Create final hologram
hologram_matrix_e = hologram_e.create_hologram()

plt.imshow(hologram_matrix_e,cmap='gray')
plt.xticks([])
plt.yticks([])
plt.show()
```

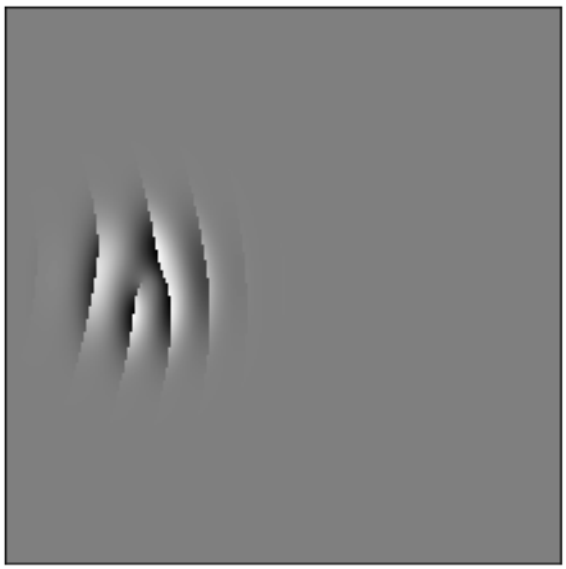

[10]:
```
################## Measurement Hologram ####################

# Create hologram object of encoded amplitude matrix
hologram_m = QHologram(Measurement)

# Add diffraction grating using angles defined earlier
hologram_m.add_angles(xrad_m, yrad_m)

#Add lense using focal length defined earlier
hologram_m.LensHologram(focal_m)

# modulate the amplitude of the array
hologram_m.josa_array()

# Create final hologram
hologram_matrix_m = hologram_m.create_hologram()

plt.imshow(hologram_matrix_m,cmap='gray')
plt.xticks([])
plt.yticks([])
plt.show()
```

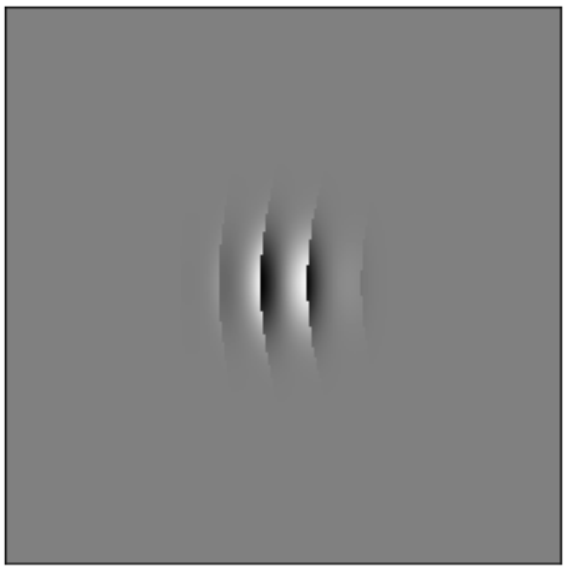

4 Optimization of Encoding SLM Position Along the x and y Axes

[11]:
```
m = 0.1             # Our steps for translation in x and y directions
B = x_dim/4         # Borders for the range of the for loops in x and y directions

step = int(m/pxl_s)

# Defining Gaussian function for curve fitting
def func(x, A, sigma, mu0, C):
    return A * np.exp(-(x-mu0)**2/sigma**2) + C
```

4.1 Translation of Encoding SLM in X Direction

[12]:
```
# Taking the Encoding state to a side to start scanning

x_e = np.linspace(-x_dim/2+B, x_dim/2+B,pxl_x)
y_e = np.linspace(-y_dim/2+y0_e ,y_dim/2+y0_e ,pxl_y)
X_e, Y_e = np.meshgrid(x_e,y_e)
r_mesh_e, phi_mesh_e = cartesian2polar(X_e,Y_e)

# Make blanck Qstate e-field profile object using the SLM parameters above
Encoding = Qstate(r_mesh_e,phi_mesh_e, wavelength=wavelength, w0=beam_waist_e)

# Update the e-field according to our state
Encoding.superposition(parameter_array_e)
```

```
Psi_temp_x = Encoding.state

hologram_e = QHologram(Encoding)

plt.imshow(np.abs(Psi_temp_x))
plt.xticks([])
plt.yticks([])
plt.show()
```

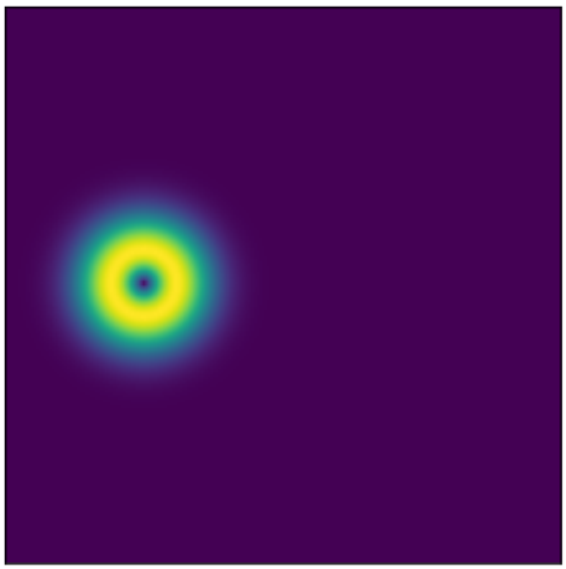

[13]:
```
xe_lin=[]
Pr_xelin =[]

for k, i in enumerate(np.arange(x0_e-B,x0_e+B,m)):

    # roll along x_e

    Psi_temp_x = np.roll(Psi_temp_x,step)

    N = np.abs(np.sum((np.conjugate(Psi_temp_x)*Psi_temp_x)))
    C = np.abs(np.sum((np.conjugate(M_r_phi)*Psi_temp_x)))
    xe_lin.append(i)
    Pr_xelin.append(C/N + np.random.normal(0,0.015))
```

[14]:
```
plt.plot(xe_lin, Pr_xelin, 'b+', label='data',alpha=1)

#Fit for the parameters a, b, c of the function func:
popt, pcov = curve_fit(func, xe_lin, Pr_xelin)
```

```
x_fit = np.linspace(-B,B,100)

#plt.plot(x_fit, func(x_fit, *popt), 'r-', label='fit')
plt.vlines(popt[2],0,1,'k','dashed')

plt.xlabel('x')
plt.ylabel('y')
plt.legend()
plt.show()

print(popt)

plt.imshow(np.abs(Psi_temp_x))
plt.xticks([])
plt.yticks([])
plt.show()
```

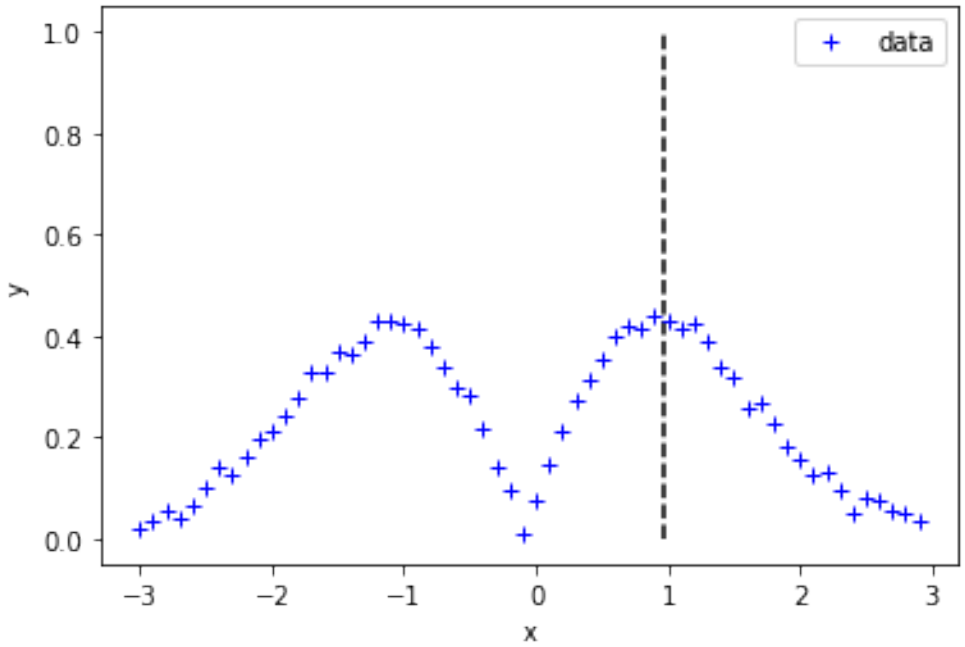


```
[0.26696404 0.54094317 0.96257382 0.19184775]
```

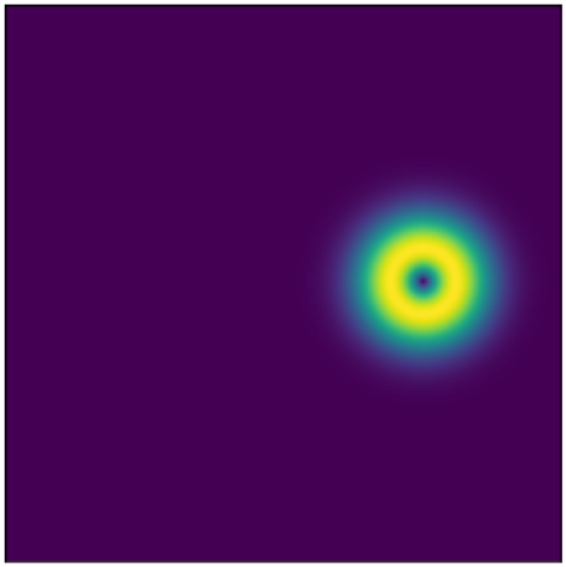

[15]:
```
x0_e = np.round(popt[2],2)

print(f"x0_e = {x0_e}")
```

```
x0_e = -0.1
```

4.2 Translation of Encoding SLM in Y Direction

[16]:
```
# Taking the Encoding state to a side to start scanning

x_e = np.linspace(-x_dim/2+x0_e, x_dim/2+x0_e,pxl_x)
y_e = np.linspace(-y_dim/2+B ,y_dim/2+B ,pxl_y)
X_e, Y_e = np.meshgrid(x_e,y_e)
r_mesh_e, phi_mesh_e = cartesian2polar(X_e,Y_e)

# Make blanck Qstate e-field profile object using the SLM parameters above
Encoding = Qstate(r_mesh_e,phi_mesh_e, wavelength=wavelength, w0=beam_waist_e)

# Update the e-field according to our state
Encoding.superposition(parameter_array_e)

Psi_temp_y = Encoding.state

hologram_e = QHologram(Encoding)

plt.imshow(np.abs(Psi_temp_y))
plt.show()
```

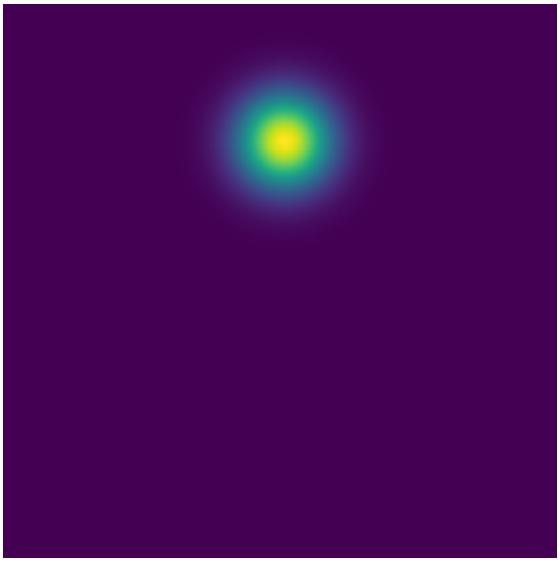

[17]:
```
ye_lin=[]
Pr_yelin=[]

for k, i in enumerate(np.arange(y0_e-B,y0_e+B,m)):

    # roll along y_e

    Psi_temp_y = np.roll(Psi_temp_y,step,axis=0)

    N = np.abs(np.sum((np.conjugate(Psi_temp_y)*Psi_temp_y)))
    C = np.abs(np.sum((np.conjugate(M_r_phi)*Psi_temp_y)))
    ye_lin.append(i)
    Pr_yelin.append(C/N + np.random.normal(0,0.015))
```

[18]:
```
plt.plot(ye_lin, Pr_yelin, 'b+', label='data',alpha=1)

#Fit for the parameters a, b, c of the function func:
popt, pcov = curve_fit(func, ye_lin, Pr_yelin)

x_fit = np.linspace(-B,B,100)

plt.plot(x_fit, func(x_fit, *popt), 'r-', label='fit')
plt.vlines(popt[2],0,1,'k','dashed')

plt.xlabel('x')
plt.ylabel('y')
plt.legend()
plt.show()
```

```
print(popt)

plt.imshow(np.abs(Psi_temp_y))
plt.xticks([])
plt.yticks([])
plt.show()
```

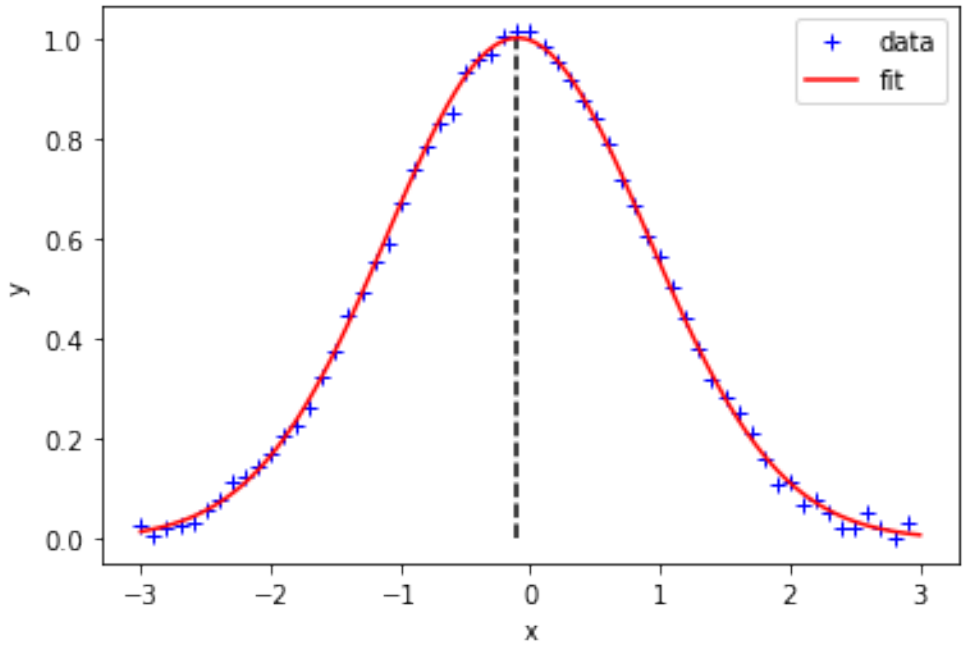


```
[ 1.00414083  1.41993777 -0.09863342 -0.00271039]
```

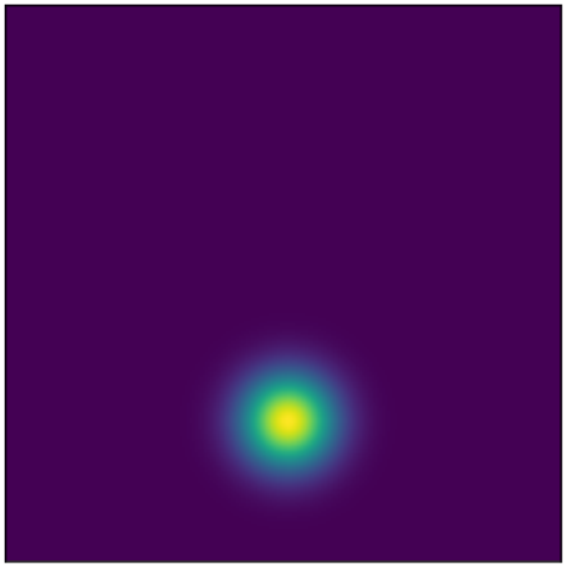

[19]:
```
y0_e = np.round(popt[2],2)

print(f"y0_e = {y0_e}")
```

```
y0_e = -0.1
```

4.3 Updating the Center Coordinates of the Encoding SLM

[20]:
```
### Here we replace the x0_e and y0_e with the updated ones ###

x_e = np.linspace(-x_dim/2+x0_e, x_dim/2+x0_e,pxl_x)
y_e = np.linspace(-y_dim/2+y0_e ,y_dim/2+y0_e ,pxl_y)
X_e, Y_e = np.meshgrid(x_e,y_e)
r_mesh_e, phi_mesh_e = cartesian2polar(X_e,Y_e)

# Make blanck Qstate e-field profile object using the SLM parameters above
Encoding = Qstate(r_mesh_e,phi_mesh_e, wavelength=wavelength, w0=beam_waist_e)

# Update the e-field according to our state
Encoding.superposition(parameter_array_e)

Psi_r_phi = Encoding.state

hologram_e = QHologram(Encoding)
```

5 Optimization of Measurement SLM Position Along the x and y Axes

5.1 Translation of measurement SLM in X direction

[21]:
```
# Taking the Measurement state to a side to start scanning

x_m = np.linspace(-x_dim/2+B, x_dim/2+B,pxl_x)
y_m = np.linspace(-y_dim/2+y0_m ,y_dim/2+y0_m ,pxl_y)
X_m, Y_m = np.meshgrid(x_m,y_m)
r_mesh_m, phi_mesh_m = cartesian2polar(X_m,Y_m)

# Make blanck Qstate e-field profile object using the SLM parameters above
Measurement = Qstate(r_mesh_m,phi_mesh_m, wavelength=wavelength, w0=beam_waist_m)

# Update the e-field according to our state
Measurement.superposition(parameter_array_m)

M_temp_x = Measurement.state

hologram_m = QHologram(Measurement)


plt.imshow(np.abs(M_temp_x))
plt.xticks([])
plt.yticks([])
plt.show()
```

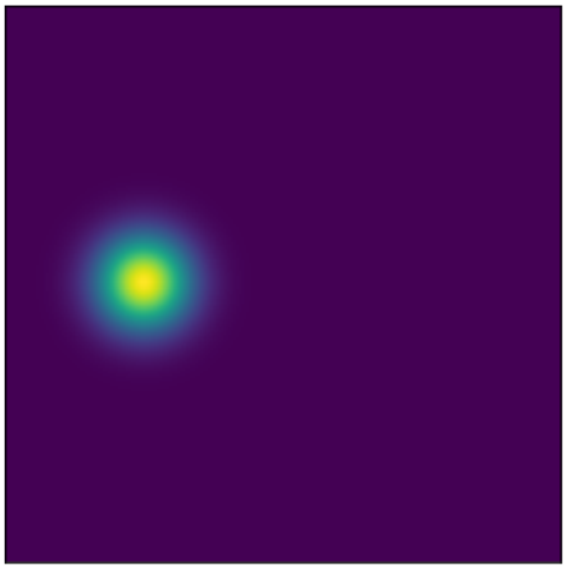

[22]:
```
xm_lin=[]
Pr_xmlin =[]

for k, i in enumerate(np.arange(x0_m-B,x0_m+B,m)):

    # roll along x_m

    M_temp_x = np.roll(M_temp_x,step)

    N = np.abs(np.sum((np.conjugate(Psi_r_phi)*Psi_r_phi)))
    C = np.abs(np.sum((np.conjugate(M_temp_x)*Psi_r_phi)))
    xm_lin.append(i)
    Pr_xmlin.append(C/N + np.random.normal(0,0.015))
```

[23]:
```
plt.plot(xm_lin, Pr_xmlin, 'b+', label='data',alpha=1)

#Fit for the parameters a, b, c of the function func:
popt, pcov = curve_fit(func, xm_lin, Pr_xmlin)

x_fit = np.linspace(-B,B,100)

plt.plot(x_fit, func(x_fit, *popt), 'r-', label='fit')
plt.vlines(popt[2],0,1,'k','dashed')

plt.xlabel('x')
plt.ylabel('y')
plt.legend()
plt.show()

print(popt)

plt.imshow(np.abs(M_temp_x))
plt.xticks([])
plt.yticks([])
plt.show()
```

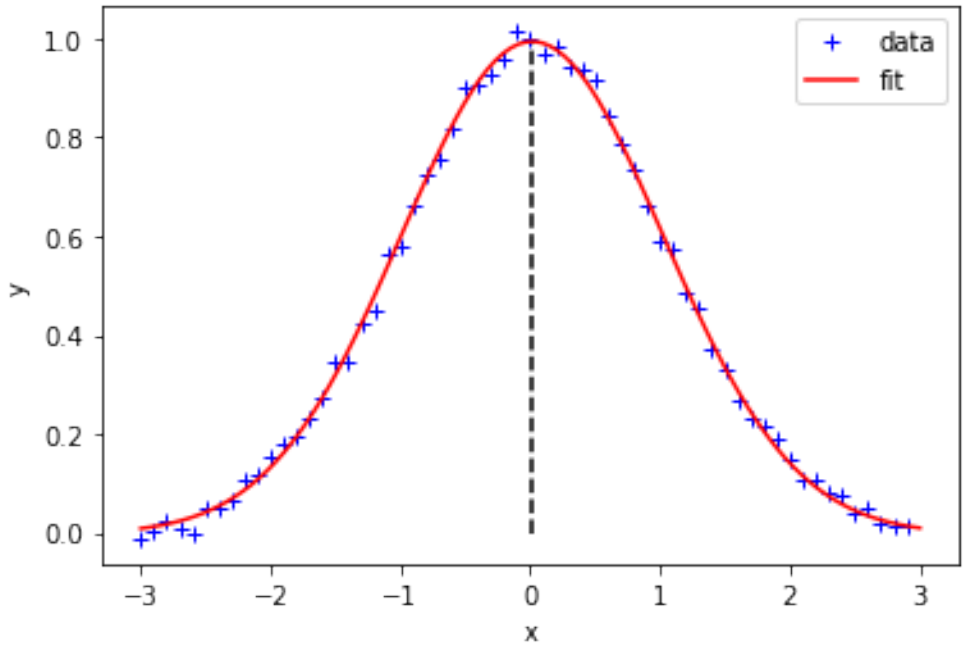


```
[ 0.99628022  1.42612233  0.01449681 -0.00266292]
```

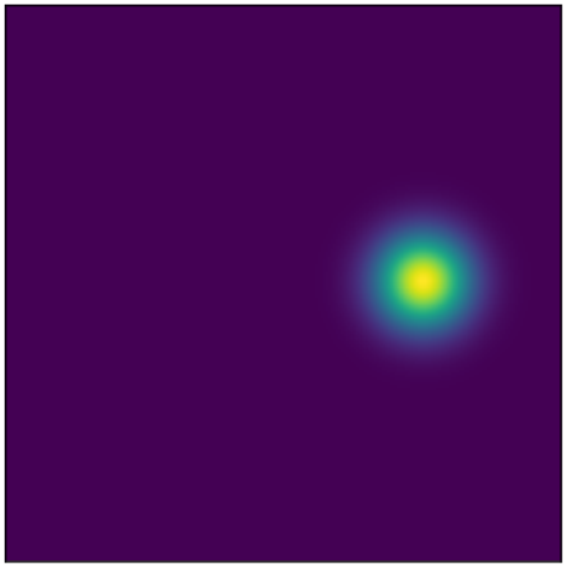

[24]:
```
x0_m = np.round(popt[2],2)
```

```
print(f"x0_m = {x0_m}")
```

```
x0_m = 0.01
```

5.2 Translation of Measurement SLM in Y Direction

[25]:
```
# Taking the Measurement state to a side to start scanning

x_m = np.linspace(-x_dim/2+x0_m, x_dim/2+x0_m,pxl_x)
y_m = np.linspace(-y_dim/2+B ,y_dim/2+B ,pxl_y)
X_m, Y_m = np.meshgrid(x_m,y_m)
r_mesh_m, phi_mesh_m = cartesian2polar(X_m,Y_m)

# Make blanck Qstate e-field profile object using the SLM parameters above
Measurement = Qstate(r_mesh_m,phi_mesh_m, wavelength=wavelength, w0=beam_waist_m)

# Update the e-field according to our state
Measurement.superposition(parameter_array_m)

M_temp_y = Measurement.state

hologram_m = QHologram(Measurement)

plt.imshow(np.abs(M_temp_y))
plt.xticks([])
plt.yticks([])
plt.show()
```

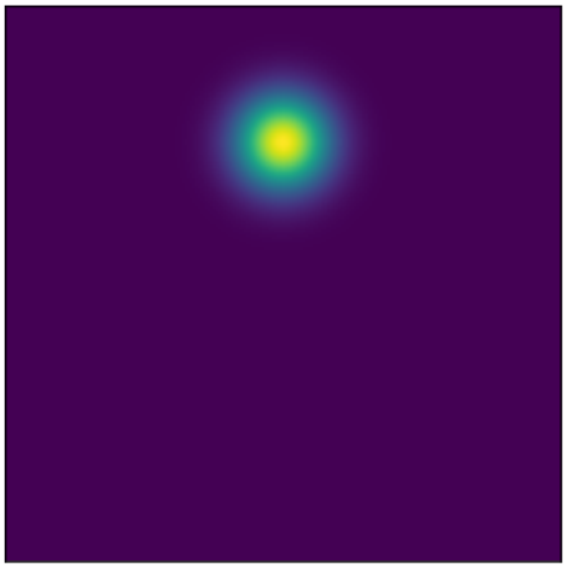

[26]:
```
ym_lin=[]
Pr_ymlin=[]

for k, i in enumerate(np.arange(y0_m-B,y0_m+B,m)):

    # roll along y_m

    M_temp_y = np.roll(M_temp_y,step,axis=0)

    N = np.abs(np.sum((np.conjugate(Psi_r_phi)*Psi_r_phi)))
    C = np.abs(np.sum((np.conjugate(M_temp_y)*Psi_r_phi)))
    ym_lin.append(i)
    Pr_ymlin.append(C/N + np.random.normal(0,0.015))
```

[27]:
```
plt.plot(ym_lin, Pr_ymlin, 'b+', label='data',alpha=1)

#Fit for the parameters a, b, c of the function func:
popt, pcov = curve_fit(func, ym_lin, Pr_ymlin)

x_fit = np.linspace(-B,B,100)

plt.plot(x_fit, func(x_fit, *popt), 'r-', label='fit')
plt.vlines(popt[2],0,1,'k','dashed')

plt.xlabel('x')
plt.ylabel('y')
plt.legend()
plt.show()

print(popt)

plt.imshow(np.abs(M_temp_y))
plt.xticks([])
plt.yticks([])
plt.show()
```

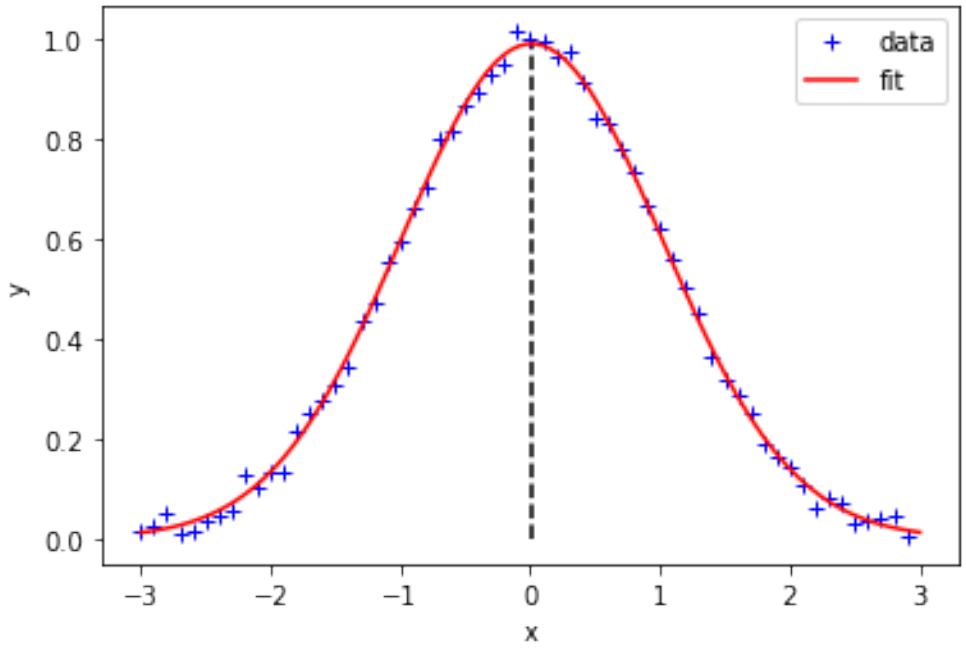


```
[9.88271864e-01 1.41800065e+00 1.07125568e-02 1.22927452e-03]
```

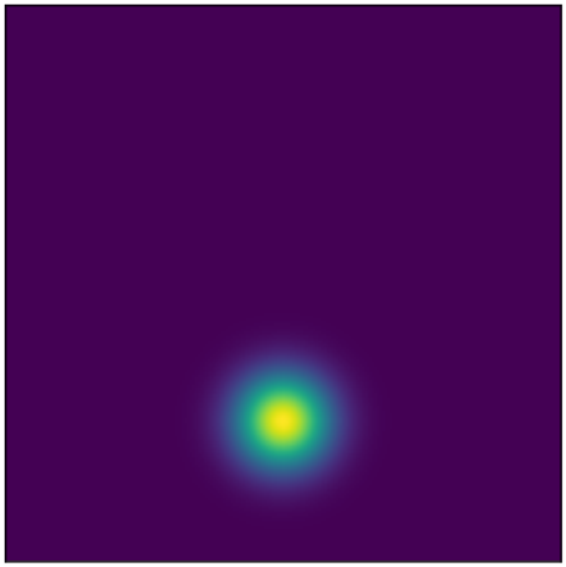

[28]:
```
y0_m = np.round(popt[2],2)
```

```
print(f"y0_m = {y0_m}")
```

```
y0_m = 0.01
```

5.3 Updating the Center Coordinates of the Measurement SLM

[29]:
```
### Here we replace the x0_m and y0_m with the updated ones ###

x_m = np.linspace(-x_dim/2+x0_m, x_dim/2+x0_m,pxl_x)
y_m = np.linspace(-y_dim/2+y0_m ,y_dim/2+y0_m ,pxl_y)
X_m, Y_m = np.meshgrid(x_m,y_m)
r_mesh_m, phi_mesh_m = cartesian2polar(X_m,Y_m)

# Make blanck Qstate e-field profile object using the SLM parameters above
Measurement = Qstate(r_mesh_m,phi_mesh_m, wavelength=wavelength, w0=beam_waist_m)

# Update the e-field according to our state
Measurement.superposition(parameter_array_m)

M_r_phi = Measurement.state

hologram_m = QHologram(Measurement)
```

6 Print the Optimized Coordinates

[30]:
```
print("The optimized parameters are:",
      "Coordinates:",
      "x0_e: {}".format(x0_e),
      "y0_e: {}".format(y0_e),
      "x0_m: {}".format(x0_m),
      "y0_e: {}".format(y0_m),
       sep='\n')
```

```
The optimized parameters are:
Coordinates:
x0_e: -0.11
y0_e: -0.11
x0_m: 0.01
y0_e: 0.01
```

بنی آدم اعضای یکدیگرند
که در آفرینش ز یک گوهرند

چو عضوی به درد آورد روزگار
دگر عضوها را نماند قرار

تو کز محنت دیگران بی‌غمی
نشاید که نامت نهند آدمی

سعدی شیرازی
گلستان

Human beings are members of a whole
In creation of one essence and soul
If one member is afflicted with pain
Other members uneasy will remain
If you have no sympathy for human pain
The name of human you cannot retain

Saadi Shirazi
Golestan